

Spin Exciton Dynamics in Singlet Fission: The *JDE* Model

by

Kori Elizabeth Smyser

B.S., Chemistry, Montana State University, 2017

A thesis submitted to the
Faculty of the Graduate School of the
University of Colorado in partial fulfillment
of the requirement for the degree of
Doctor of Philosophy, Chemical Physics
Department of Chemistry

2022

Committee Members:

Joel Eaves

Niels Damrauer

Sandeep Sharma

Obadiah Reid

Victor Gurarie

Smyser, Kori Elizabeth (Ph.D., Chemical Physics)

Spin Exciton Dynamics in Singlet Fission: The *JDE* Model

Thesis directed by Professor Joel D. Eaves

Abstract

Singlet fission is a photophysical process that takes place in some organic chromophores, where one optically bright singlet exciton rapidly generates two spin-entangled triplet excitons. For over a decade, photovoltaic applications motivated most of the research in singlet fission. This work builds rational molecular design principles for quantum information applications using it.

Based on basic molecular symmetries, I derive the *JDE* model hamiltonian, and analyze the time evolution of the magnetic sublevels formed during singlet fission by developing a nonadiabatic transition theory. These dynamics manifest in time-resolved electron paramagnetic resonance spectra (trEPR) whose basic measurement forms the basis of a quantum gate. I propose that if the relaxation process between exciton spin sublevels is state specific, singlet fission can overcome one of the most formidable challenges in quantum computing—the tyranny of temperature. Using this theory, I predict the conditions for state-selective population of EPR active states: strong inter-chromophore exchange coupling, mutual alignment between molecular axes on the chromophore pairs, and a high degree of ordering, both static and dynamic.

To make connections to experiments, I extend the *JDE* model to a glassy, orientationally disordered sample of nonparallel but rigidly bound molecular dimers, TIPS-BP1', and assign the trEPR spectrum with unprecedented accuracy. This work shows that, indeed, singlet fission can initialize specific magnetic sublevels, even when the molecular axes are not all mutually parallel. Additionally, spin sublevel coherences in this molecule

are long-lived at temperatures much higher than in conventional quantum hardware.

For crystalline samples, chromophores are densely packed and statically ordered, but excitons may hop to neighboring sites and become increasingly distant, challenging the dynamic ordering requirement. In my final chapter, I construct a model for an oriented crystal of all-parallel TES TIP-TT chromophores and calculate the spectrum from populations of paired, entangled triplets and unpaired triplets that have undergone one or more hops. A simple model of unpairing allows the assignment of unpaired triplets that emerge from a spin-coherent quintet state, for the first time, in trEPR spectra of this molecule.

Acknowledgements

I am incredibly grateful to my family and cherish the laughter and support they have shared with me. They taught me how to find joy in the little things with cards in hand, how to celebrate my quirks, the importance of a rich vocabulary and sense of humor, and showed me the meaning of unconditional love, patience, and strength. Jessica Taylor, “you are my cousin and I love you.”

I am very grateful to those at Montana State University and the University of Colorado who guided, supported, and believed in me. I would especially like to thank Erik Grumstrup for introducing me to the creative and exciting world of academic research. I will fondly remember the late-night lab report writing sessions with Anna Scott, Axl Levan, Tacey Hicks, Tom Robinson, Jessie Bohn, and Scott Spring that soon became family dinners.

I am likewise thankful for the efforts and support of my fellow first-years at CU. It was nice to have friends that not only managed to make homework fun but took the time with me to learn and understand fully. I thank my committee for their interest in me and my research and their valuable feedback over the years—especially my academic grandpa Niels Damrauer, who made time when I needed advice. I truly cannot imagine a better graduate research experience than my time with the Eaves lab. From class to the lab, it has been a sincere pleasure learning from my adviser, Joel Eaves, and I have greatly

appreciated his patience when repeating derivations and discussions. I am thankful to be staying in the area because I look forward to any future group get-togethers with his home-smoked salmon on the menu; it is delicious, and I am more than happy to help with the leftovers. I, too, would like to thank my fellow Eaves group members for supporting me, for listening and sharing, and for remembering to invite me to the get-togethers.

I want to thank all the friends that have brightened my life. I am so fortunate to have been surrounded by a colorful, adventurous, and passionate group of people in a place that matches their spirit. We have lived. Alex Kennedy, you are a beautiful, brave, caring soul, and I love you. I thank my Lucky Joe's and Dave's Sushi families for helping me get here and supporting me along the way. Finally, I am thankful for the love and support of my partner, Keith Portman. I appreciate your positive attitude, love of volcanoes, and your understanding and care throughout this past year. I look forward to our next chapter together.

Contents

1	Introduction	1
1.1	Optically Pumped Spin Polarization	1
1.2	Singlet Fission	3
1.3	The Time-Resolved Electron Paramagnetic Resonance Experiment	7
2	Singlet Fission for Quantum Information and Quantum Computing: The Parallel <i>JDE</i> Model	13
2.1	Abstract	13
2.2	Introduction	14
2.3	The Spin-Exciton Hamiltonian	14
2.4	Spin Dynamics and Selection Rules at Zero Applied Field	18
2.5	EPR Spectroscopy	24
2.6	Discussion	29
3	The <i>JDE</i> Model Formalism	32
3.1	Model Development	32
3.2	The <i>JDE</i> Spin-Exciton Hamiltonian in Cartesian Space	34
3.2.1	Deriving <i>JDE</i> Model Hamiltonian	34
3.2.2	Introduction to Tensor Formalism	37

3.2.3	Isotropic Inter-chromophore Exchange Interaction	41
3.2.4	Anisotropic Intra-chromophore Interactions	43
3.2.5	Anisotropic Inter-chromophore Interaction	49
3.2.6	Rank-1 Interactions	51
3.2.7	Coupled Spin States	52
3.2.8	Selection Rules from Discrete Symmetries	56
3.3	The Wigner-Eckart Theorem	63
3.3.1	Spherical Tensor Formalism	64
3.3.2	The Rotated <i>JDE</i> Model	69
3.3.3	Matrix Elements from the Wigner-Eckart Theorem	75
3.3.4	Reduced Matrix Elements from the Wigner-Eckart Theorem	76
3.3.5	Selection Rules from the Wigner-Eckart Theorem	79
3.3.6	Isotropic Inter-chromophore Exchange Matrix Elements	82
3.3.7	Anisotropic Intra-chromophore Matrix Elements	85
3.3.8	Anisotropic Inter-chromophore Matrix Elements	88
3.3.9	Rank-1 Intra-chromophore Matrix Elements	89
3.3.10	Rank-1 Inter-chromophore Matrix Elements	91
3.4	Nonadiabatic Transition Theory for the <i>JDE</i> Model	91
3.4.1	Choice of Basis for the <i>JDE</i> model	93
3.4.2	Calculating the Quintet State Populations	94
3.4.3	Calculating the EPR Spectrum	95
3.4.4	Best-fit Parameters by Simulated Annealing	99
4	Entangled, Spin-polarized Excitons from Singlet Fission in a Rigid Dimer	101
4.1	Abstract	101

4.2 Entangled, Spin-polarized Excitons from Singlet Fission in a Rigid Dimer	102
5 Triplet-Pair Spin Signatures from Macroscopically Aligned Heteroacenes in an Oriented Single Crystal	116
5.1 Abstract	116
5.2 Introduction	117
5.3 Theory and Calculations for the EPR Spectra	118
5.4 Magnetophotoluminescence Spectroscopy	120
5.5 Electron Paramagnetic Resonance Spectroscopy.	124
Bibliography	133
A Quantifying Entanglement	142
B The Q_0 Model	145

List of Figures

1.1	Optically induced spin polarization generates states for quantum information applications near room temperature.	2
1.2	Singlet fission.	4
1.3	Spin dynamics for the triplet pair.	5
1.4	Exciton fission.	6
1.5	Magnetic spin-spin interactions have distributions.	8
1.6	The trEPR experiment.	9
1.7	The triplet trEPR spectrum as a function of orientation.	11
2.1	The <i>JDE</i> model.	16
2.2	Zero-field energy and selection rules.	20
2.3	Calculated prompt EPR spectra for the rotation of an oriented and parallel sample with respect to an applied field.	26
2.4	The $\theta = 90^\circ$ field-swept prompt EPR quintet spectrum for a parallel dimer of pentacene molecules in a dilute	28
3.1	Model development scheme.	32
3.2	Orientation-dependent parameters for the <i>JDE</i> model.	44
3.3	The coordinate frames of the <i>JDE</i> model.	50

3.4	Active and passive rotations.	71
3.5	Partitioning the hamiltonian and the choice of basis.	94
4.1	TrEPR data for TIPS-BP1' demonstrates long spin-coherence times and strong spin polarization.	105
4.2	The intersystem crossing triplet EPR spectrum of TIPS-Pc monomers in a heavy atom solvent.	106
4.3	Data and calculated EPR spectrum for TIPS-BP1'.	109
4.4	The quintet spectrum from the diabatic basis.	112
4.5	Theory predicts strong spin polarization for the rigid TIPS-BP1' dimer.	114
5.1	Structure of TES TIPS-TT and the molecular coordinate system.	118
5.2	Magnetophotoluminescence spectrum for TES TIPS-TT.	121
5.3	Schematic and associated energy level diagrams for the inter- and intra-triplet interactions J and D .	122
5.4	TrEPR spectra of a single crystal of TES TIPS-TT.	125
5.5	Early time (25 -75 ns) spectra and calculations of single crystal sample.	127
5.6	Calculated spectra, populations and energy level plots for single crystal trEPR data at specified orientations between 10° and 60°.	128
5.7	Calculated spectra, populations and energy level plots for single crystal trEPR data at specified orientations between 70° and 120°.	129
5.8	Calculated spectra, populations and energy level plots for single crystal trEPR data at specified orientations between 130° and 180°.	130
B.1	Reproduction of the strong-field PL spectrum from Johnson and Merrifield and calculated pair state energies.	146

List of Tables

3.1 Exchange symmetry selection rules	60
3.2 Inversion symmetry selection rules	63
3.3 Rotational symmetry selection rules	81

Copyright

All images, figures and illustrations are the work of the author unless otherwise noted.

Text and figures are © 2022 Kori Elizabeth Smyser unless otherwise noted.

Chapter 1

Introduction*

1.1 Optically Pumped Spin Polarization

Materials capable of storing and manipulating quantum data must maintain quantum coherences and entanglement over timescales that are orders of magnitude longer than the system's quantum beat period.¹ But quantum states are fragile, and most materials do not sustain quantum coherences when temperatures are in excess of a few Kelvin. This "tyranny of low temperature" is a major hurdle to realizing accessible quantum computing and information technologies.

From a quantum information perspective, the photoproducts of singlet fission can solve two outstanding problems associated with the tyranny of low temperature, and they do it in complementary ways. Each corresponds to one of the criteria for quantum computing set forth by Ref. [1]. To paraphrase: a system capable of quantum information processing must be prepared in a *pure quantum state*, not a mixed one.² Once initialized, one must be able to execute a deterministic sequence of unitary operations, or quantum gates, on that state so that it can be coaxed into collapsing on the final state, which is the solution to a computational problem, with high probability and in polynomial time.^{3,4}

*Adapted with permission from Smyser, K. E. & Eaves, J. D. *Sci. Rep.* **10**, 18480, (2020).

Because magnetic resonance experiments operate in the “strong-field” regime where the Rabi frequency, Ω , is comparable to the transition frequency, ω (Fig. 1.1a), they can drive arbitrary unitary operations between quantum spin states.⁵ But the gap between

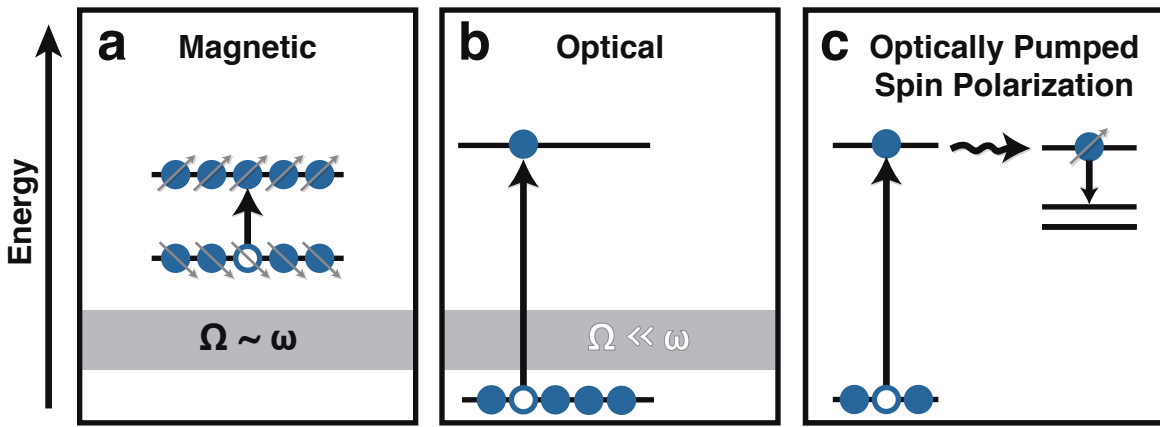


FIGURE 1.1: (a) In magnetic resonance experiments, the Rabi frequency, Ω , can be comparable to the transition (Larmor) frequency, ω . In this strong field limit, it is possible to completely manipulate a quantum state (qubit). However, the energy gap between states is small relative to $k_B T$. This is a source of uncertainty when the state is initialized. (b) In optical transitions, the energy gap is large relative to $k_B T$. But the Rabi frequency is much less than the transition frequency, which means that gate operations done with weak optical fields will be incomplete and noisy. (c) By coupling optical excitations to an internal conversion process, such as singlet fission (wavy arrow), one may capitalize on the advantages of both methods, provided that the relaxation is state-selective.

the ground and excited states in these experiments is small relative to $k_B T$, and as a result, there is a great deal of thermally generated uncertainty in the initial state of the system. In the language of the density matrix, the initial state is mixed, not pure. Optical experiments, by contrast, have a large gap between ground and excited states relative to $k_B T$ (Fig. 1.1b), so that thermal fluctuations do not generate appreciable uncertainty in the ensemble of initial states. The Rabi frequency in optical experiments, however, is perturbatively small relative to the transition frequency. It is therefore very difficult

or impossible to induce a population inversion in an optical experiment, which severely limits the ability of a purely optical experiment to perform quantum gate operations.

In more recent years, researchers have become interested in systems where it is possible to generate spin polarization through optical pumping (Fig. 1.1c).^{6,7} The optical field removes the uncertainty in the initial state of the system, and magnetic resonance experiments on the optically prepared photoproduct, well in the strong-field regime, perform the quantum gate operations. The nitrogen-vacancy (NV) center in diamond is an example of a system that operates on these principles. In solid-state systems, like the NV center, spin centers are implanted into the material post-synthesis. Because the defects are often randomly dispersed, these materials have problems with scalability that might be overcome in molecular systems that are synthesized from the bottom up. In this dissertation, I explore the phenomenon of singlet fission as a novel platform on which one might build quantum data structures and gates near room temperature.

1.2 Singlet Fission

Singlet fission is a photophysical interconversion process that takes place between specifically designed organic chromophores. Following excitation with a photon (γ), an optically bright singlet state on one chromophore is shared with another chromophore in its ground state, S_0S_1 , and rapidly relaxes into a doubly excited, spin-singlet state, ^1TT (Fig. 1.2),^{8–10}



In this notation, the superscript indicates the state's multiplicity in terms of the total spin S , and the TT designates the spatial nature of the spin wavefunction. Here, the subscripts 0 and 1 designate the ground and excited electronic states, respectively. The $|^1\text{TT}\rangle$ spin wavefunction is a maximally entangled, coherent superposition over three of the nine spin sublevels of the two-triplet basis states (Section 3.2.7, Eq. 3.47).^{11–13} In the

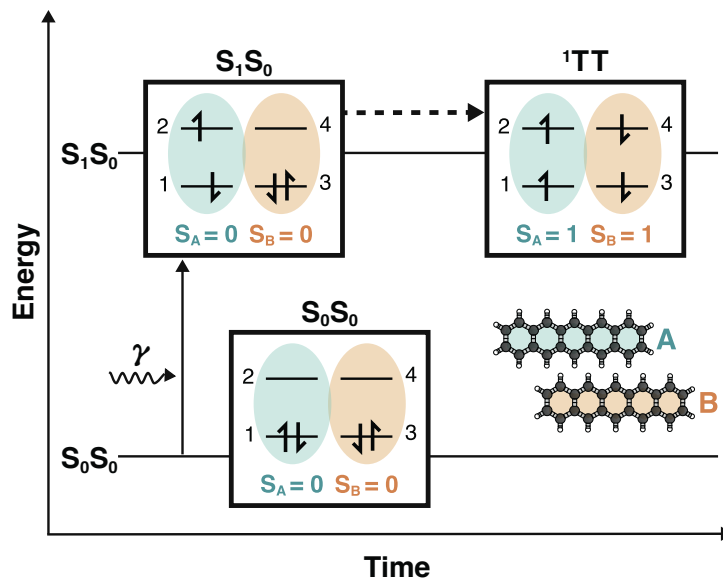


FIGURE 1.2: Singlet fission is a photophysical process that takes place in some pairs of organic chromophores, or dimers, the targets of the proposed research. A single chromophore is photoexcited (γ) into an excited singlet state S_1 , from its ground state S_0 . This single excitation delocalizes in the dimer generating the singly excited spin state S_0S_1 . Singlet fission (dashed arrow) is the non-radiative, spin-conserving and energy-conserving transition that forms a singlet two-triplet state ^1TT . This process involves both chromophores, A and B, which are occupied by electrons 1, 2 and 3, 4 that reside in the highest occupied molecular orbital (HOMO) and lowest unoccupied molecular orbital (LUMO) on each chromophore. The spin of the electrons is emphasized here where, for example, S_A gives the spin eigenvalue of the two-electron state in chromophore A.

last few years, time-resolved electron paramagnetic resonance (trEPR) experiments have combined pulsed optical laser excitation with magnetic resonance to reveal that the ^1TT

state evolves into various $^{2S+1}\text{TT}_M$ spin sublevels,¹⁴⁻²²

$$^1\text{TT} \rightleftharpoons ^{2S+1}\text{TT}_M, \quad (1.3)$$

where the subscript, M , now refers to the magnetic sublevel $-S \leq M \leq +S$. Although singlet fission is a spin-conserving process (Eq. 1.2), the triplet pair sublevels (Eq. 1.3) are not eigenfunctions of the electronic spin hamiltonian; they are non-stationary and evolve in time. In crystalline systems, these excitons may hop to neighboring sites, becoming

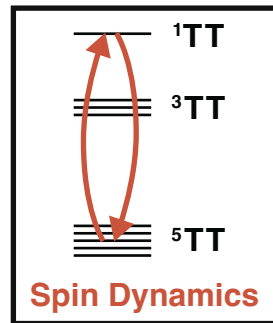


FIGURE 1.3: Spin dynamics for the triplet pair. There are nine coupled pair states that are characterized by a total spin S , each with multiplicity $2S + 1$ —one singlet ^1TT , three triplets ^3TT , and five quintets ^5TT . Spin dynamics of the triplet pair states, including dephasing and population relaxation, occur over the timescale of nanoseconds (ns) to milliseconds (ms). The major goal of this work is to derive selection rules and develop a rate theory for population relaxation between the various spin states.

increasingly more distant, and eventually unpair into $\text{T} + \text{T}$ (Fig. 1.4):²³

$$^{2S+1}\text{TT}_M \rightleftharpoons \text{T} + \text{T}. \quad (1.4)$$

There has not been a consistent microscopic theory that can explain the set of relaxation phenomena embodied in Eqs. 1.1-1.4. In 1967, the discovery of magnetic field

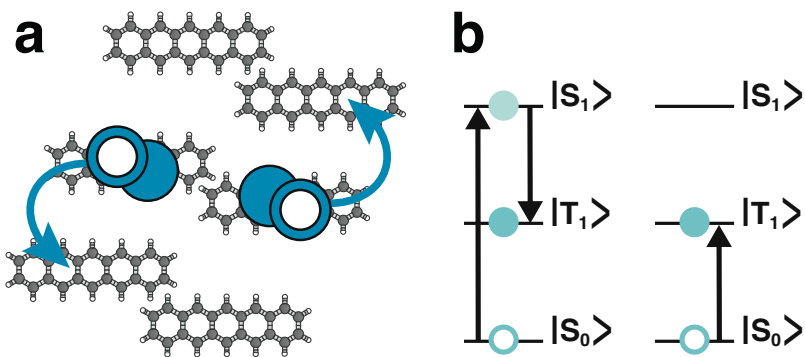


FIGURE 1.4: (a) At long times in crystals, hopping events unpair the biexciton from singlet fission. Hopping induced fluctuations in the inter-exciton coupling leads to irreversible coherence decay (Eq. 1.4, right arrow). The separated triplets can then recombine so that the accompanying rapid increase in the coupling collapses the T + T states onto the pair spin states (Eq. 1.4, left arrow). (b) Singlet fission is an unconventional spin conserving pathway. An optical pulse excites a single chromophore into the singlet excited state S_1 from its ground state S_0 . If the triplet exciton state T_1 is nearly half the energy of the S_0S_1 state, singlet fission can generate a doubly excited dimer state TT, the triplet pair, with overall singlet multiplicity. The traditional picture of singlet fission here shows how two triplet excitons are formed and places less emphasis on the spin and coupled nature of the exciton states than the description in Fig. 1.2. The electron and hole are represented by filled and open circles, respectively.

effects on the delayed fluorescence intensity from anthracene crystals²⁴ proved the theory of singlet fission that arose through various contributions throughout the preceding decade.^{25–28} These early studies focused on the phenomena in the limit of pair state degeneracy and at long times. Motivated to better understand energy transfer processes, they led to a fundamental understanding of mobile excitons in crystals. The spin dynamics described by Eq. 1.3, however, remained a missing piece of the singlet fission puzzle.

For the most part, the literature from this field grew quiet until Nozik and Michl resurrected singlet fission for photovoltaic applications in the early 2000s.⁸ Methods were no longer qualitative but aimed toward quantitatively increasing the efficiency of singlet fission and unpaired triplet excitons to maximize the production of independent charge

carriers from a single photon event for solar cell devices. In the decades that followed, ultrafast lasers replaced the magnetic field. But, again, interest fell on the exciton dynamics rather than the spin dynamics of the pair state.

While the lion's share of attention over the past decade has focused on maximizing the conversion of the ^1TT state to $\text{T} + \text{T}$ for energy applications,^{29,30} we argue that for quantum information applications, one should seek to instead *limit* the decay into independent excitons, by designing molecules that make the conversion from ^1TT to $^{2S+1}\text{TT}_M$ as state-selective as possible. Chapters 2 and 3 develop a theory for the spin dynamics for relaxation between the strongly coupled triplet pair states. The theory replicates the trEPR spectrum from molecular dimers in Chapter 4 and dimers in crystals in Chapter 5.

1.3 The Time-Resolved Electron Paramagnetic Resonance Experiment

TrEPR is a time-resolved magnetic resonance experiment that measures the energies and relative populations of magnetic spin sublevels. The experiment is analogous to nuclear magnetic resonance (NMR) experiments, but it probes the transitions between electron spin sublevels, rather than nuclear. Electrons are characterized by their spin quantum number S . A spin- S state has a multiplicity of $2S + 1$ which describes the number of magnetic sublevels, labelled by the quantum number $-S \leq M \leq S$, that comprise the spin state. The spin of an electron describes the magnitude of its magnetic moment, $\vec{\mu} = -g\mu_B\mathbf{S}$, where μ_B is the Bohr magneton and g is the g-factor of the spin particle.

Local magnetic interactions direct the precession of the spin magnetic moment in the

absence of an applied field. One may imagine that local spin interactions have orbital-like distributions in space (Fig. 1.5). These interactions have a representation where their values are maximized along a set of axes, called the principal axis system. Although different interactions have different principal axes, it is often the case that they correspond to molecular symmetries. Because the local dipole, or magnetic, spin interactions (Figs. 1.5) are diagonal in their principal axis system, the spin states that diagonalize the hamiltonian at zero-field are conventionally labelled by these axes (x, y, z). These interactions are called “zero-field splitting” (ZFS) interactions because they split the energies of magnetic states in the absence of an applied field (Fig. 1.6b).

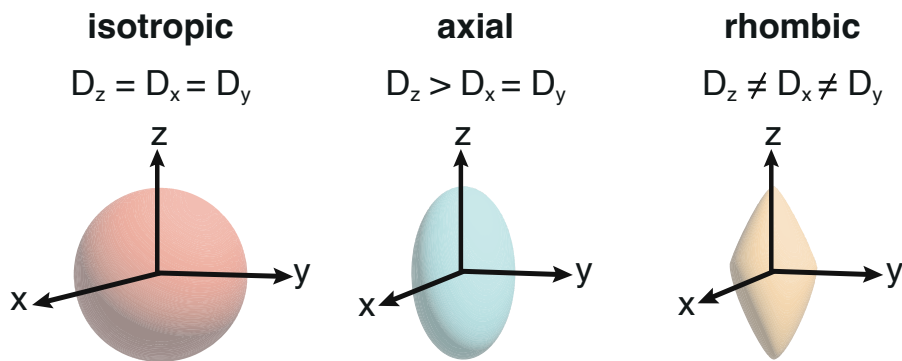


FIGURE 1.5: Magnetic spin-spin interactions are three dimensional and have distributions in space. The interactions have maxima along the axes of their principal frames (x, y, z). Depending on the relative magnitudes of the principal values, D_z , D_x , and D_y , the distributions are spatially characterized as being either isotropic, axial or rhombic.

In an EPR experiment, a static magnetic field, or Zeeman field, $\vec{B}_0 = (0, 0, B_0)$ is applied to the spin system and its direction defines the lab z -axis (Fig. 1.6a, red arrow). A strong Zeeman field ($B_0 \gg |D|$) applies a torque to the spin magnetic moment and redirects the spin to precess about the lab z -axis (Fig. 1.6a, blue arrow). The energy of the Zeeman spin sublevels $|S, M\rangle$ in the field are tuned by the field by an energy proportional to M .

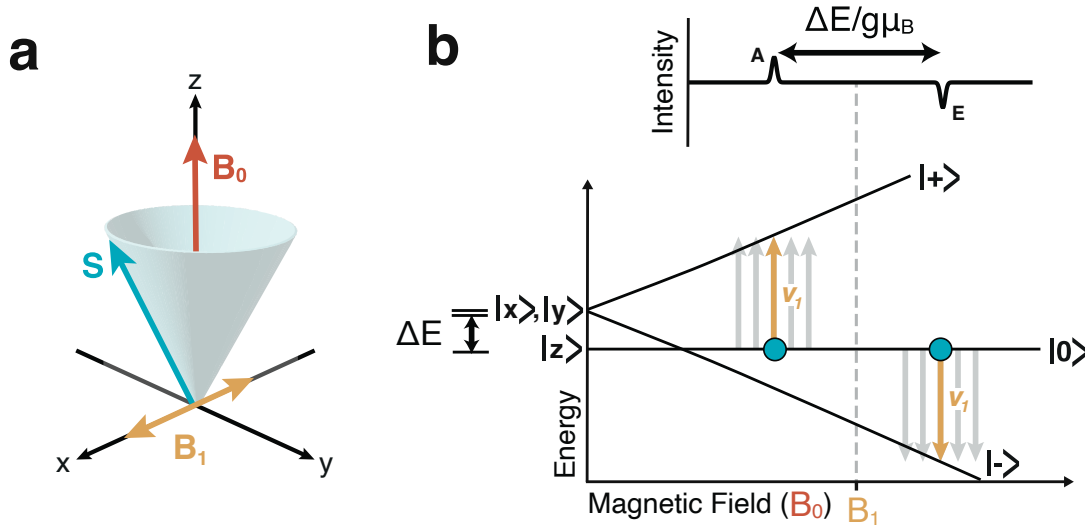


FIGURE 1.6: The trEPR experiment. **(a)** The direction of the static Zeeman field \vec{B}_0 defines lab z -axis and the microwave field \vec{B}_1 is applied perpendicular to it along the lab x -axis. In a strong field experiment, the spin \vec{s} precesses about the applied field. **(b)** In an EPR experiment, a microwave field $B_1 = h\nu_1/g\mu_B$ drives transitions between magnetic sublevels that are split by a static Zeeman field B_0 . If the Zeeman field tunes the local hamiltonian so that the microwave field is on resonance (yellow arrows), a signal appears in the spectrum. The intensity of the signal at a resonant B_0 is proportional to the difference in the populations (blue circles) of the involved sublevels. The splitting in B_0 is proportional to the energy splitting at zero-field, ΔE , due to the local magnetic interactions. The spectrum describes the set of all resonances between magnetic sublevels that are split by a given amount of energy; the magnitude of B_1 is constant for all magnitudes of B_0 .

For a two electron system, there are two unpaired electrons in a triplet state and they can occupy one of three $|S = 1, M\rangle$ sublevels—they are both spin up ($M = +1$), both spin down ($M = -1$), or a symmetric linear combination of both up and down ($M = 0$). Microwave radiation ν_1 can promote the system between $\Delta M = \pm 1$ sublevels if the transition is allowed and the resonance condition $\nu_1 = \Delta E(B_0)$ is met, where $\Delta E(B_0)$ is the energy splitting between sublevels for a given hamiltonian (B_0). For the EPR experiments considered, a microwave field \vec{B}_1 is applied perpendicular to \vec{B}_0 , polarized along the lab x -axis (Fig. 1.6a, yellow arrow). The magnitude of the microwave field is labelled B_1 (T)

or ν_1 (Hz), depending on the chosen units, $B_1 = h\nu_1/g\mu_B$. For arbitrary magnitudes of B_0 , the resonance condition will fail, so to collect an EPR spectrum the static field B_0 must be scanned over a range of values that contain all resonances for the system while B_1 is fixed (Fig. 1.6b, yellow and grey arrows). The EPR spectrum is centered about the microwave field $B_1 = h\nu_1/g\mu_B$, which for “X-band” trEPR ($\nu_1 \approx 10$ GHz) is at about 350 mT for $g = 2.0023$.

The intensity of the trEPR spectrum is proportional to the difference in the populations of the sublevels $p_M - p_{M+1}$, where p_M is the population of sublevel M (Fig. 1.6b, blue circles).^{31–33} It is positive for absorption events (A) and negative for emission events (E). By optically pumping the paramagnetic species, the resolution of the trEPR experiment has a considerable advantage over conventional EPR experiments that probe near-thermal populations.

When a Zeeman field is turned on, the zero-field states adiabatically tune in the field, slowly converging to Zeeman sublevels (Fig. 1.6b). Because the ZFS interactions perturb the Zeeman sublevels, the $\Delta M = \pm 1$ energy splittings at a given B_0 differ by an energy proportional to the ZFS energy. In the spectrum, the resonances are shifted along the field axis relative to one another by amounts proportional to the ZFS energy. Because the ZFS interactions have different values along different directions, the resonant field values (B_0) likewise depend on the orientation of the principal axes of the ZFS interactions with respect to the Zeeman field. By systematically rotating the system in the applied Zeeman field, one may map out the distribution of spin interactions and underlying molecular symmetries. This result makes trEPR a powerful tool for characterizing the spatial qualities of molecules.

Consider, for example, the magnetic interaction between two electrons in a triplet state

represented by \mathbf{D} . Suppose further that \mathbf{D} has an axial distribution (Fig. 1.5), so that the interaction is given entirely by its maximum value D and its orientation relative to its z principal axis. The energies of the zero-field states for this two-electron triplet, labelled $|z\rangle$, $|x\rangle$, and $|y\rangle$, are split by $|D|$ (Fig. 1.7).

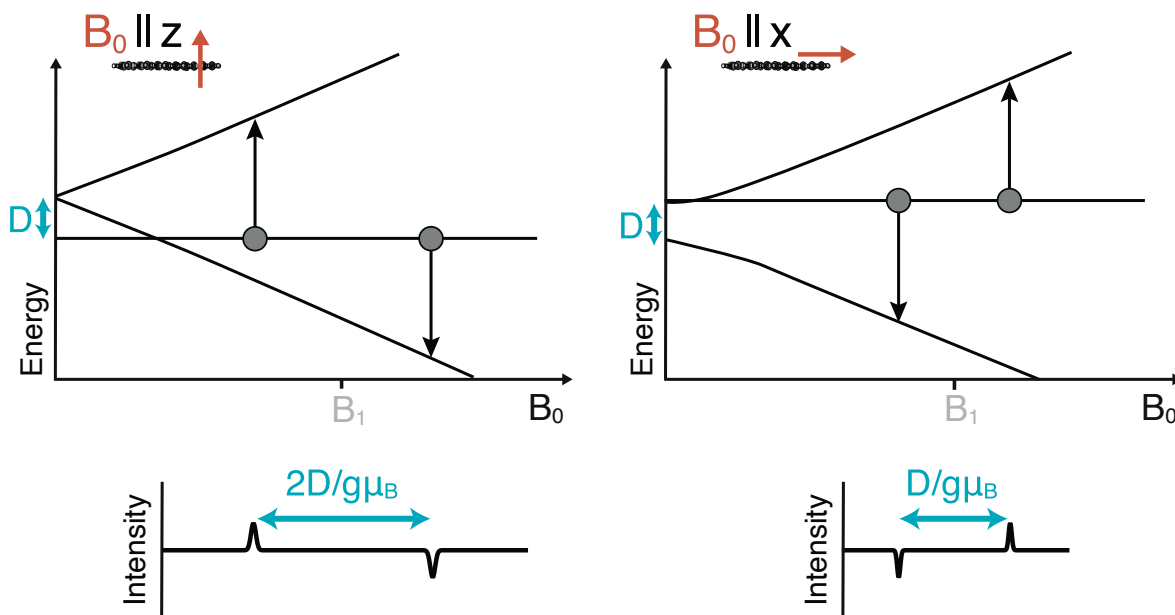


FIGURE 1.7: The triplet trEPR spectrum as a function of orientation. Black lines illustrate the energies of triplet state magnetic sublevels (Fig. 1.6) as a function of an applied Zeeman field B_0 . The direction of the field with respect to the molecular axes z and x is indicated by red arrows. Circles represent sublevel populations and arrows show transitions. When the zero-field dipole interaction \mathbf{D} is axial (Fig. 1.5), the zero-field level $|z\rangle$ is split from the degenerate $|x\rangle$ and $|y\rangle$ sublevels by the magnitude of the interaction, D . For the field along z , two signals appear in the trEPR spectrum that are split by $2D$. For $\vec{B}_0 \parallel x$, the zero-field states converge to different strong-field states and the splitting in the trEPR spectrum is halved.

Suppose now that a strong Zeeman field is applied along the z principal axis of the ZFS interaction, assumed to correspond to the molecular z -axis. When the field is increased, the spins leave their precession about the principal axes and begin to precess about \vec{B}_0 . As the field increases, the zero-field states converge to different linear combinations of

Zeeman states. For $\vec{B}_0 \parallel z$, the field applies no torque to the $|z\rangle$ sublevel so it converges to $|0\rangle$ (Fig. 1.7). Then $|x\rangle = (|-\rangle - |+\rangle)/\sqrt{2}$ and $|y\rangle = i(|-\rangle + |+\rangle)/\sqrt{2}$. If the $|0\rangle$ sublevel is the only sublevel populated, Fig. 1.7 shows that the observed trEPR spectrum has a pair of absorptive and emissive lines split about center field by $2D/g\mu_B$.

If instead the field is applied along the principal x -axis, then the zero-field sublevels converge to different Zeeman sublevels as the field is turned on: $|z\rangle = i(|-\rangle + |+\rangle)/\sqrt{2}$, $|x\rangle = |0\rangle$, and $|y\rangle = |-\rangle - |+\rangle/\sqrt{2}$. For $\vec{B}_0 \parallel x$, the energy of the $|x\rangle$ level is unaffected by the applied field and, as a result, the transitions in the trEPR spectrum are split by half as much as before (Fig. 1.7). If the trEPR experiment probes spin interactions that differ magnetically or spatially, the resulting spectrum will be a sum of spectra from each,²³ and in completely disordered samples the spectra are complex and broad.³⁴

Chapter 2

Singlet Fission for Quantum Information and Quantum Computing: The Parallel JDE Model*

2.1 Abstract

Singlet fission is a photoconversion process that generates a doubly excited, maximally spin entangled pair state. This state has applications to quantum information and computing that are only beginning to be realized. In this Chapter, we construct and analyze a spin-exciton hamiltonian to describe the dynamics of the two-triplet state. We find the selection rules that connect the doubly excited, spin-singlet state to the manifold of quintet states and comment on the mechanism and conditions for the transition into formally independent triplets. For adjacent dimers that are oriented and immobilized in an inert host, singlet fission can be strongly state-selective. We make predictions for electron paramagnetic resonance experiments and analyze experimental data from recent literature. Our results give conditions for which magnetic resonance pulses can drive transitions between optically polarized magnetic sublevels of the two-exciton states, making it possible to realize quantum gates at room temperature in these systems.

*Adapted with permission from Smyser, K. E. & Eaves, J. D. *Sci. Rep.* **10**, 18480, (2020).

2.2 Introduction

In this Chapter we consider singlet fission between chromophores in two classes of systems that are widespread in the literature: covalently linked organic dimer molecules³⁵ and organic crystals comprised of chromophore pairs.¹⁴ As is often the case, the selection rules governing the quantum relaxation phenomena depend sensitively on molecular symmetries. In particular, a pair of identical chromophores, where one molecule is related to the other by a translation (Fig. 2.1b), will also exhibit an exchange symmetry for the exciton triplet pair. As we show, that symmetry isolates the ^3TT triplet states so that spin relaxation only proceeds between ^1TT and ^5TT states. The most state-selective relaxation occurs between the ^1TT singlet state and the $^5\text{TT}_0$ quintet state in an ordered and immobilized system of molecular dimers that have their magnetic principal axes mutually parallel to one another.

2.3 The Spin-Exciton Hamiltonian

We follow with a derivation of the spin-exciton hamiltonian for the triplet pairs in Eq. 1.3, exploiting approximations for the light atom molecules characteristic of singlet fission chromophores. The singlet fission process $S_0S_1 \rightleftharpoons ^1\text{TT}$ (Fig. 1.2) is often much faster (picosecond or sub-picosecond) than the timescales on which the pair states evolve $^1\text{TT} \rightleftharpoons ^{2S+1}\text{TT}_M$ (nanoseconds to microseconds). For singlet fission dimers, the spin-orbit interaction is small and is often ignored, though it is straightforward to include it in the hamiltonian.³⁶ Similarly, the \mathbf{g} -tensors in singlet fission chromophores are often isotropic,⁸ though anisotropy in the \mathbf{g} -tensors can also be included perturbatively.

After making the Born-Oppenheimer approximation, suppressing orbital degrees of freedom, and ignoring hyperfine interactions, we begin with a general hamiltonian that is bilinear in all spin-spin interactions,

$$\mathcal{H} = \frac{1}{2} \sum_{\substack{i,j=1 \\ i \neq j}}^4 \mathbf{s}_i \cdot \mathbf{O}_{ij} \cdot \mathbf{s}_j, \quad (2.1)$$

where \mathbf{s}_i is the electron spin operator for orbital i , and the indices i and j enumerate the HOMO and LUMO levels in a frontier molecular orbital description of the chromophore pair (Fig. 2.1a). \mathbf{O}_{ij} is a rank-two tensor that accounts for the spin-spin interactions between the four electrons in the four orbitals. **Within this framework, \mathbf{O}_{ij} depends implicitly on integrals over spatial wavefunctions** (Sections 3.2.3 and 3.2.4). Akin to electronically nonadiabatic effects in molecules, fluctuations in nuclear coordinates and exciton hopping can make the \mathbf{O}_{ij} time-dependent.^{23,37} These time-dependent \mathbf{O}_{ij} parameters can drive transitions between different spin states of the spin-exciton hamiltonian.

The interaction tensors \mathbf{O}_{ij} for each electron pair can be decomposed into three separate terms: a scalar “isotropic” part, an antisymmetric tensor of rank one, and a traceless, anisotropic tensor of rank two. The isotropic term yields the usual Dirac-Heisenberg exchange coupling.³³ Unlike the isotropic exchange interaction, both the antisymmetric and the anisotropic terms are formally relativistic in nature, and in light-atom molecules they are much smaller than the isotropic term.³⁸ For example, the isotropic exchange interaction in a single pentacene molecule splits the singlet and triplet levels by about 1 eV,⁸ while the anisotropic interaction splits the triplet levels by about 1 GHz, $\approx 10^{-6}$ eV.³⁹ The antisymmetric term is usually negligible in aromatic hydrocarbons and so we ignore it.

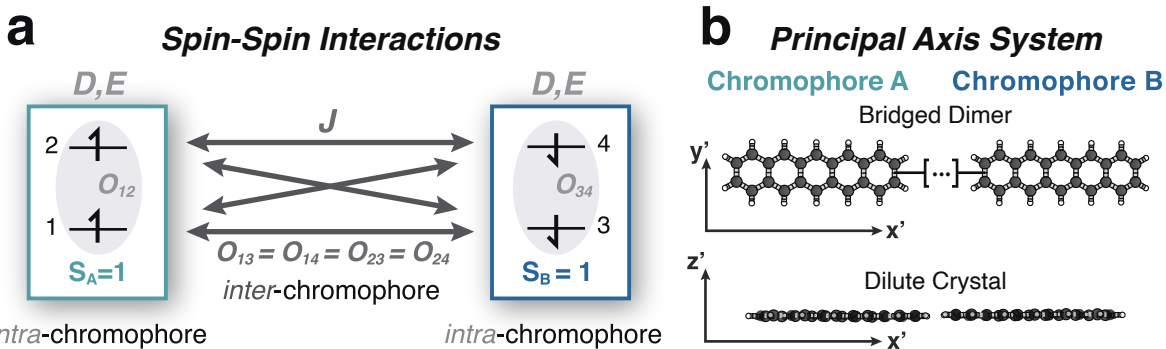


FIGURE 2.1: (a) The products of singlet fission are doubly excited states, with one electron in each frontier molecular orbital (numbered 1-4) of each chromophore (labelled A or B). The spin of each chromophore is a triplet so that $S_A = S_B = 1$. We assume that all *inter*-chromophore isotropic exchange interactions J (double-headed arrows) are equivalent. The *intra*-chromophore interaction is spin-dipole in origin and is characterized by the axial and rhombic EPR parameters, D and E , respectively. In the parallel JDE model, we assume that $D_A = D_B = D$ and $E_A = E_B = E$. This figure is similar in spirit to a picture presented in a recent review, though the nature of the spin-spin interactions there differs from what we present here.⁴⁰ (b) The parallel JDE model describes two translationally invariant chromophores that have all zero-field splitting principal axes (x', y', z') parallel to one another. These chromophores may be covalently linked (top) or doped into a photophysically inactive host matrix (bottom).

To simplify the hamiltonian, we decompose it into intra-chromophore and inter-chromophore interactions (see Section 3.2.2). Because we are not interested in modeling, for example, the transitions between the singlet and triplet state on a single chromophore, we do not include the intra-chromophore isotropic exchange interaction in the hamiltonian. We do, however, keep the *intra*-chromophore anisotropic coupling. We also include the isotropic *inter*-chromophore exchange interaction but discard the much smaller *inter*-chromophore anisotropic coupling. Finally, we set all of the *inter*-chromophore isotropic exchange interactions equal to the same number, J , (see Section 3.2.1). The spin-exciton hamiltonian then takes a compact form,

$$\mathcal{H} = J \mathbf{S}_A \cdot \mathbf{S}_B + H_A + H_B, \quad (2.2)$$

where $\mathbf{S}_A = \mathbf{s}_1 + \mathbf{s}_2$ and $\mathbf{S}_B = \mathbf{s}_3 + \mathbf{s}_4$ are the spin operators associated with chromophores A and B .

The first term in Eq. 2.2 is the isotropic exchange interaction J between two triplet excitons. $H_A = D(S_{Az'}^2 - \mathbf{S}_A^2/3) + E(S_{Ax'}^2 - S_{Ay'}^2)$ and $H_B = D(S_{Bz'}^2 - \mathbf{S}_B^2/3) + E(S_{Bx'}^2 - S_{By'}^2)$ are the hamiltonians associated with the intra-chromophore anisotropic interactions, taken to be of the spin-dipole form, written in the canonical “zero-field splitting” (ZFS) form from EPR literature.³³ The primed coordinates denote the principal axes of the magnetic dipole tensor for chromophore A and chromophore B . The highest symmetry case is the one we analyze here, where all principal directions for chromophore A are parallel to those of chromophore B . Equation 2.2 describes the interactions between two triplet Frenkel spin-excitons, modeled as two spin-1 objects, each one interacting with itself through the spin-dipole interaction and coupled to one another through exchange.

Because the hamiltonian depends only on the parameters J , D , and E and the principal axes of A and B are parallel, we refer to the spin-exciton hamiltonian in equation 2.2 as the parallel *JDE* model. As we will show, restricting the axes of A and B to be parallel imposes symmetries that make relaxation between magnetic sublevels maximally state-selective. All of the parameters in the *JDE* model can either be computed in electronic structure or measured in mixed optical/magnetic resonance experiments.

Hamiltonians similar to Eq. 2.2 have appeared more recently in literature,^{14–17,19,37,41} though researchers either use approximations that make Eq. 2.2 spin-conserving or they analyze it at weak J . Methods of arriving at a spin-conserving *JDE* model differ between authors, but they amount to making an effective spin approximation, such that, for example, $S_{Az}^2 + S_{Bz}^2 \approx S_z^2$. One then discards the isotropic exchange term, which is spin-conserving anyway, and writes the hamiltonian with renormalized D and E parameters,

where the A and B site-spin operators are replaced by total spin operators. The D and E zero-field splitting parameters in crystals are renormalized to the spatially averaged D^* and E^* .^{42,43} In the “strong exchange limit,” $|J|/|D| \gg 1$, D becomes $D/3$, but only for the quintets.¹⁵ Ref. [44]’s “singlet character” approximation is not spin-conserving, but is only appropriate when the Zeeman term (B_0) dominates over J . In the theory for $B_0 > |J|$, the initial and final states are adiabatically connected to one another.³⁷ The theory presented in this Chapter is a nonadiabatic analog that is applicable when J is large. Spin conserving approximations, like the strong or weak exchange approximation, are suitable for work that does not consider transitions between states of different multiplicity. They are manifestly incapable of describing the kind of intersystem crossing, from ${}^1\text{TT}$ to ${}^5\text{TT}_M$ for example, that recent EPR experiments have observed. These newer measurements necessitate the development of the theory presented here.

2.4 Spin Dynamics and Selection Rules at Zero Applied Field

The exchange term $J\mathbf{S}_A \cdot \mathbf{S}_B$ is the largest energy scale in the hamiltonian. It is rotationally invariant and diagonal in the total spin representation. We factor out elements from the JDE hamiltonian (Eq. 2.2) that are functions of the total spin operators, \mathbf{S}^2 and S_z , and are therefore diagonal in the total spin basis $\{|S, M\rangle\}$. These are the reference hamiltonian,

$$H_0 = J\mathbf{S}_A \cdot \mathbf{S}_B + D \left(S_z^2 - \vec{S}^2 / 3 \right). \quad (2.3)$$

The couplings between states of different multiplicity make up V , which is what remains, $V = H - H_0$. The off-diagonal perturbations in V that cause transitions between the states depend solely on D and E ,

$$\begin{aligned} V = & -\frac{2D}{3} (2S_{Az}S_{Bz} - S_{Ax}S_{Bx} - S_{Ay}S_{By}) \\ & - 2E (S_{Ax}S_{Bx} - S_{Ay}S_{By}) \\ & + \frac{E}{2} (S_+^2 + S_-^2). \end{aligned} \tag{2.4}$$

The terms that comprise V are bilinear products of \mathbf{S}_A and \mathbf{S}_B Cartesian spin operators. In the parallel case the largest of these terms $\sim DS_{Az}S_{Bz}$ which has the form of an effective “Zeeman” interaction, where the z -component of the magnetic field produced by exciton spin- A couples to the magnetic dipole of spin- B . This form of the hamiltonian, $H_0 + V$, is equivalent to the hamiltonian given in Eq. 2.2 but facilitates the application of perturbation theory and an intuitive discussion of the results of the JDE model transition theory at zero field.

The energy level diagram for the diagonal states of the reference hamiltonian, H_0 , appears in Fig. 2.2a. States of different multiplicity are split by the large inter-chromophore exchange interaction, J , and for $J < 0$, the singlet state is higher in energy than the triplet and quintet manifolds (Eq. 2.2). The singlet-quintet splitting between ${}^1\text{TT}$ and ${}^5\text{TT}$ is three times the singlet-triplet splitting. The much smaller intra-chromophore axial ZFS interaction, D , splits magnetic, M , sublevels within each manifold. The rhombicity parameter, E —the smallest energy scale in the hamiltonian—is not in H_0 and only couples $\Delta S = 0, \Delta M = \pm 2$ -sublevels at zero field.

When evaluating the hamiltonian, we express it in terms of spherical tensor operators

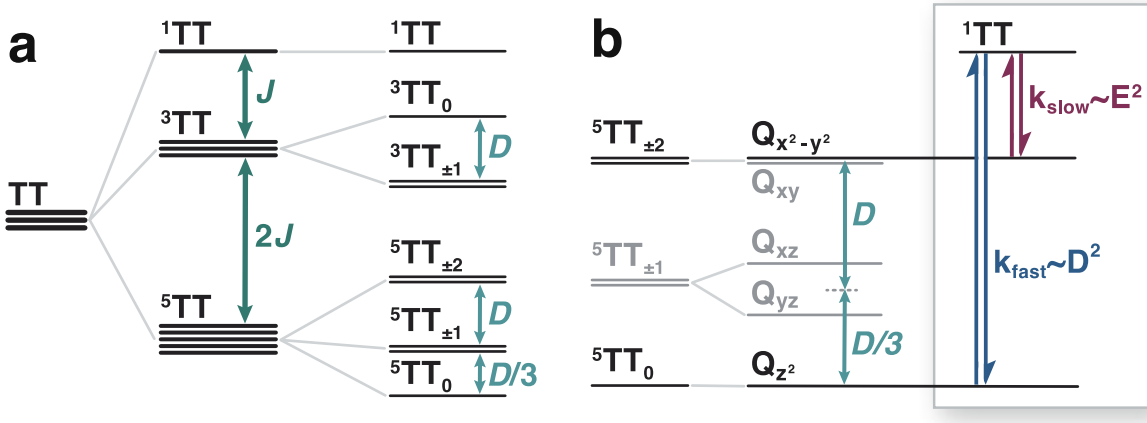


FIGURE 2.2: (a) Energy-level correlation diagram of the JDE model in zero applied field. Interaction energies and splittings decrease in magnitude going from left to right. The sign of J orders the states of total S ; we choose $J < 0$ in analogy to Hund's rule. The choice $D > 0$ corresponds to literature values for pentacene.²³ D is the second largest energy scale and it lifts the degeneracy of states with different magnitudes of the total spin projection quantum number $|M| = 0, 1, 2$. (b) The Q states are linear combinations of degenerate pairs of ${}^5\text{TT}_{\pm M}$ states with Cartesian subscripts that indicate analogies to the d-orbitals. Transitions from ${}^1\text{TT}$ are only allowed to two Q states (black). The Q_{z^2} state may be populated through a non-adiabatically fast interconversion process which goes as $k_{\text{fast}} \sim D^2$. A much slower process $k_{\text{slow}} \sim E^2$ allows transition from the ${}^1\text{TT}$ state to the $Q_{x^2-y^2}$ state.

and apply the Wigner-Eckart theorem (see Section 3.3).⁴⁵ In our evaluation, the “renormalization” of D , for example, to $D/3$ for quintets (Fig. 2.2a), is a direct consequence of the Wigner-Eckart theorem. We assume that the ZFS, D and E parameters are independent of nuclear coordinates and that the time-dependent nuclear motion appears in J . A recent paper that numerically simulates spin dynamics in singlet fission in Ref. [37] makes a similar approximation.

The application of the Wigner-Eckart theorem to the hamiltonian in Eq. 2.2 also shows that transitions from ${}^1\text{TT}$ to ${}^5\text{TT}_0$ and ${}^5\text{TT}_{\pm 2}$ are allowed while all other transitions from ${}^1\text{TT}$ are forbidden (Section 3.3.7). Motivated by degenerate perturbation theory, we form

symmetric and antisymmetric combinations of the $\pm M$ -states of the degenerate hamiltonian (Fig. 2.2b). For example, forming linear combinations from the sums and differences of each pair of degenerate states,⁴⁴

$$\begin{aligned} |Q_{x^2-y^2}\rangle &= \frac{1}{\sqrt{2}} (|{}^5\text{TT}_{+2}\rangle + |{}^5\text{TT}_{-2}\rangle) = \frac{1}{\sqrt{2}} (|xx\rangle - |yy\rangle) \\ |Q_{xy}\rangle &= \frac{1}{\sqrt{2}} (|{}^5\text{TT}_{+2}\rangle - |{}^5\text{TT}_{-2}\rangle) = \frac{i}{\sqrt{2}} (|xy\rangle + |yx\rangle) \\ |Q_{xz}\rangle &= \frac{1}{\sqrt{2}} (|{}^5\text{TT}_{+1}\rangle - |{}^5\text{TT}_{-1}\rangle) = -\frac{1}{\sqrt{2}} (|xz\rangle + |zx\rangle) \\ |Q_{yz}\rangle &= \frac{1}{\sqrt{2}} (|{}^5\text{TT}_{+1}\rangle + |{}^5\text{TT}_{-1}\rangle) = -\frac{i}{\sqrt{2}} (|yz\rangle + |zy\rangle) \\ |Q_{z^2}\rangle &= |{}^5\text{TT}_0\rangle = \frac{1}{\sqrt{6}} (2|zz\rangle - |xx\rangle - |yy\rangle), \end{aligned} \quad (2.5)$$

breaks the degeneracy of the ${}^5\text{TT}_{\pm 1}$ states by $2|E|$ (Fig. 2.2b). These linear combinations of the M -sublevels are analogous to those of the $\ell = 2$ spherical harmonics that are taken to construct the d-orbitals,⁴⁶ and so we label the states accordingly (Fig. 2.2b). The states labelled by Cartesian coordinates are product states of the single exciton “zero-field states” that diagonalize the single-exciton ZFS hamiltonian. The labels correspond to the principal axis directions of the ZFS interaction, in which the interaction lies solely along these axes.³³ The product states, however, are not the eigenstates of $H_{ZFS} = H_A + H_B$.⁴⁴

The first term in V (Eq. 2.4) is of similar form to the $|Q_{z^2}\rangle$ state (Eq. 2.5) and couples it to the $|{}^1\text{TT}\rangle$ state by $|\langle {}^1\text{TT}|V|Q_{z^2}\rangle| \sim D$; the second term couples the $|{}^1\text{TT}\rangle$ state to the $|Q_{x^2-y^2}\rangle$ state by $|\langle {}^1\text{TT}|V|Q_{x^2-y^2}\rangle| \sim E$; and the third term in V weakly mixes the non-degenerate quintet states, $|Q_{z^2}\rangle$ and $|Q_{x^2-y^2}\rangle$ so weakly that we ignore it. All other singlet-quintet coupling elements go to zero in this basis. The state-selectivity follows from the symmetries of how the Cartesian Q -states, rather than the Zeeman $|S, M\rangle$ states,

transform under the rotation operations that characterize the symmetries of the zero-field hamiltonian (Section 3.3.5).

In a rate theory for relaxation, the relaxation rate from ^1TT to Q_{z^2} is proportional to D^2 and the rate from ^1TT to $Q_{x^2-y^2}$ is proportional to E^2 . Because $|D| \gg |E|$, the dominant relaxation channel is from ^1TT to Q_{z^2} (Fig. 2.2b). These selection rules are strict for identical chromophores with parallel symmetry, but upon breaking this symmetry, transitions from the quintet ^5TT to the triplet manifold ^3TT become allowed while transitions from the ^1TT to the ^3TT manifold remain forbidden. In the absence of parallel symmetry, transitions also become allowed between ^1TT and all of the quintet sublevels.

Equation 2.2 can describe how the unpairing of ^1TT to independent triplets $\text{T} + \text{T}$ takes place (Eq. 1.4).³⁷ By measuring quantum beats in delayed fluorescence spectra, Ref. [11] showed, rather convincingly, that exciton unpairing can occur in crystalline tetracene. In a crystal, the exciton hopping rate is fast. As a result, J , which depends sensitively on the distance between chromophores, will rapidly go to zero. This scenario can be modeled using a quantum quench with the time-dependent hamiltonian $\mathcal{H}(t) = H_A + H_B + (1 - \theta(t))J\mathbf{S}_A \cdot \mathbf{S}_B$, where $\theta(t)$ is the Heaviside step function, and the quench occurs for $t > 0$. After the initial transients associated with decoherence and population relaxation phenomena subside, detailed balance shows that the system's reduced density matrix will factorize into a thermal product state. Because H_A and H_B commute, at times that are long compared to the spin relaxation times the density matrix becomes $\rho \sim \exp(-\beta H) / Z = \exp(-\beta H_A) \exp(-\beta H_B) / Z_A Z_B = \rho_A \otimes \rho_B$. The two triplet exciton states become formally independent.

Exciton entanglement diminishes as J becomes smaller. This implies that dimers will preserve entanglement on longer timescales than crystals with mobile excitons. In

tetracene crystals, the loss of coherence has been observed to occur on timescales of tens of nanoseconds, which is not much longer than the quantum gate switching times given by the inverse characteristic EPR transition frequencies.¹¹ Once thermalized, these two triplets offer no quantum advantage over single triplets prepared through more standard intersystem crossing processes.

For quantum information applications, one should focus attention on dimers where chromophores are covalently bound or packed together as a minority component in a crystal so that the exciton hopping rate to the host is negligible.¹⁴ We refer to the latter category as a “dilute crystal.” In these systems, J may fluctuate about a nonzero value, but it cannot go to zero. We impose the condition that $|J| \gg |D|$. For organic chromophores, such as polyacenes, it is also often the case that $|D| \gg |E|$.

In dimers, transitions can occur from rare fluctuations of the bare energy gaps between states of total $|S, M\rangle$. These fluctuations are driven by nuclear motions, and we assume that the energy gap embodied in a time-dependent J obeys Gaussian statistics. This scenario is valid so long as $|J| \gg |D|$ and the energy gap obeys linear response with respect to the nuclear motions. The resulting theory is completely analogous to Marcus’ theory of nonadiabatic electron transfer and the Förster-Dexter theory of exciton hopping, where the ZFS parameters play the role of the nonadiabatic coupling matrix elements. Transitions between initial and final states take the form $k_{i \rightarrow f} = F |\langle i | V | f \rangle|^2$, where F is a Franck-Condon weighted density of states. In principle, F incorporates a thermal factor between the various final states that is the result of summing over nuclear fluctuations. Detailed balance, however, gives the condition that $k_{i \rightarrow f} / k_{f \rightarrow i} = \exp(-\beta(E_i - E_f))$. Given that the various quintet states are split by about 0.05 cm^{-1} , ignoring the temperature dependence of the prefactor is a safe approximation for temperatures above about 1 K. It is a

straightforward matter to extend this analysis to a case where $|J| < |D|$, by first diagonalizing the JDE hamiltonian and then applying second-order perturbation theory in the exciton-heat bath coupling. This approach would resonate closely with the much earlier work in Ref. [47] on delayed fluorescence in molecular crystals that has since been applied to recent experiments.¹³

2.5 EPR Spectroscopy

Recent experiments have employed an optical pump/EPR probe scheme to observe the fate of exciton polarization following singlet fission.^{15–22,37,48} Many of these experiments use field-swept EPR as the probe, where the system is subjected to a static magnetic field, \mathbf{B}_0 , along the laboratory z -axis. The static field splits the magnetic sublevels while an oscillatory microwave field, \mathbf{B}_1 , polarized in the xy -plane, induces transitions between them. In these experiments, one finds resonances as a function of the static field strength, B_0 .

Many experiments use X-band EPR (8-12 GHz) and for small organic chromophores this is in the strong field limit, where states are split by much more than D . To model these experiments, we introduce the Zeeman term, $H_{Zeeman} = g\mu_B B_0 S_z$, into Eq. 2.2 and choose the quantization axis along the lab, or Zeeman, z -axis (see Section 3.3.2). The static Zeeman field splits states of different M but not states of different S ; the ^1TT state is unaffected by the Zeeman field.

Because the Zeeman field induces splittings that are large compared to those of H_{ZFS} , the reference hamiltonian, H_0 , changes. To construct it, we first project out the quintet block to find its eigenstates, $|\alpha\rangle = \sum_M c_{M,\alpha} |^5\text{TT}_M\rangle$. These states, the adiabats (Fig. 2.4b),

adiabatically follow B_0 . The hamiltonian is then re-expressed in the adiabatic basis, with the reference hamiltonian, $H_0 = \sum_{\alpha} |\alpha\rangle\epsilon_{\alpha}\langle\alpha|$, and coupling to $|^1\text{TT}\rangle$ defined accordingly. Transitions occur between the adiabatic sublevels and have a spectrum given by the Golden Rule $I = \sum_{\alpha,\beta} |\langle\alpha|S_x|\beta\rangle|^2(P_{\alpha} - P_{\beta})\delta(\epsilon_{\alpha} - \epsilon_{\beta})$,⁴⁹ where $P_{\alpha} = \text{Tr}(\rho|\alpha\rangle\langle\alpha|)$ is the population in state $|\alpha\rangle$. More details appear in Section 3.4. While the time-dependence of the populations can be, and has been, measured, we focus attention on the “prompt” EPR spectrum that interrogates the initial population of the exciton magnetic sublevels immediately following singlet fission, where the short-time approximation $P_{\alpha} \sim |\langle^1\text{TT}|H|\alpha\rangle|^2$ is valid. With these provisions in place, there are no adjustable parameters for the calculated EPR spectra.

Changing the orientation of the dimer relative to the Zeeman field results in a perturbative change in the hamiltonian. The transitions from ${}^1\text{TT}$ to the ${}^5\text{TT}_{\pm 1}$ sublevels, that were once symmetry forbidden, are now allowed and state selectivity diminishes. For dimers in a powder or frozen solution, the EPR signal is a sum over an ensemble of molecules that have a broad distribution of orientations with respect to the Zeeman field. The resulting spin polarization is scrambled, which leads to decoherence in the ensemble signal. In quantum information applications this is a source of noise, and it is therefore important not only to fix the molecular axes relative to one another, but also with respect to the laboratory axis.

For dimers with their principal axes fixed in space, the prompt EPR spectra as a function of the polar angle, θ , between z and z' , exhibit different numbers of peaks with different frequencies and signed relative intensities (Fig. 2.3). The coupling term, V , is a function of θ , and all quintet states may be directly accessible from the ${}^1\text{TT}$ state. There is intensity-borrowing from the ${}^5\text{TT}_0$ and ${}^5\text{TT}_{\pm 2}$ zero-field states into all ${}^5\text{TT}_M$ sublevels

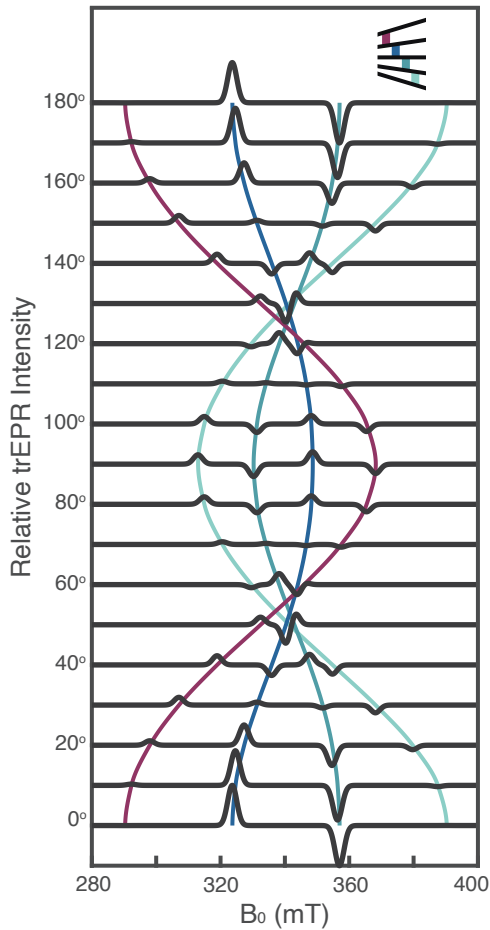


FIGURE 2.3: θ is the polar angle between the lab-fixed Zeeman axis and the principal z' -axis. Peak intensities are proportional to differences in state populations and are relative to intensities at $\theta = 0^\circ$. Differences in the number and sign of the peaks are the result a θ -dependent coupling between the $|^1\text{TT}\rangle$ and the adiabatic $|\alpha\rangle$ states described in the text. Colored lines follow specific transitions, indicated in the inset where states are ordered in energy with respect to the applied field. The parameters used to calculate the spectra are consistent with those reported in Fig. 2.4, where we discuss the spectrum for $\theta = 90^\circ$.

as a function of θ . As θ goes from 0° to 90° , state selectivity for the relaxation from ${}^1\text{TT}$ monotonically decreases. The EPR signal is a much weaker function of the azimuthal angle, ϕ .

Reference [14] published TT EPR spectra for dilute crystals of pentacene molecules doped into a *p*-terphenyl matrix. The pentacene molecules adopted both parallel and herringbone configurations in the host, as observed in the pentacene crystal structure. This elegant design allowed them to disperse the dimers and fix their orientations in space. The ${}^5\text{TT}$ EPR spectrum contains contributions from dimers in both parallel and herringbone geometries. Figure 2.4a shows the field-swept energies of ${}^5\text{TT}_M$ states for parallel chromophores, where the Zeeman field, B_0 , is directed along the principal x' -axis, which is the most well-resolved spectrum in their paper. On this diagram, we indicate the diabats which are pure $|S, M\rangle$ states, along with the adiabats described above (Fig. 2.4b). The transitions occur in the strong field limit, far from the avoided crossings between the adiabats, which occur at much smaller values of the B_0 field. Indeed, in the vicinity in which the EPR transitions are recorded, the diabats and adiabats very nearly coincide.

We present our calculation for the prompt EPR spectrum in Fig. 2.4c using the parameters from Ref. [14]. As Fig. 2.4a and 2.4c show, our model fits their data extremely well for the quintet part of the spectrum (left panel of Fig. 6 in Ref. [14]), with one caveat. The polarization pattern (AEAE) we calculate for parallel molecules (Fig. 2.4c) matches the polarization of the spectrum that Ref. [14] assigned to the herringbone configuration. This is because Ref. [14] included an anisotropic inter-exciton exchange coupling and treated the populations as fit parameters. Ref. [14] did find, however, that setting the populations in quintet $M = \pm 1$ levels to zero produced the best fit to the spectrum. This result is completely consistent with the selection rules derived here with $B_0||x'$.

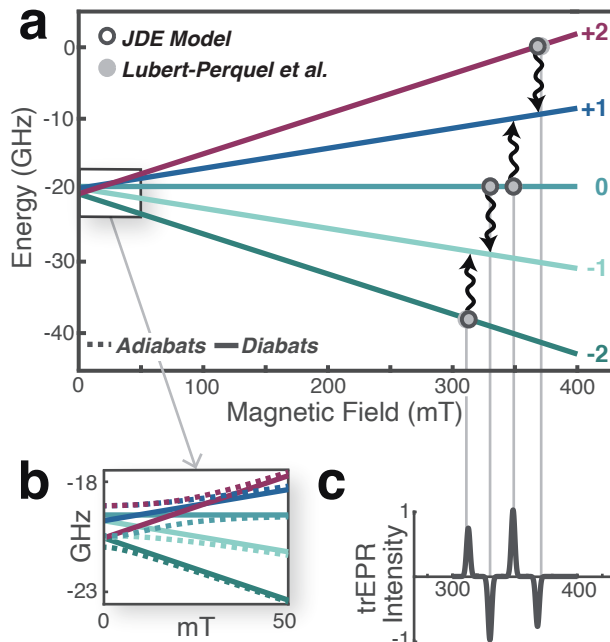


FIGURE 2.4: (a) The energies of diabatic quintet states as a function of the Zeeman field. Parameters used are literature values for parallel pentacene molecules in *p*-terphenyl.¹⁴ The experiments performed in Ref. [14] are in the strong field limit, where the transitions are far removed from the avoided crossings between adiabatic states (b). In this limit, the diabatic states (solid lines) of the Zeeman hamiltonian are very close to the adiabatic states (dashed lines). Open circles indicate computed transitions which compare favorably to the field values of transitions reported by Ref. [14] (closed circles). With $B_0||x'$, the ^1TT state transfers only to the quintet $M = 0, \pm 2$ states. Wavy arrows indicate the direction of transitions for $D > 0$. (c) Simulated prompt EPR spectrum, where positive changes in the intensity indicate induced absorption and negative changes indicate stimulated emission. The relative peak intensities were calculated from coupling matrix elements between the singlet and quintet states using a short-time approximation to the Pauli master equation. These populations reproduce the *AEAE* polarization pattern for the quintet part of the spectrum reported in Ref. [14].

2.6 Discussion

We have provided a derivation and an analysis of a model hamiltonian for singlet fission with an eye toward quantum computing, information, and sensing applications. The model is specified by only three parameters: the inter-chromophore isotropic exchange coupling, J , and the intra-chromophore ZFS axial parameter, D , and rhombicity parameter, E . These parameters can be measured independently or calculated using electronic structure. The model one arrives at under a set of reasonable approximations is something we call the *JDE* model, named for the J , D , and E parameters of that hamiltonian.

In particular, we have shown that one can use the magnetic sublevels of the ${}^5\text{TT}$ space as “qudits” in quantum information applications,⁵⁰ where EPR experiments perform the function of quantum gates. The five quintet states offer a quantum advantage over the three states of the spin-polarized triplets, produced either by intersystem crossing or as the final spin unpaired products of a singlet fission process in a crystal. We have shown the conditions under which the ${}^1\text{TT}$ state transfers to states in the quintet block and have given the conditions for maximal state selectivity, and thereby the most efficient pathway to optical spin polarization for those transitions.

To decrease the transition rates from the ${}^{2S+1}\text{TT}_M$ manifold into the incoherent unpaired triplets, one needs to keep the value of J large. This implies that molecular dimers that are covalently bound to one another or doped as an impurity component into a host crystal are ideal candidates for generating optically spin-polarized quantum states near room temperature.

We have identified, for the first time, the selection rules for relaxation between the various doubly excited TT levels in chromophores with parallel symmetry at both zero

and large Zeeman fields. At zero field, fluctuations in J transfer population from the ^1TT state into the highly entangled quintet state, Q_{z^2} . This transition rate goes as D^2 . There is one and only one other allowed transition, which is into the $Q_{x^2-y^2}$ state, but this rate is proportional to E^2 and is much slower. One can make the relaxation even more state selective by synthesizing molecules with large $|D|/|E|$ ratios.

In the strong field conditions, characteristic of both time-resolved field swept EPR experiments and quantum computing applications, we find that relaxation can be kept state-selective provided that the principal axes of the two chromophores are parallel to each other and to the Zeeman field. When a molecule's principal z' -axis does not align with the Zeeman axis, several symmetries are broken, and transitions are possible to all sublevels in the quintet block. In samples where the molecules have a broad distribution of orientations relative to the Zeeman axis, the ensemble will exhibit decoherence. This is a different source of decoherence than, for example, inhomogeneous broadening, that can be removed through echo techniques. This means that one needs to also devise a method to immobilize and control the orientation of the singlet fission chromophores. Recent, elegant, experimental work has shown that this is possible.¹⁴

Finally, using our model and analysis, we calculated the prompt EPR spectra of pentacene dimers doped into a *p*-terphenyl crystal to compare with the experimental measurements reported in Ref. [14]. With the parameters J , D , and E provided, there are no adjustable parameters in this calculation. The results match the major features of the measured quintet spectrum, including the polarization pattern (AAE), very well.

Singlet fission can create strongly spin-polarized products and thereby generate nearly pure quantum states at room temperature, but there are several design principles that one should follow. First, keep the inter-chromophore exchange, J , large. Second,

immobilize the molecules and align their principal axis to the Zeeman field. Both requirements are satisfied in immobilized and oriented, covalently linked dimers, or in dimer pairs that are embedded in a crystal host that inhibits exciton diffusion.¹⁴

Singlet fission can offer many of the quantum advantages found in color centers, like the NV center in diamond, but with a bottom-up approach to design that is currently unavailable in color centers whose defects are implanted in the material post-synthesis. Singlet fission, in contrast, is able to capitalize on the arsenal of synthetic techniques developed in organic chemistry to design molecules. This work provides a quantitative model for computing dynamics and fitting spectra, and qualitative design principles for the synthetic design of new organic molecules for quantum information applications. This is an important step in establishing the relationship between molecular structure and function in an emerging class of organic, novel quantum materials.

Chapter 3

The *JDE* Model Formalism

3.1 Model Development

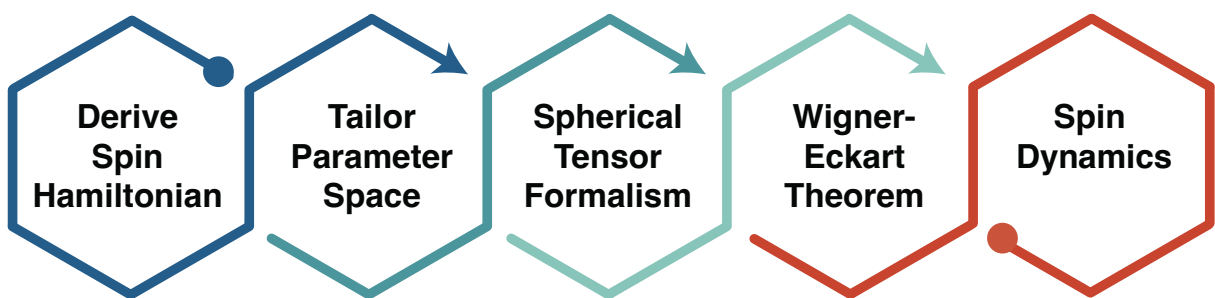


FIGURE 3.1

Step 1: Derive the biexciton hamiltonian from the all-electron spin-exciton hamiltonian from Chapter 2. In the absence of spin-orbit coupling, the wavefunction factorizes into spin and spatial (orbital) components. After integrating over spatial components, the spins interact through an effective hamiltonian. Quite generally, the interactions must be bilinear in the spins.

Step 2: Write the model hamiltonian as a sum of different spin-spin interaction hamiltonians. The parameters of these hamiltonians can be measured or calculated, forming a rational connection between molecular structure and the emergent exciton

spin dynamics of the triplet pair. Based on the relative magnitudes of reported values for the interactions and, by exploiting symmetries specifically for singlet fission dimers, reduce the parameter space of the model hamiltonian to a minimal set.

Step 3: Write the simplified model hamiltonian in the spherical tensor representation. In the next step the matrix elements are evaluated based on the rotational symmetries of spin operators, spin states, and spin-spin interactions.

Step 4: Use the Wigner-Eckart theorem to analyze the matrix elements of the *JDE* model hamiltonian in the total spin basis. A direct result are the selection rules for relaxation pathways between the initially formed singlet pair state and the various high-spin pair sublevels.

Step 5: The *JDE* hamiltonian is a low energy approximation to a fully relativistic hamiltonian. The true eigenstates of this system are the fully relativistic states, so in the model representation, interactions can actually change the angular momentum. This is witnessed for some dimers in the trEPR spectrum immediately following singlet fission (\sim ns). Given the model hamiltonian and nature of these states, develop a theory for transitions between them. By developing state-to-state kinetics through first-order perturbation theory, this illustrates the role that interactions play in pair state dynamics. Using this theory, calculate the trEPR spectrum with home-built software written in the Julia programming language.

3.2 The JDE Spin-Exciton Hamiltonian in Cartesian Space

This Section aims to develop an understanding of the spin-exciton hamiltonian from Chapter 2 (Eq. 2.2) and introduces the concept of tensors. First, it provides a more explicit derivation of the *JDE* model hamiltonian and then discusses the spin-spin interactions relevant to the singlet fission chromophores for quantum computing applications. To conclude, selection rules are derived from two discrete symmetry operations, exchange and parity.

3.2.1 Deriving JDE Model Hamiltonian

The electron-hole pair called a Frenkel, or molecular exciton, is localized to one chromophore. The spatial wavefunction of the two-triplet state is therefore also expected to be tightly bound. As a result, we expect that each chromophore behaves as a spin-1 object. These are spin centers A and B with spin operators,

$$\begin{aligned}\mathbf{S}_A &= \mathbf{s}_1 + \mathbf{s}_2, \\ \mathbf{S}_B &= \mathbf{s}_3 + \mathbf{s}_4,\end{aligned}\tag{3.1}$$

where indices 1-4 denote the electrons belonging to the individual spin centers. The energy from two interacting spins can be described by a “bilinear” spin hamiltonian. For

example, the hamiltonian that describes all inter-chromophore interactions is,

$$\begin{aligned} H_{AB} &= \mathbf{S}_A^\top \cdot \mathbf{O}_{AB} \cdot \mathbf{S}_B \\ &= (S_{Ax} \ S_{Ay} \ S_{Az}) \begin{pmatrix} O_{xx} & O_{xy} & O_{xz} \\ O_{yx} & O_{yy} & O_{yz} \\ O_{zx} & O_{zy} & O_{zz} \end{pmatrix} \begin{pmatrix} S_{Bx} \\ S_{By} \\ S_{Bz} \end{pmatrix}. \end{aligned} \quad (3.2)$$

In the second line of Eq. 3.2, a 3×3 Cartesian matrix is used to represent *all* inter-chromophore interactions (e.g., dipole-dipole, exchange, spin-orbit) between spin-centers A and B . Throughout the text, objects and interactions with vector representations are indicated with over-arrows and those with matrix representations are in bold. Operators are also shown in bold.

Equation 3.2 comes from the all-electron spin hamiltonian from Chapter 2 (Eq. 2.1), restated here for convenience,

$$\mathcal{H} = \frac{1}{2} \sum_{\substack{u,v=1 \\ u \neq v}}^4 \mathbf{s}_u^\top \cdot \mathbf{O}_{uv} \cdot \mathbf{s}_v, \quad (3.3)$$

where \mathbf{s}_u is the electron spin operator for orbital u , and the indices u and v enumerate the HOMO and LUMO levels in a frontier molecular orbital description of the chromophore pair (Fig. 2.1a). \mathbf{O}_{uv} is a matrix that represents the spin-spin interactions between the two electrons in orbitals u and v . To arrive at Eq. 3.2, the sum in Eq. 3.3 is first expanded

and then terms are grouped into inter-chromophore and intra-chromophore hamiltonians, H_{AB} , H_A , and H_B , respectively,

$$\begin{aligned}\mathcal{H} &= \mathbf{s}_1^\top \cdot \mathbf{O}_{13} \cdot \mathbf{s}_3 + \mathbf{s}_1^\top \cdot \mathbf{O}_{14} \cdot \mathbf{s}_4 + \mathbf{s}_2^\top \cdot \mathbf{O}_{23} \cdot \mathbf{s}_3 + \mathbf{s}_2^\top \cdot \mathbf{O}_{24} \cdot \mathbf{s}_4 \\ &\quad + \mathbf{s}_1^\top \cdot \mathbf{O}_{12} \cdot \mathbf{s}_2 + \mathbf{s}_2^\top \cdot \mathbf{O}_{24} \cdot \mathbf{s}_4 \\ &= \mathbf{s}_1^\top \cdot \mathbf{O}_{13} \cdot \mathbf{s}_3 + \mathbf{s}_1^\top \cdot \mathbf{O}_{14} \cdot \mathbf{s}_4 + \mathbf{s}_2^\top \cdot \mathbf{O}_{23} \cdot \mathbf{s}_3 + \mathbf{s}_2^\top \cdot \mathbf{O}_{24} \cdot \mathbf{s}_4 \\ &\quad + H_A + H_B.\end{aligned}\tag{3.4}$$

The intra-chromophore hamiltonians for chromophores A and B (Fig. 2.1) are defined as $H_A \equiv \mathbf{s}_1^\top \cdot \mathbf{O}_{12} \cdot \mathbf{s}_2$ and $H_B \equiv \mathbf{s}_3^\top \cdot \mathbf{O}_{34} \cdot \mathbf{s}_4$. To write H_{AB} , I exploit Hückel Molecular Orbital theory that says for identical atoms the HOMO and LUMO orbitals differ only by phase, $\mathbf{O}_{13} = \mathbf{O}_{14} = \mathbf{O}_{23} = \mathbf{O}_{24} \equiv \mathbf{O}_{AB}$. Then the hamiltonian is further simplified by considering Eq. 3.1,

$$\begin{aligned}\mathcal{H} &= \mathbf{s}_1^\top \cdot \mathbf{O}_{13} \cdot \mathbf{s}_3 + \mathbf{s}_1^\top \cdot \mathbf{O}_{14} \cdot \mathbf{s}_4 + \mathbf{s}_2^\top \cdot \mathbf{O}_{23} \cdot \mathbf{s}_3 + \mathbf{s}_2^\top \cdot \mathbf{O}_{24} \cdot \mathbf{s}_4 + H_A + H_B \\ &= \mathbf{s}_1^\top \cdot \mathbf{O}_{AB} \cdot (\mathbf{s}_3 + \mathbf{s}_4) + \mathbf{s}_2^\top \cdot \mathbf{O}_{AB} \cdot (\mathbf{s}_3 + \mathbf{s}_4) + H_A + H_B \\ &= (\mathbf{s}_1 + \mathbf{s}_2)^\top \cdot \mathbf{O}_{AB} \cdot (\mathbf{s}_3 + \mathbf{s}_4) + H_A + H_B \\ &= \mathbf{S}_A^\top \cdot \mathbf{O}_{AB} \cdot \mathbf{S}_B + H_A + H_B \\ &= H_{AB} + H_A + H_B.\end{aligned}\tag{3.5}$$

In summary,

$$\begin{aligned} H_A &= \mathbf{s}_1^\top \cdot \mathbf{O}_{12} \cdot \mathbf{s}_2 \\ H_B &= \mathbf{s}_3^\top \cdot \mathbf{O}_{34} \cdot \mathbf{s}_4 \\ H_{AB} &= \mathbf{S}_A^\top \cdot \mathbf{O}_{AB} \cdot \mathbf{S}_B. \end{aligned} \tag{3.6}$$

3.2.2 Introduction to Tensor Formalism

The \mathbf{O} matrices in Eq. 3.6 are a representation of a more abstract object called a tensor—a basis-independent mathematical object that can be used to describe physical properties. Tensors are indexed by their rank, k , which describes the number of directional spaces they span simultaneously. For example, the representation of a rank- k tensor in a 3-dimensional space is described by 3^k values. When indexed by x , y , and z , like in Eq. 3.2, the \mathbf{O} refer to Cartesian tensors that are defined with respect to Euclidean space.

The Cartesian tensor in Eq. 3.2 is written in a most general form, where all of the matrix elements are assumed to be independent. In this form, it is difficult to meaningfully associate these parameters, or matrix elements, with measured or calculated values for the energies of physical interactions. The matrix in Eq. 3.2 is an example of a *reducible* tensor. To assign the tensors meaningfully to spin-spin interactions, I continue by breaking down the reducible Cartesian tensors into parts that have specific symmetries,

$$\begin{aligned} \mathbf{O} &= \mathbf{O}_{\text{symmetric}} + \mathbf{O}_{\text{antisymmetric}} \\ &= \frac{1}{2} (\mathbf{O} + \mathbf{O}^\top) + \frac{1}{2} (\mathbf{O} - \mathbf{O}^\top). \end{aligned} \tag{3.7}$$

The symmetric part of Eq. 3.7 may be further reduced,

$$\begin{aligned}\mathbf{O} = & \frac{1}{3}\text{Tr}(\mathbf{O}) + \left[\frac{1}{2}(\mathbf{O} + \mathbf{O}^T) - \frac{1}{3}\text{Tr}(\mathbf{O}) \right] && (\text{symmetric}) \\ & + \frac{1}{2}(\mathbf{O} - \mathbf{O}^T) && (\text{antisymmetric}).\end{aligned}\quad (3.8)$$

Each part is referred to as an *irreducible* tensor of rank $k \in \{0, 1, \dots, k-1, k\}$,⁵¹

$$\mathbf{O} = \left[\frac{\text{Tr}(\mathbf{O})}{3} \mathbf{1} \right]^{(k=0)} + \left[\frac{1}{2}(\mathbf{O} - \mathbf{O}^T) \right]^{(k=1)} + \left[\frac{1}{2}(\mathbf{O} + \mathbf{O}^T) - \frac{\text{Tr}(\mathbf{O})}{3} \mathbf{1} \right]^{(k=2)}, \quad (3.9)$$

where $\mathbf{1}$ is the identity matrix. Specific spin interactions are assigned to the irreducible tensors $\mathbf{O}^{(k)}$ by considering their symmetries under rotation.

Rank- k irreducible tensors are entirely described by $2k+1$ independent parameters. Irreducible rank-0 tensors have a scalar (isotropic) representation, $\mathbf{O}^{(0)} = \text{Tr}(\mathbf{O})/3$. Although, later it will prove helpful to instead consistently use matrix representations for all interactions,

$$\mathbf{O}^{(0)} = \frac{\text{Tr}(\mathbf{O})}{3} \begin{pmatrix} 1 & 0 & 0 \\ 0 & 1 & 0 \\ 0 & 0 & 1 \end{pmatrix}. \quad (3.10)$$

Interactions with irreducible rank-one representations are spatially antisymmetric, $\mathbf{O}^T(1) = -\mathbf{O}^{(1)}$. In matrix form they are defined as,

$$\mathbf{O}^{(1)} = \begin{pmatrix} 0 & \delta_{xy} & \delta_{xz} \\ -\delta_{xy} & 0 & \delta_{yz} \\ -\delta_{xz} & -\delta_{yz} & 0 \end{pmatrix}, \quad (3.11)$$

where $\delta_{ij} = (O_{ij} - O_{ji}) / 2$. They are described by three unique parameters and consequentially can also be represented by a vector. The irreducible rank-two term in Eq. 3.9 has a 3×3 matrix representation,

$$\mathbf{O}^{(2)} = \begin{pmatrix} \sigma_{xx} & \sigma_{xy} & \sigma_{xz} \\ \sigma_{xy} & \sigma_{yy} & \sigma_{yz} \\ \sigma_{xz} & \sigma_{yz} & \sigma_{zz} \end{pmatrix}, \quad (3.12)$$

where $\sigma_{ij} = (O_{ij} + O_{ji}) / 2$. It is symmetric, $\mathbf{O}^T{}^{(2)} = \mathbf{O}^{(2)}$, and traceless, $\sigma_{xx} + \sigma_{yy} + \sigma_{zz} = 0$, so that it is completely described by five parameters. The values of the $\mathbf{O}^{(2)}$ interactions are different for different directions so they are often referred to as anisotropic.

The inter- and intra-chromophore spin hamiltonians are bilinear because they are linear in the spins, separately. Because the elements of \mathbf{O} are scalar values, we may rewrite the spin-spin hamiltonians as the scalar tensor product between the interaction tensor \mathbf{O} and the dyadic product of spin tensors. For example, consider again the inter-chromophore spin hamiltonian (Eq. 3.6),

$$\begin{aligned} H_{AB} &= \mathbf{S}_A^\top \cdot \mathbf{O}_{AB} \cdot \mathbf{S}_B \\ &= \sum_{i,j=x,y,z} S_{Ai} O_{ABij} S_{Bj} \\ &= \sum_{i,j=x,y,z} O_{ABij} S_{Ai} S_{Bj} \\ &= \mathbf{O}_{AB} : (\mathbf{S}_A \otimes \mathbf{S}_B^\top). \end{aligned} \quad (3.13)$$

Here I have introduced new notation for two operations: (1) the dyadic, or tensor, product of spin operators is a matrix and is defined as,

$$(\mathbf{S}_A \otimes \mathbf{S}_B^\top) = \begin{pmatrix} S_{Ax} \\ S_{Ay} \\ S_{Az} \end{pmatrix} (S_{Bx} \quad S_{By} \quad S_{Bz}) = \begin{pmatrix} S_{Ax}S_{Bx} & S_{Ax}S_{By} & S_{Ax}S_{Bz} \\ S_{Ay}S_{Bx} & S_{Ay}S_{By} & S_{Ay}S_{Bz} \\ S_{Az}S_{Bx} & S_{Az}S_{By} & S_{Az}S_{Bz} \end{pmatrix}, \quad (3.14)$$

and (2) the scalar tensor product,

$$\mathbf{O} : \mathbf{T} = \begin{pmatrix} O_{xx} & O_{xy} & O_{xz} \\ O_{yx} & O_{yy} & O_{yz} \\ O_{zx} & O_{zy} & O_{zz} \end{pmatrix} : \begin{pmatrix} T_{xx} & T_{xy} & T_{xz} \\ T_{yx} & T_{yy} & T_{yz} \\ T_{zx} & T_{zy} & T_{zz} \end{pmatrix} = \sum_{i,j} O_{ij} T_{ij}. \quad (3.15)$$

The scalar tensor product can be thought of as the dot product of vectorized matrices or the sum over the elements of a Hadamard product. It is sometimes referred to as the Frobenius inner product or double dot product. Like the interaction tensor, the dyadics can be written in terms of irreducible components, but, keeping in mind that the elements of $(\mathbf{S}_A \otimes \mathbf{S}_B^\top)$ are products of spin component operators, it is not helpful to do so in terms of Cartesian tensors. I will consider this further after introducing spherical tensor operators. In summary, the full spin-exciton hamiltonian is written as,

$$\mathcal{H} = \sum_k \mathbf{O}_{AB}^{(k)} : (\mathbf{S}_A \otimes \mathbf{S}_B^\top)^{(k)} + \mathbf{O}_{12}^{(k)} : (\mathbf{s}_1 \otimes \mathbf{s}_2^\top)^{(k)} + \mathbf{O}_{34}^{(k)} : (\mathbf{s}_3 \otimes \mathbf{s}_4^\top)^{(k)}. \quad (3.16)$$

Note that this Section considers the static representations of the physically dynamic interactions. Their “effective” values are experimentally observable on the time and energy scales relevant to triplet pair dynamics and magnetic spectroscopies; they are time,

ensemble, and spatial averages. In the following subsections, I show how the effective interaction parameters, like J , D , and E from Chapter 2, relate to elements of irreducible Cartesian tensors $\mathbf{O}^{(k)}$ by exploiting their physical symmetries. To arrive at a model spin hamiltonian, where scalar values parameterize the interactions, we integrate over the spatial part of the wavefunction.

3.2.3 Isotropic Inter-chromophore Exchange Interaction

The Coulomb interaction between excitons, here labeled 1 and 2, is a function that describes the energy from the spatial overlap of the electronic wavefunctions that are separated by a distance r_{12} . For example, to first order, it evaluates as the *scalar* inter-electron interaction potential given by the sum of Coulomb \mathcal{C} and Exchange \mathcal{K} integrals,⁵¹

$$\mathcal{C} = \left\langle \phi_i(1)\phi_j(2) \mid \frac{e^2}{r_{12}} \mid \phi_i(1)\phi_j(2) \right\rangle, \quad (3.17)$$

$$\mathcal{K} = \left\langle \phi_i(1)\phi_j(2) \mid \frac{e^2}{r_{12}} \mid \phi_i(2)\phi_j(1) \right\rangle, \quad (3.18)$$

$$\mathcal{J} = \mathcal{C} \pm \mathcal{K}, \quad (3.19)$$

where e is the elementary charge (1.6×10^{-19} C) and ϕ denotes the space part of the wavefunction for an electron in state i and another in state j . The angular brackets indicate that the values are averages over the orbital wavefunctions.⁵² Equation 3.17 says that the Coulomb integral adds a penalty for the repulsive forces between two charge densities. The Exchange integral (Eq. 3.18) is proportional to the orbital overlap and lowers \mathcal{J} (Eq. 3.19) for unpaired electrons relative to paired. By occupying antisymmetric spatial orbitals, the unpaired electrons in a triplet state avoid each other and minimize repulsive

magnetic forces. In contrast, the paired singlet electrons have an increased probability of occupying the same space and, it follows, higher energy. The exchange interaction is a purely quantum-mechanical effect.

We shift the energy to neglect the Coulomb integral and set the isotropic exchange parameter equal to the Exchange integral, $|J| = \mathcal{K}$, which can be measured experimentally as the energy splitting between spin states of different multiplicity (Figs. 2.2 and 5.2). Note that ferromagnetism is the physical alignment of electron spins, so for ferromagnetic systems $J < 0$ while for antiferromagnetic systems $J > 0$.

For the triplet pair, the intra-chromophore isotropic interactions are large (~ 1 eV). Because this is too large to be observable by magnetic field methods, this interaction is not included in the hamiltonian. The inter-chromophore isotropic interaction is also too large to be directly observed from the resonances in the X-band trEPR experiments herein, but it does manifest in the intensity of the spectrum. It is the largest energy scale in the hamiltonian and its value is given by the parameter J ,

$$\begin{aligned}\mathbf{O}_{12}^{(0)} &\equiv 0 \\ \mathbf{O}_{34}^{(0)} &\equiv 0 \\ \mathbf{O}_{AB}^{(0)} &= J.\end{aligned}\tag{3.20}$$

Because the scalar tensor product is defined for same-rank tensors, the rank-zero spin-spin operators form a scalar dot product $\mathbf{S}_A^\top \cdot \mathbf{S}_B$.

Based on the expression for the *JDE* model in Eq. 3.16, the inter-chromophore isotropic exchange hamiltonian is,

$$\begin{aligned} H_{AB}^{(0)} &= \mathbf{O}_{AB}^{(0)} : (\mathbf{S}_A \otimes \mathbf{S}_B^\top)^{(0)} \\ &= JS_A^\top \cdot \mathbf{S}_B. \end{aligned} \quad (3.21)$$

3.2.4 Anisotropic Intra-chromophore Interactions

The classical interaction between one spin-dipole and the magnetic field produced by another (Figs. 3.2a and 3.2b) transforms under rotation as a rank-two irreducible tensor so we use this interaction to derive the hamiltonian for rank-two spin-spin interactions. In the absence of a field, all M -sublevels of a spin state are degenerate. The rank-two anisotropic interactions are local magnetic fields that lift this degeneracy (Fig. 2.2) and are hence called zero-field splitting (ZFS) interactions.

To derive an expression for the spin-spin interaction, I start with the classical expression for the direct interaction between a dipole or magnetic moment, $\vec{\mu}_2$, and the magnetic field \vec{B}'_1 from another dipole, $\vec{\mu}_1$. (Note, throughout this dissertation the unprimed field vector \vec{B}_1 refers to the applied microwave field in an EPR experiment in magnetic field units.) The magnetic field from $\vec{\mu}_1$ is,

$$\begin{aligned} \vec{B}'_1 &= \frac{\mu_0}{4\pi r_{12}^3} (3(\vec{\mu}_1^\top \cdot \hat{r}_{12}) \hat{r}_{12} - \vec{\mu}_1) \\ &= \frac{\mu_0}{4\pi r_{12}^3} (3(\hat{r}_{12} \cdot \hat{r}_{12}^\top) \cdot \vec{\mu}_1 - \vec{\mu}_1), \end{aligned} \quad (3.22)$$

where μ_0 is the vacuum permeability and $\vec{r}_{12} = r \hat{r}_{12} = (x, y, z)$ is a vector pointing from the field source at $\vec{\mu}_1$ to the point of “measurement” at $\vec{\mu}_2$ (Fig. 3.2a). The energy of the

dipole $\vec{\mu}_2$ in the external field \vec{B}'_1 is,

$$\begin{aligned}
 -\vec{B}'_1 \cdot \vec{\mu}_2 &= -\frac{\mu_0}{4\pi r_{12}^3} (3\vec{\mu}_1^\top \cdot (\hat{r}_{12} \cdot \hat{r}_{12}^\top) - \vec{\mu}_1^\top) \cdot \vec{\mu}_2 \\
 &= -\frac{\mu_0}{4\pi r_{12}^3} (3(\vec{\mu}_1^\top \cdot \hat{r}_{12}) (\hat{r}_{12}^\top \cdot \vec{\mu}_2) - \vec{\mu}_1^\top \cdot \vec{\mu}_2) \\
 &= \frac{\mu_0}{4\pi r_{12}^3} (\vec{\mu}_1^\top \cdot \vec{\mu}_2 - 3(\vec{\mu}_1^\top \cdot \hat{r}_{12}) (\hat{r}_{12}^\top \cdot \vec{\mu}_2)) .
 \end{aligned} \tag{3.23}$$

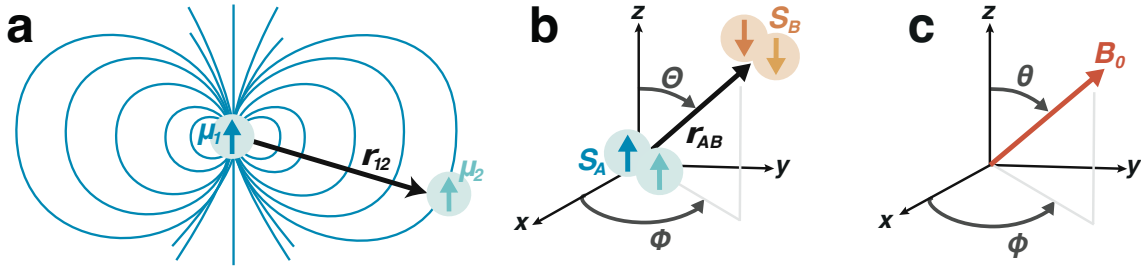


FIGURE 3.2: The *JDE* model is a function of orientation. **(a)** The intra-chromophore magnetic dipole-dipole rank-two hamiltonian is derived from the classical expression for the energy of a dipole $\vec{\mu}_2$ that is placed in the magnetic field produced by another $\vec{\mu}_1$. The vector \vec{r}_{12} describes the relative orientation of the two dipoles. **(b)** The inter-chromophore magnetic dipole-dipole interaction is parameterized by its magnitude, which is a function of the distance between the two triplets r_{AB} , and the relative orientation of the two chromophores with respect to the dimer frame (x, y, z , see Fig. 3.3b) that is described by the polar coordinates Θ and Φ . **(c)** The EPR spectrum is different for different orientations of the dimer in the Zeeman field \vec{B}_0 . A passive rotation (Section 3.3.2) of the dimer axes (x, y, z) by the polar angles θ and ϕ describes the system with respect to the field.

The dipole vectors are then promoted to spin operators by substituting the definition of the magnetic moment of an electron, $\vec{\mu} = -g\mu_B \mathbf{s}$, where $\mu_B = e\hbar/2m_e$ is the Bohr magneton and $g_e \approx 2.0023$ is the free electron g-factor. By assuming that the angular momentum of the system is entirely due to spin angular momentum, the g-factor is isotropic and $g_1 = g_2 = g_e$. For electron spin operators \mathbf{s}_1 and \mathbf{s}_2 (Fig. 2.1), the rank-two anisotropic

zero-field hamiltonian for chromophore A is,

$$\begin{aligned}
H_A^{(2)} &= \frac{\mu_B^2 g_e^2}{r_{12}^3} (\mathbf{s}_1^\top \cdot \mathbf{s}_2 - 3 (\mathbf{s}_1^\top \cdot \hat{r}_{12}) (\hat{r}_{12}^\top \cdot \mathbf{s}_2)) \\
&= \lambda (\mathbf{s}_1^\top \cdot \mathbf{s}_2 - 3 (\mathbf{s}_1^\top \cdot \hat{r}_{12}) (\hat{r}_{12}^\top \cdot \mathbf{s}_2)) \\
&= \lambda \mathbf{s}_1^\top \cdot (\mathbf{1} - 3 \hat{r}_{12} \cdot \hat{r}_{12}^\top) \cdot \mathbf{s}_2 \\
&= \lambda \mathbf{s}_1^\top \cdot \mathbf{D}_A \cdot \mathbf{s}_2,
\end{aligned} \tag{3.24}$$

where $\lambda \equiv \mu_B^2 g_e^2 / r_{12}^3$. In the last line the identity $(\mathbf{a}^\top \cdot \mathbf{b}) (\mathbf{c}^\top \cdot \mathbf{d}) = \mathbf{a}^\top \cdot (\mathbf{b} \cdot \mathbf{c}^\top) \cdot \mathbf{d}$ is used to define the matrix $\mathbf{D}_A \equiv \mathbf{1} - 3 (\hat{r}_{12} \cdot \hat{r}_{12}^\top)$.

Following Ref. [33], I now rewrite the single chromophore hamiltonians in terms of their total spin, $\mathbf{S}_A = \mathbf{s}_1 + \mathbf{s}_2$ and $\mathbf{S}_B = \mathbf{s}_3 + \mathbf{s}_4$, replace the direction \hat{r} with the vector \vec{r} , and omit the 12 subscript on r for readability,

$$\begin{aligned}
H_A^{(2)} &= \lambda \left(\mathbf{s}_1^\top \cdot \mathbf{s}_2 - \frac{3 (\mathbf{s}_1^\top \cdot \vec{r}) (\vec{r}^\top \cdot \mathbf{s}_2)}{r^2} \right) \\
&= \lambda \left(r^2 (\mathbf{s}_1^\top \cdot \mathbf{s}_2) - 3 (\mathbf{s}_1^\top \cdot \vec{r}) (\vec{r}^\top \cdot \mathbf{s}_2) \right).
\end{aligned} \tag{3.25}$$

Expanding the dot product,

$$\begin{aligned}
H_A^{(2)} &= \frac{\lambda}{r^2} [(r^2 - 3x^2)s_{1x}s_{2x} + (r^2 - 3y^2)s_{1y}s_{2y} + (r^2 - 3z^2)s_{1z}s_{2z} \\
&\quad - 3xy(s_{1x}s_{2y} + s_{2x}s_{1y}) - 3xz(s_{1x}s_{2z} + s_{2x}s_{1z}) - 3yz(s_{1y}s_{2z} + s_{2y}s_{1z})].
\end{aligned} \tag{3.26}$$

The spins here are electrons so, for example, $|s_{1x}^2| = 1/4$, and,

$$\begin{aligned} S_{Ax}^2 &= (s_{1x} + s_{2x})^2 = s_{1x}^2 + 2s_{1x}s_{2x} + s_{2x}^2 \\ s_{1x}s_{2x} &= \frac{1}{2}(S_{Ax}^2 - \frac{1}{2}) \end{aligned} \quad (3.27)$$

After substituting Eq. 3.27 into Eq. 3.26, and doing the same for similar expressions,

$$\begin{aligned} H_A^{(2)} &= \frac{\lambda}{2r^2} [(r^2 - 3x^2)S_{Ax}^2 + (r^2 - 3y^2)S_{Ay}^2 + (r^2 - 3z^2)S_{Az}^2 \\ &\quad - 6xy(s_{1x}s_{2y} + s_{2x}s_{1y}) - 6xz(s_{1x}s_{2z} + s_{2x}s_{1z}) - 6yz(s_{1y}s_{2z} + s_{2y}s_{1z})], \end{aligned} \quad (3.28)$$

where additional Cartesian terms are eliminated by using $r = \sqrt{x^2 + y^2 + z^2}$.

Finally, the following work is used to derive replacements for the three remaining single-electron terms,

$$\begin{aligned} S_{Ax}S_{Ay} &= (s_{1x} + s_{2x})(s_{1y} + s_{2y}) \\ &= s_{1x}s_{1y} + s_{1x}s_{2y} + s_{2x}s_{1y} + s_{2x}s_{2y}, \end{aligned} \quad (3.29a)$$

$$\begin{aligned} S_{Ay}S_{Ax} &= (s_{1y} + s_{2y})(s_{1x} + s_{2x}) \\ &= s_{1y}s_{1x} + s_{1y}s_{2x} + s_{2y}s_{1x} + s_{2y}s_{2x}, \end{aligned} \quad (3.29b)$$

$$\begin{aligned} S_{Ax}S_{Ay} + S_{Ay}S_{Ax} &= 2s_{1x}s_{2y} + 2s_{1y}s_{2x} \\ &\quad + \{s_{1x}s_{1y} + s_{1y}s_{1x}\} + \{s_{2x}s_{2y} + s_{2y}s_{2x}\}, \end{aligned} \quad (3.29c)$$

where the bracketed expressions are anticommutators and go to zero for electrons.⁵¹ The simplified expression is,

$$s_{1x}s_{2y} + s_{1y}s_{2x} = \frac{1}{2}(S_{Ax}S_{Ay} + S_{Ay}S_{Ax}). \quad (3.29d)$$

After substituting Eq. 3.29d and similar expressions into Eq. 3.28, the rank-two spin- A hamiltonian is,

$$\begin{aligned} H_A^{(2)} = & \frac{\lambda}{2r^2} [(r^2 - 3x^2)S_{Ax}^2 + (r^2 - 3y^2)S_{Ay}^2 + (r^2 - 3z^2)S_{Az}^2 \\ & - 3xy(S_{Ax}S_{Ay} + S_{Ay}S_{Ax}) - 3xz(S_{Ax}S_{Az} + S_{Az}S_{Ax}) - 3yz(S_{Ay}S_{Az} + S_{Az}S_{Ay})]. \end{aligned} \quad (3.30)$$

In matrix form this is,

$$\begin{aligned} H_A^{(2)} = & \frac{\lambda}{2} \mathbf{S}_A^\top \cdot \begin{bmatrix} \langle \frac{r^2 - 3x^2}{r^5} \rangle & \langle \frac{-3xy}{r^5} \rangle & \langle \frac{-3xz}{r^5} \rangle \\ \langle \frac{-3xy}{r^5} \rangle & \langle \frac{r^2 - 3y^2}{r^5} \rangle & \langle \frac{-3yz}{r^5} \rangle \\ \langle \frac{-3xz}{r^5} \rangle & \langle \frac{-3yz}{r^5} \rangle & \langle \frac{r^2 - 3z^2}{r^5} \rangle \end{bmatrix} \cdot \mathbf{S}_A \\ = & \frac{\lambda}{2} \mathbf{S}_A^\top \cdot \mathbf{D}_A \cdot \mathbf{S}_A, \end{aligned} \quad (3.31)$$

where angular brackets denote integrals over spatial coordinates. Note that the 3×3 matrix representation of \mathbf{D}_A in Eq. 3.31 is traceless and symmetric—it is irreducible—so that only five independent parameters are required to represent it in any given reference frame.

It is conventional to specify \mathbf{D} relative to its “principal frame.” The principal frame of an interaction is the coordinate system in which the interaction lies solely along the axes; the principal frame of an interaction matrix, in this sense, is analogous to the eigenspace

of a hamiltonian. I assume that the principal frame of the intra-chromophore interaction lies along the chromophore axes as illustrated in Fig. 3.3a. In Chapter 4, I extract an angle β that describes the relative orientation of the principal frames of \mathbf{D}_A and \mathbf{D}_B for the dimer TIPS-BP1' by fitting its EPR spectrum and it is identical to the value calculated for the dimer by DFT methods, demonstrating that this is a good approximation for the systems of interest.

In its principal frame the \mathbf{D} matrix is diagonal,

$$\mathbf{D} = \begin{bmatrix} D_{xx} & 0 & 0 \\ 0 & D_{yy} & 0 \\ 0 & 0 & D_{zz} \end{bmatrix}, \quad (3.32)$$

where convention requires that $|D_{zz}| > |D_{xx}| \geq |D_{yy}|$. Because \mathbf{D} is traceless, the ZFS interaction is typically reported in terms of two parameters, the axial component $D = 3D_{zz}/2$ and the rhombic component $E = (D_{xx} - D_{yy})/2$, so that in its principal frame,

$$\mathbf{D} = \begin{bmatrix} -\frac{D}{3} + E & 0 & 0 \\ 0 & -\frac{D}{3} - E & 0 \\ 0 & 0 & \frac{2}{3}D \end{bmatrix}, \quad (3.33)$$

and

$$H_A^{(2)} = D_A/3 \left(3S_{Az}^2 - \mathbf{S}_A^2 \right) + E_A \left(S_{Ax}^2 - S_{Ay}^2 \right), \quad (3.34)$$

where $|D| \geq 3|E|$. The hamiltonian for chromophore B has the same form as the hamiltonian for chromophore A and can be written by swapping out the spin labels. Note that

the values for \mathbf{D}_A and \mathbf{D}_B are only equivalent if the chromophores are spatially and chemically equivalent (see Section 3.3.2). I refer to the chromophores in these dimers, where $D_A = D_B$, as being “parallel” and this special case is the basis of the theory in Chapter 2.

According to Eq. 3.31, the intra-chromophore anisotropic interactions are rank-two irreducible tensors defined as,

$$\begin{aligned}\mathbf{O}_A^{(2)} &= \mathbf{D}_A \\ \mathbf{O}_B^{(2)} &= \mathbf{D}_B.\end{aligned}\tag{3.35}$$

The ZFS hamiltonians in the form of Eq. 3.16 are,

$$\begin{aligned}H_A^{(2)} &= \mathbf{D}_A^{(2)} : (\mathbf{S}_A \otimes \mathbf{S}_A^\top)^{(2)} \\ H_B^{(2)} &= \mathbf{D}_B^{(2)} : (\mathbf{S}_B \otimes \mathbf{S}_B^\top)^{(2)}.\end{aligned}\tag{3.36}$$

3.2.5 Anisotropic Inter-chromophore Interaction

Similar to the intra-chromophore interactions \mathbf{D} but for two spin-1 centers, the anisotropic inter-chromophore interaction is also derived from the classical dipole-dipole expression (Eq. 3.24). After promoting operators to their quantum mechanical analogs and integrating over spatial wavefunctions, we arrive at the expression for the rank-two anisotropic inter-chromophore hamiltonian,³⁸

$$H_{AB}^{(2)} = \mathbf{S}_A^\top \cdot \mathbf{X} (\mathbf{1} - 3\hat{\mathbf{r}}_{AB} \cdot \hat{\mathbf{r}}_{AB}^\top) \cdot \mathbf{S}_B = \mathbf{S}_A^\top \cdot \mathbf{X} \cdot \mathbf{S}_B.\tag{3.37}$$

Here, \mathbf{S}_A and \mathbf{S}_B denote the single chromophore spin operators that sum to the total spin $\mathbf{S} = \mathbf{S}_A + \mathbf{S}_B$. \mathbf{X} describes the magnitude of the interaction which goes as $g^2 \mu_B^2 / r_{AB}^3$, where r_{AB} is the magnitude of the vector $\vec{r}_{AB} = r \hat{\mathbf{r}}_{AB}$ that points from spin center A to B (Fig. 3.2),

$\hat{r}_{AB} = (\sin \Theta \cos \Phi, \sin \Theta \sin \Phi, \cos \Theta)$, where Θ and Φ are the polar and azimuthal angles that define the orientation of \hat{r}_{AB} in the chosen coordinate system. I choose to define the anisotropic inter-chromophore interaction tensor in the “dimer axis system” given by the vector sum of the single-chromophore magnetic axes (Fig. 3.3b).

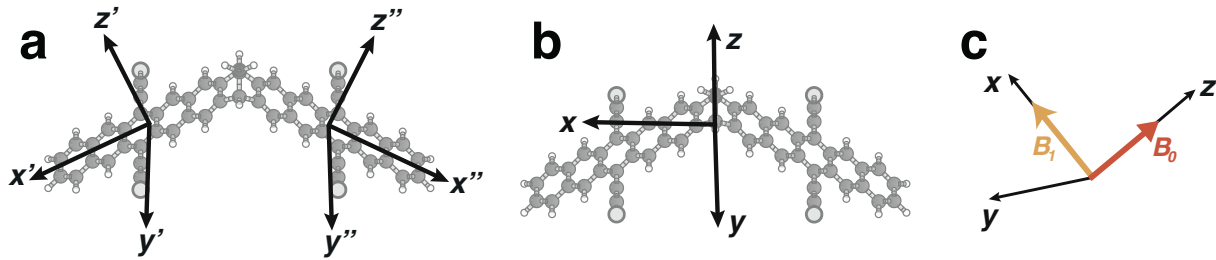


FIGURE 3.3: The *JDE* model is defined with respect to a chosen frame of reference. When giving values for the various anisotropic interactions, it is necessary to specify which reference frame the values are defined in. (a) For the *JDE* model, the anisotropic intra-chromophore interactions are defined in their respective single-chromophore axes systems. (b) I choose to express the anisotropic inter-chromophore interaction with respect to the dimer axis system—the vector sum of the single-chromophore frames. (c) Before evaluating the hamiltonian, all interactions are rotated into the lab frame, where the z -axis is defined by the static Zeeman field \vec{B}_0 that is perpendicular to the microwave field \vec{B}_1 along the x -axis.

In the dimer frame,

$$\mathbf{X} = X \begin{pmatrix} 1 - 3 \sin^2 \Theta \cos^2 \Phi & -3 \sin^2 \Theta \sin \Phi \cos \Phi & -3 \sin \Theta \cos \Theta \cos \Phi \\ -3 \sin^2 \Theta \sin \Phi \cos \Phi & 1 - 3 \sin^2 \Theta \sin^2 \Phi & -3 \sin \Theta \cos \Theta \sin \Phi \\ -3 \sin \Theta \cos \Theta \cos \Phi & -3 \sin \Theta \cos \Theta \sin \Phi & 1 - 3 \cos^2 \Theta \end{pmatrix}. \quad (3.38)$$

Notice that these matrix elements are the spherical equivalents of the matrix elements in Eq. 3.31.

Note that dimers whose chromophores vary translationally have different orientations and magnitudes of \vec{r}_{AB} and, therefore, have different values of X , Θ , and Φ —even if the

chromophores have parallel sets of molecular axes. In Chapter 4, I calculate the EPR spectrum for a dimer whose relative orientation is fixed and, by comparing the calculated spectrum to the data, extract a single value of X from the data. In crystals with many unique pair sites, like the single crystal of TES TIPS-TT dimers in Chapter 5, the EPR spectrum is a function of a wide distribution of X values.

The inter-chromophore anisotropic rank-two dipole-dipole interaction and hamiltonian are,

$$\begin{aligned}\mathbf{X}_{AB}^{(2)} &= \mathbf{X} \\ H_{AB}^{(2)} &= \mathbf{X}_{AB}^{(2)} : (\mathbf{S}_A \otimes \mathbf{S}_B^\top)^{(2)}.\end{aligned}\tag{3.39}$$

3.2.6 Rank-1 Interactions

Interactions with rank-1 antisymmetric representations cant the spins. They are relativistic and generally negligible for singlet fission materials.⁸ In general, they are neglected throughout this dissertation because it is primarily concerning the spin dynamics at strong fields, away from level crossings. Although, in Chapter 5, I model the delayed fluorescence following singlet fission (Fig. 1.2) as a function of a much stronger field (up to 14 T) than the field in X-band EPR experiments (350 mT). In these magnetophotoluminescence experiments, phenomena occur in the spectrum at Zeeman field values where states with different multiplicities cross, for example, where the ^1TT and $^3\text{TT}_{\pm 1}$ levels become degenerate. Near degeneracies the level splitting is on the order of the weak interactions so that the otherwise negligible rank-1 interactions become important. Because of their relevance near degeneracies, I derive selection rules from the most general expression of a rank-1 spin-spin hamiltonian using symmetry arguments alone.

The rank $k = 1$ spin-spin hamiltonian for spins u and v is written as³⁸

$$H_{uv} = \vec{d}_{uv} \cdot (\mathbf{s}_u \times \mathbf{s}_v), \quad (3.40)$$

where \times denotes the vector cross-product. According to Eq. 3.11 the interaction vector \vec{d}_{ij} also has a matrix form that is a rank-1 irreducible tensor. For consistency I express the interaction according to this,

$$\begin{aligned} \mathbf{d}_{AB}^{(1)} &= \mathbf{d}_{AB} \\ \mathbf{d}_A^{(1)} &= \mathbf{d}_A \\ \mathbf{d}_B^{(1)} &= \mathbf{d}_B. \end{aligned} \quad (3.41)$$

The corresponding hamiltonians are,

$$\begin{aligned} H_{AB}^{(1)} &= \mathbf{d}_{AB}^{(1)} : (\mathbf{S}_A \otimes \mathbf{S}_B^\top)^{(1)} \\ H_A^{(1)} &= \mathbf{d}_{12}^{(1)} : (\mathbf{s}_1 \otimes \mathbf{s}_2^\top)^{(1)} \\ H_B^{(1)} &= \mathbf{d}_{34}^{(1)} : (\mathbf{s}_3 \otimes \mathbf{s}_4^\top)^{(1)}. \end{aligned} \quad (3.42)$$

Note that unlike the intra-chromophore rank-two hamiltonians, the rank-one hamiltonians are a function of the single-electron spin operators.

3.2.7 Coupled Spin States

The total spin operator \mathbf{S} is a sum of the triplet spin operators \mathbf{S}_A and \mathbf{S}_B . I label the operators A and B to denote which of the two vector spaces they operate on. For example, \mathbf{S}_A acts on vector space \mathbb{V}_A that belongs to chromophore A and \mathbf{S}_B acts on vector space \mathbb{V}_B . The total spin operates on the vector product space $\mathbb{V} = \mathbb{V}_A \otimes \mathbb{V}_B$ so that

$\mathbf{S} = \mathbf{S}_A \otimes \mathbf{1}_B + \mathbf{1}_A \otimes \mathbf{S}_B$, where $\mathbf{1}$ is the identity operator in the vector space of spin A or B . The vector spaces \mathbb{V}_A and \mathbb{V}_B are spanned by the “uncoupled” states $|S_A M_A\rangle$ and $|S_B M_B\rangle$, respectively. The biexciton space is spanned by the tensor products states,

$$|S_A M_A\rangle \otimes |S_B M_B\rangle = |S_A M_A; S_B M_B\rangle, \quad (3.43)$$

where

$$\begin{aligned} S_{Az}|S_A M_A; S_B M_B\rangle &= M_A |S_A M_A; S_B M_B\rangle \\ S_{Bz}|S_A M_A; S_B M_B\rangle &= M_B |S_A M_A; S_B M_B\rangle. \end{aligned} \quad (3.44)$$

For the triplet pair $S_A = S_B = 1$, so throughout the text the notation for the uncoupled product states is often simplified to $|M_A M_B\rangle$. The uncoupled biexciton basis is $\{|M_A M_B\rangle\} = \{|-\rangle, |-0\rangle, |-\rangle, |0-\rangle, |00\rangle, |0+\rangle, |+-\rangle, |+0\rangle, |++\rangle\}$.

Based on the principles of quantum superposition, solutions to the hamiltonian (its eigenvalues) are conserved in any basis of the form $\{\sum_{M_A, M_B} c_{M_A M_B} |M_A M_B\rangle\}$, where $c_{M_A M_B}$ are arbitrary complex coefficients. One choice for the coefficients comes from the unitary transformation that maps the uncoupled product states $|S_A M_A; S_B M_B\rangle$ to a coupled representation—a $(2S_A + 1)(2S_B + 1)$ -dimensional space spanned by the basis set $\{|S_A S_B; SM\rangle\}$, where S is the eigenvalue of the total spin operator and M is the eigenvalue of the z -component of the total spin operator S_z . This unitary transformation is,

$$\begin{aligned} &|S_A M_A; S_B M_B\rangle \langle S_A S_B; SM| \\ &= \sum_{M_A, M_B} |S_A M_A; S_B M_B\rangle \langle S_A M_A; S_B M_B| S_A S_B; SM \rangle \langle S_A S_B; SM|. \end{aligned} \quad (3.45)$$

Its matrix elements $\langle S_A M_A; S_B M_B | S_A S_B; SM \rangle$ are integrals over the angular momentum

functions given analytically by the spherical harmonics—they are Clebsch-Gordan coefficients. For the triplet pair the transformation matrix is,

$$\begin{array}{c|cccccccccc}
 & \langle 0,0 | & \langle 1,-1 | & \langle 1,0 | & \langle 1,+1 | & \langle 2,-2 | & \langle 2,-1 | & \langle 2,0 | & \langle 2,+1 | & \langle 2,+2 |
 \end{array}
 \\
 \begin{array}{l}
 |--\rangle \\
 |-0\rangle \\
 |+-\rangle \\
 |0-\rangle \\
 |00\rangle \\
 |0+\rangle \\
 |+-\rangle \\
 |+0\rangle \\
 |++\rangle
 \end{array}
 \left(\begin{array}{cccccccccc}
 0 & 0 & 0 & 0 & 1 & 0 & 0 & 0 & 0 & 0 \\
 0 & -\frac{1}{\sqrt{2}} & 0 & 0 & 0 & \frac{1}{\sqrt{2}} & 0 & 0 & 0 & 0 \\
 \frac{1}{\sqrt{3}} & 0 & -\frac{1}{\sqrt{2}} & 0 & 0 & 0 & \frac{1}{\sqrt{6}} & 0 & 0 & 0 \\
 0 & \frac{1}{\sqrt{2}} & 0 & 0 & 0 & \frac{1}{\sqrt{2}} & 0 & 0 & 0 & 0 \\
 -\frac{1}{\sqrt{3}} & 0 & 0 & 0 & 0 & 0 & \sqrt{\frac{2}{3}} & 0 & 0 & 0 \\
 0 & 0 & 0 & -\frac{1}{\sqrt{2}} & 0 & 0 & 0 & \frac{1}{\sqrt{2}} & 0 & 0 \\
 \frac{1}{\sqrt{3}} & 0 & \frac{1}{\sqrt{2}} & 0 & 0 & 0 & \frac{1}{\sqrt{6}} & 0 & 0 & 0 \\
 0 & 0 & 0 & \frac{1}{\sqrt{2}} & 0 & 0 & 0 & \frac{1}{\sqrt{2}} & 0 & 0 \\
 0 & 0 & 0 & 0 & 0 & 0 & 0 & 0 & 0 & 1
 \end{array} \right). \quad (3.46)$$

The coupled state representation, or basis, splits up into three invariant and irreducible subspaces, each characterized by its total spin $|S_A - S_B| \leq S \leq S_A + S_B$ and

with dimensions $2S + 1$,

$$\begin{aligned}
 |^1\text{TT}_0\rangle &= \frac{1}{\sqrt{3}} (|-\rangle - |0\rangle + |+\rangle) \\
 |^3\text{TT}_{-1}\rangle &= \frac{1}{\sqrt{2}} (-|-\rangle + |0-\rangle) \\
 |^3\text{TT}_0\rangle &= \frac{1}{\sqrt{2}} (-|-\rangle + |+\rangle) \\
 |^3\text{TT}_{+1}\rangle &= \frac{1}{\sqrt{2}} (-|0+\rangle + |+0\rangle) \\
 |^5\text{TT}_{-2}\rangle &= |--\rangle \\
 |^5\text{TT}_{-1}\rangle &= \frac{1}{\sqrt{2}} (|-\rangle + |0-\rangle) \\
 |^5\text{TT}_0\rangle &= \frac{1}{\sqrt{6}} (|-\rangle + 2|00\rangle + |+-\rangle) \\
 |^5\text{TT}_{+1}\rangle &= \frac{1}{\sqrt{2}} (|0+\rangle + |+0\rangle) \\
 |^5\text{TT}_{+2}\rangle &= |++\rangle.
 \end{aligned} \tag{3.47}$$

The same-spin subspaces are irreducible because the total spin of the state does not change under rotation—only M changes when S_x , S_y , or S_z are applied to the total spin states. The notations $|^{2S+1}\text{TT}_M\rangle$ and $|S, M\rangle$ are used interchangeably throughout this text to denote the total spin states. As before, because $S_A = S_B = 1$, notation is often simplified from $|S_A S_B; SM\rangle$ to $|S, M\rangle$.

Note that the coupled states are simultaneous eigenkets of \mathbf{S}^2 , \mathbf{S}_A^2 , \mathbf{S}_B^2 , and S_z ,

$$\begin{aligned}\mathbf{S}^2|S, M\rangle &= S(S+1)|S, M\rangle \\ \mathbf{S}_A^2|S, M\rangle &= S_A(S_A+1)|S, M\rangle \\ \mathbf{S}_B^2|S, M\rangle &= S_B(S_B+1)|S, M\rangle \\ S_z|S, M\rangle &= M|S, M\rangle.\end{aligned}\tag{3.48}$$

In the coupled basis, \mathbf{S}_A^2 , \mathbf{S}_B^2 , and S_z commute with \mathbf{S}^2 , however, the triplet spin components, for example, S_{Az} and S_{Bz} , do not commute with \mathbf{S}^2 .

It is clear that similarities exist between the irreducible Cartesian tensors and the spin states and spin operators. For example, the multiplicity of a spin S state is $2S+1$. The spin is analogous to the rank of an irreducible tensor which has $2k+1$ parts, or components. It turns out that irreducible Cartesian tensors belong to a special group of tensors called spherical tensors, which transform like the angular momenta and are the basis of the Wigner-Eckart theorem.

3.2.8 Selection Rules from Discrete Symmetries

To conclude this Section, I consider the selection rules that arise from discrete symmetry operators. Recall that the intra-chromophore hamiltonian is (Eq. 3.6),

$$H_A + H_B = \mathbf{s}_1^\top \cdot \mathbf{O}_{12} \cdot \mathbf{s}_2 + \mathbf{s}_3^\top \cdot \mathbf{O}_{34} \cdot \mathbf{s}_4,\tag{3.49}$$

where \mathbf{s}_i for $i = 1 - 4$ are the electron spin operators for the HOMO and LUMO levels in a frontier molecular orbital description of the chromophores comprising the triplet pair,

labelled A and B (Fig. 2.1). For convenience, I begin by making simplifications similar to those introduced in Section 3.2.1. Recall that the hamiltonian may instead be written as the scalar product of two matrices (Eq. 3.15),

$$H_A + H_B = \mathbf{O}_{12} : (\mathbf{s}_1 \otimes \mathbf{s}_2^\top) + \mathbf{O}_{34} : (\mathbf{s}_3 \otimes \mathbf{s}_4^\top). \quad (3.50)$$

To again simplify notation, I now define new operators for the spin tensor products, $(\mathbf{s}_1 \otimes \mathbf{s}_2^\top) \equiv \mathbf{T}_A$ and $(\mathbf{s}_3 \otimes \mathbf{s}_4^\top) \equiv \mathbf{T}_B$, not to be confused with the spin-1 operators \mathbf{S}_A and \mathbf{S}_B , and relabel the irreducible spin interaction matrices as $\mathbf{O}_{12} \equiv \mathbf{O}_A$ and $\mathbf{O}_{34} \equiv \mathbf{O}_B$ so that,

$$H_A + H_B = \mathbf{O}_A : \mathbf{T}_A + \mathbf{O}_B : \mathbf{T}_B. \quad (3.51)$$

The first symmetry considered is the particle exchange, or permutation, symmetry. The particle exchange operator \mathbf{P}_{AB} swaps out the labels that correspond to the subspaces of the two-triplet system, A and B . For the total spin coupled triplet pair states (Eq. 3.47), it is easily seen upon inspection and well understood that the singlet and quintet spin states are even under exchange of A and B , while the triplet states are odd. For example,

$$\begin{aligned} \mathbf{P}_{AB}|^1\text{TT}_0\rangle &= \frac{1}{\sqrt{3}} (\mathbf{P}_{AB}|-\rangle - \mathbf{P}_{AB}|00\rangle + \mathbf{P}_{AB}|+\rangle) \\ &= \frac{1}{\sqrt{3}} (|-\rangle - |00\rangle + |+\rangle) \\ &= |^1\text{TT}_0\rangle. \end{aligned} \quad (3.52)$$

In summary,

$$\begin{aligned}\mathbf{P}_{AB}|^1\text{TT}\rangle &= |^1\text{TT}\rangle \\ \mathbf{P}_{AB}|^3\text{TT}\rangle &= -|^3\text{TT}\rangle \\ \mathbf{P}_{AB}|^5\text{TT}\rangle &= |^5\text{TT}\rangle.\end{aligned}\tag{3.53}$$

The coupled Zeeman states are eigenstates of the exchange operator and their eigenvalues are a function of the total spin,

$$\mathbf{P}_{AB}|^{2S+1}\text{TT}\rangle = (-1)^S |^{2S+1}\text{TT}\rangle.\tag{3.54}$$

Likewise, the spin operators transform under particle exchange as,

$$\mathbf{P}_{AB}\mathbf{T}_A\mathbf{P}_{AB}^{-1} = \mathbf{T}_B.\tag{3.55}$$

The interactions tensors are invariant under the particle exchange operator,

$$\mathbf{P}_{AB}\mathbf{O}\mathbf{P}_{AB}^{-1} = \mathbf{O}.\tag{3.56}$$

I finally define two new spin operators that are the sum and difference of the new single-chromophore spin operators: $(\mathbf{T}_A + \mathbf{T}_B)/2 \equiv \boldsymbol{\Sigma}$ and $(\mathbf{T}_A - \mathbf{T}_B)/2 \equiv \boldsymbol{\Delta}$, respectively. The hamiltonian conveniently factorizes as,

$$H_A + H_B = H_{\Sigma} + H_{\Delta} = (\mathbf{O}_A + \mathbf{O}_B) : \boldsymbol{\Sigma} + (\mathbf{O}_A - \mathbf{O}_B) : \boldsymbol{\Delta}.\tag{3.57}$$

The exchange symmetry of the new spin operators are,

$$\begin{aligned}\mathbf{P}_{AB}\boldsymbol{\Sigma}\mathbf{P}_{AB}^{-1} &= \boldsymbol{\Sigma} \\ \mathbf{P}_{AB}\boldsymbol{\Delta}\mathbf{P}_{AB}^{-1} &= -\boldsymbol{\Delta}.\end{aligned}\tag{3.58}$$

The interaction tensors for dimers of molecularly equivalent chromophores are related by a rotation, $\mathbf{O}_B = \mathbf{R}^{-1}\mathbf{O}_A\mathbf{R}$. For parallel chromophores, $\mathbf{R} = \mathbf{1}$ and H_Δ is zero. The exchange symmetry selection rules for parallel chromophores with respect to the coupled spin states $|S, M\rangle$ and $|S', M'\rangle$ are found by inserting $\mathbf{P}_{AB}^{-1}\mathbf{P}_{AB} = \mathbf{1}$ into the matrix element for H_Σ (Eq. 3.57),

$$\begin{aligned}\langle S', M' | H_\Sigma | S, M \rangle &= \langle S', M' | \mathbf{P}_{AB}^{-1} \mathbf{P}_{AB} H_\Sigma \mathbf{P}_{AB}^{-1} \mathbf{P}_{AB} | S, M \rangle \\ &= \langle S', M' | \mathbf{P}_{AB}^{-1} \left[\mathbf{P}_{AB} [(\mathbf{O}_A + \mathbf{O}_B) : \boldsymbol{\Sigma}] \mathbf{P}_{AB}^{-1} \right] \mathbf{P}_{AB} | S, M \rangle \\ &= \langle S', M' | \mathbf{P}_{AB}^{-1} [(\mathbf{O}_A + \mathbf{O}_B) : \boldsymbol{\Sigma}] \mathbf{P}_{AB} | S, M \rangle \\ &= \left[\langle S', M' | \mathbf{P}_{AB}^{-1} \right] H_\Sigma \left[\mathbf{P}_{AB} | S, M \rangle \right] \\ &= (-1)^{S'} \langle S', M' | H_\Sigma | S, M \rangle (-1)^S \\ &= (-1)^{S'+S} \langle S', M' | H_\Sigma | S, M \rangle.\end{aligned}\tag{3.59}$$

It follows that matrix elements of H_Σ , which is the full hamiltonian for parallel chromophores, are zero unless $S + S' = \text{even}$. In other words, the ${}^3\text{TT}$ manifold is isolated in parallel systems.

For non-parallel chromophores, the exchange symmetry of H_Δ must also be considered. Using the same arguments as above,

$$\langle S', M' | H_\Delta | S, M \rangle = (-1)^{S'+S+1} \langle S', M' | H_\Delta | S, M \rangle, \quad (3.60)$$

where the exponent of 1 is from the eigenvalue of Δ . The matrix elements of H_Δ are zero unless $S + S' = \text{odd}$. Upon breaking parallel symmetry, transitions to the ${}^3\text{TT}$ state become allowed. But the coupling between $\Delta S = \pm 1$ states goes as the difference in the interaction tensors, $(\mathbf{O}_A - \mathbf{O}_B) / 2$, and is therefore expected to be significantly weaker. Further, for same-molecule chromophores, the Δ coupling diminishes as the molecules align, $(\mathbf{O}_A - \mathbf{R}^{-1}\mathbf{O}_A\mathbf{R}) / 2$.

$H_A + H_B$	S	S'
H_Σ	0	0, 2
	1	1
	2	0, 2
H_Δ	0	1
	1	0, 2
	2	1

TABLE 3.1: Exchange symmetry selection rules. The exchange operator \mathbf{P}_{AB} exchanges the spin labels of operators and spin states. Exchange symmetry requires that the intra-chromophore hamiltonian matrix elements in the total spin basis $\langle S'M' | H_A + H_B | S, M \rangle$ are non-zero for the specified conditions. For parallel chromophores, $H_\Delta = (\mathbf{O}_A - \mathbf{O}_B) : \Delta$ is zero so that the selection rules for the intra-chromophore hamiltonian are given solely by $H_\Sigma = (\mathbf{O}_A + \mathbf{O}_B) : \Sigma$ (Eq. 3.57).

Now consider the spatial inversion symmetry of the spin system, another discrete symmetry. The parity operator π sends the spatial coordinates (x, y, z) to their inverse position $(-x, -y, -z)$. For example, the function $x_1 + x_2$ is symmetric under exchange, but odd under parity, while $x_1^2 + x_2^2$ is symmetric with respect to both exchange and parity.

Under the action of π the spin operator \mathbf{S} , a generator of rotations, is unchanged,

$$\pi \mathbf{S} \pi^{-1} = \mathbf{S}. \quad (3.61)$$

Using the fact that $\pi^2 = \mathbf{1}$, the parity operator similarly only has two eigenvalues, ± 1 , and like before the observed value only depends on S . The choice however for assigning these to the different total spin states is arbitrary in non-relativistic quantum mechanics, so I assign them as,

$$\pi |^{2S+1}\text{TT}\rangle = (-1)^S |^{2S+1}\text{TT}\rangle. \quad (3.62)$$

Finally, according to the matrices for the irreducible rank- k tensors (Eqs. 3.10-3.12), the interaction tensors transform under parity according to their rank,

$$\pi \mathbf{O}^{(k)} \pi^{-1} = (-1)^k \mathbf{O}^{(k)}. \quad (3.63)$$

This states that if an interaction represented by \mathbf{O}_A , \mathbf{O}_B , or \mathbf{O}_{AB} is inversion symmetric, its rank-one components are zero—rank-one interactions are, by definition, antisymmetric.

The parity operator applies the following selection rule to H_A , H_B , and H_{AB} ,

$$\begin{aligned}
 \langle S', M' | H | S, M \rangle &= \langle S', M' | \pi^{-1} \pi H \pi^{-1} \pi | S, M \rangle \\
 &= \langle S', M' | \pi^{-1} \left[\pi \left(\mathbf{O}^{(k)} : \mathbf{T} \right) \pi^{-1} \right] \pi | S, M \rangle \\
 &= \langle S', M' | \pi^{-1} (-1)^k \left(\mathbf{O}^{(k)} : \mathbf{T} \right) \pi | S, M \rangle \\
 &= (-1)^k \left[\langle S', M' | \pi^{-1} \right] H \left[\pi | S, M \rangle \right] \\
 &= (-1)^k (-1)^{S'} \langle S', M' | H | S, M \rangle (-1)^S \\
 &= (-1)^{S'+S+k} \langle S', M' | H | S, M \rangle,
 \end{aligned} \tag{3.64}$$

where I have dropped subscripts for generality and \mathbf{T} is defined as the relevant spin tensor product (Eq. 3.51). This says that $k = \text{even}$ interactions only connect $\Delta S = \text{even}$ states and that $k = \text{odd}$ interactions only connect $\Delta S = \text{odd}$ states.

This symmetry applies to H_A , H_B , and H_{AB} , separately. If the principal axes of \mathbf{D}_A are parallel to those of \mathbf{D}_B (Section 3.3.2), and if the interactions are equivalent, $\mathbf{D}_A = \mathbf{D}_B$, then the inter-chromophore hamiltonian factorizes so that this inversion symmetry selection rule applies to the sum $H_A + H_B$. For this parallel case, a similar selection rule independent of k was already shown in Table 3.1 (H_Δ).

H_{AB}	S	S'
$k = 0, 2$	0	0, 2
	1	1
	2	0, 2
$k = 1$	0	1
	1	0, 2
	2	1

TABLE 3.2: The inversion symmetry selection rules from the parity operator π depend on the rank k of the interaction tensor. The inter-chromophore hamiltonian matrix elements in the total spin basis $\langle S'M'|H_{AB}|S, M\rangle$ are non-zero for the specified conditions.

3.3 The Wigner-Eckart Theorem

Conservation of angular momentum is of fundamental importance to the quantum mechanics of many-particle systems. Conservation laws are deeply rooted in the superposition principles and symmetries of physical systems under various changes. Selection rules realize the interplay between the symmetries of the spin states and the hamiltonian that represent the system. When acted upon, for example, by rotation, exchange, and inversion operators, the symmetries of the hamiltonian are unveiled by its transformation.

The Wigner-Eckart theorem is a powerful tool for evaluating the spin hamiltonian matrix elements, and selection rules from rotational symmetries are a direct result of its application. As I showed in Chapter 2, the relevant states for singlet fission chromophores in the strong J limit are the coupled Zeeman states. But in Cartesian space, it is sometimes impossible to analytically evaluate matrix elements in the total spin basis. Being deeply rooted in the coupling of angular momenta, the Wigner-Eckart theorem overcomes this obstacle.

This Section begins with a detailed account of the underlying concepts of the Wigner-Eckart theorem, focusing on spherical tensors and rotations. Then, matrix elements for the triplet pair spin hamiltonian (Eq. 3.16) are derived according to the Wigner-Eckart theorem, revealing selection rules for transitions between the total spins states.

3.3.1 Spherical Tensor Formalism

Spherical tensors $\mathbf{T}^{(k)}$ are a subset of tensors that transform under rotations of the coordinate frame like the components of the spherical harmonic functions \mathcal{Y}_l^m .⁵¹ As in Section 3.2.1, k denotes the rank of the tensor, which is analogous to the spherical harmonic order, l , and q denotes the component, like the index m . In Eq. 3.9, the reducible Cartesian tensor \mathbf{O} was expanded in terms of irreducible spherical tensors. The irreducible spherical tensor operator $\mathbf{T}^{(k)}$ is a set (denoted by the parenthetical (k) superscript) of $2k + 1$ operators \mathbf{T}_q^k , where $q = -k, -k + 1, \dots, k - 1, k$. A spherical tensor operator is defined by how it transforms under rotation. The finite rotation operator $\mathcal{D}^{(k)}(\Omega)$ rotates a spherical tensor component, or its frame of reference, and the result is a superposition of same-rank tensor components, weighted by rotational coefficients. The rank of an irreducible tensor is conserved under rotation,

$$\mathcal{D}(\Omega)\mathbf{T}_q^k\mathcal{D}^\dagger(\Omega) = \sum_{q'=-k}^k \mathcal{D}_{q'q}^k(\Omega)\mathbf{T}_{q'}^k, \quad (3.65)$$

or, similarly,

$$\mathcal{D}^\dagger(\Omega)\mathbf{T}_q^k\mathcal{D}(\Omega) = \sum_{q'=-k}^k \mathcal{D}_{qq'}^{k*}(\Omega)\mathbf{T}_{q'}^k. \quad (3.66)$$

The scalar coefficients $\mathcal{D}_{q'q}^k(\Omega)$ are *Wigner rotation matrix elements* of the finite rotation operator, $\langle kq|\mathcal{D}^{(k)}(\Omega)|kq'\rangle$.⁵³ The first line rotates the q -th component of the rank- k tensor T_k^q , while the second line gives the q -th component of a rotated tensor. This says that the action of rotating a spherical tensor is equivalent to angular momentum addition and thus, being deeply rooted in the coupling of angular momenta, allows us to derive the selection rules with respect to the total spin of the triplet pair even when the operators evaluated belong to subspaces of the total spin.

The finite rotation operators are built from a series of infinitesimal rotations, $\mathcal{D}(\Omega) = e^{i\alpha S_z} e^{i\beta S_y} e^{i\gamma S_z}$, where $\Omega \equiv \{\alpha, \beta, \gamma\}$ is a set of Euler angles (Section 3.3.2). Let $d_{q'q}^k \equiv \langle kq'|e^{i\beta S_y}|kq\rangle$, then,

$$\begin{aligned}\mathcal{D}_{q'q}^k &= e^{i\gamma q'} e^{i\alpha q} \langle kq'|e^{i\beta S_y}|kq\rangle \\ &= e^{i\gamma q'} e^{i\alpha q} d_{q'q}^k(\beta).\end{aligned}\quad (3.67)$$

The $d_{q'q}^k(\beta)$ are the matrix elements of Wigner's small d-matrix. They have a closed formula in terms of Jacobi polynomials, P ,

$$d_{q'q}^k(\beta) = \left[\frac{(k+q')!(k-q')!}{(k+q)!(k-q)!} \right]^{1/2} \left(\cos \frac{\beta}{2} \right)^{q'+q} \left(\sin \frac{\beta}{2} \right)^{q'-q} P_{k-q'}^{q'-q, q'+q}(\cos \beta), \quad (3.68)$$

where,

$$d_{q'q}^k(\beta) = (-1)^{q-q'} d_{qq'}^k(\beta) = d_{-q-q'}^k(\beta). \quad (3.69)$$

Note that, although Ref. [53] is an excellent reference, according to the symmetries of $d_{q'q}^k(\beta)$ there is a sign error in Table 1: $d_{2-1}^{(2)}(\beta) = (-1)^{-1-2} d_{-12}^{(2)}(\beta) = -d_{-12}^{(2)}(\beta)$.

Some terms in the hamiltonian are products of single-chromophore spin operators, like S_{Ax}^2 , that cannot be written with respect to the total spin. The triplet pair spin hamiltonian (Eq. 3.16) does not commute with the total spin operator $\mathbf{S} = \mathbf{S}_A + \mathbf{S}_B$. To evaluate

the hamiltonian in the total spin basis, I use the Wigner-Eckart theorem and rewrite the spin tensor operators as irreducible spherical tensor operators.

The spin operators \mathbf{S} , \mathbf{S}_A , and \mathbf{S}_B are Hermitian tensor operators—their components satisfy $\mathbf{T}_q^{k\dagger} = (-1)^q \mathbf{T}_{-q}^k$. The scalar product of two tensor operators of the same rank k was previously defined for Cartesian tensors in Eq. 3.70. The equivalent expression for spherical tensors is,⁴⁵

$$\mathbf{U}^{(k)} : \mathbf{V}^{(k)} = \sum_q (-1)^q \mathbf{U}_q^k \otimes \mathbf{V}_{-q}^k = \sum_q (-1)^q \mathbf{U}_{-q}^k \otimes \mathbf{V}_q^k = \left(\mathbf{U}^{(k)} : \mathbf{V}^{(k)} \right)^0, \quad (3.70)$$

which likewise gives a tensor of rank $k = 0$.

A reduced spherical tensor component can be written as the superposition of tensor products weighted by coefficients,

$$\mathbf{T}_q^k = \sum_{q_1, q_2} \mathbf{U}_{q_1}^{k_1} \otimes \mathbf{V}_{q_2}^{k_2} \langle k_1 q_1; k_2 q_2 | k_1 k_2; k q \rangle. \quad (3.71)$$

Similarly, a tensor product reduces to a sum of tensors,

$$\mathbf{U}_{q_1}^{k_1} \otimes \mathbf{V}_{q_2}^{k_2} = \sum_{k, q} \mathbf{T}_q^k \langle k_1 k_2; k q | k_1 q_1; k_2 q_2 \rangle. \quad (3.72)$$

The coefficients in Eqs. 3.71-3.72 are Clebsch-Gordan coefficients (Eq. 3.45)—expansion coefficients that arise when coupling angular momenta. The rank of the spherical tensor \mathbf{T}_q^k is determined by the same rules for coupling angular momenta: $|k_1 - k_2| \leq k \leq k_1 + k_2$ and $q = q_1 + q_2$.

According to Eq. 3.9, the Cartesian interaction tensors can be written as irreducible spherical tensors. The spherical tensor components are related to components of the

Cartesian tensors $\mathbf{O}^{(k)}$ according to,

$$\begin{aligned}
 \mathbf{O}^0 &= -1/\sqrt{3} (\mathbf{O}_{xx} + \mathbf{O}_{yy} + \mathbf{O}_{zz}) = -\text{Tr}(\mathbf{O})/\sqrt{3} \\
 \mathbf{O}_0^1 &= -i/\sqrt{2} (\mathbf{O}_{xy} - \mathbf{O}_{yx}) \\
 \mathbf{O}_{\pm 1}^1 &= -1/2 [\mathbf{O}_{zx} - \mathbf{O}_{xz} \pm i (\mathbf{O}_{zy} - \mathbf{O}_{yz})] \\
 \mathbf{O}_0^2 &= 1/\sqrt{6} [3\mathbf{O}_{zz} - (\mathbf{O}_{xx} + \mathbf{O}_{yy} + \mathbf{O}_{zz})] \\
 \mathbf{O}_{\pm 1}^2 &= \mp 1/2 [\mathbf{O}_{xz} + \mathbf{O}_{zx} \pm i (\mathbf{O}_{yz} + \mathbf{O}_{zy})] \\
 \mathbf{O}_{\pm 2}^2 &= 1/2 [\mathbf{O}_{xx} - \mathbf{O}_{yy} \pm i (\mathbf{O}_{xy} + \mathbf{O}_{yx})].
 \end{aligned} \tag{3.73}$$

The spherical tensor components of a rank-2 irreducible tensor in its *principle frame* (Eq. 3.32) are,

$$\begin{aligned}
 \mathbf{O}^0 &= -\text{Tr}(\mathbf{O})/\sqrt{3} \\
 \mathbf{O}_0^1 &= 0 \\
 \mathbf{O}_{\pm 1}^1 &= 0 \\
 \mathbf{O}_0^2 &= \sqrt{2/3} (\mathbf{O}_{zz} - \text{Tr}(\mathbf{O})/3) \\
 \mathbf{O}_{\pm 1}^2 &= 0 \\
 \mathbf{O}_{\pm 2}^2 &= 1/2 (\mathbf{O}_{xx} - \mathbf{O}_{yy}).
 \end{aligned} \tag{3.74}$$

Likewise, the tensor product spin operators $\mathbf{T}^{(k)} \equiv (\mathbf{U} \otimes \mathbf{V})^{(k)}$ for either single spins $(\mathbf{S}_A^{(k)} \otimes \mathbf{1})^{(k)}$ or the product of two spins, $(\mathbf{S}_A \otimes \mathbf{S}_B)^{(k)}$ (Eq. 3.14), have a spherical tensor representation. The spherical tensor operator components (Eq. 3.71) are related to the

products of Cartesian tensor operator components according to,

$$\begin{aligned}
 \mathbf{T}^0 &= -1/\sqrt{3} (\mathbf{U}_x \mathbf{V}_x + \mathbf{U}_y \mathbf{V}_y + \mathbf{U}_z \mathbf{V}_z) \\
 \mathbf{T}_0^1 &= i/\sqrt{2} (\mathbf{U}_x \mathbf{V}_y - \mathbf{U}_y \mathbf{V}_x) \\
 \mathbf{T}_{\pm 1}^1 &= 1/2 [\mathbf{U}_z \mathbf{V}_x - \mathbf{U}_x \mathbf{V}_z \pm i (\mathbf{U}_z \mathbf{V}_y - \mathbf{U}_y \mathbf{V}_z)] \\
 \mathbf{T}_0^2 &= 1/\sqrt{6} [3\mathbf{U}_z \mathbf{V}_z - (\mathbf{U}_x \mathbf{V}_x + \mathbf{U}_y \mathbf{V}_y + \mathbf{U}_z \mathbf{V}_z)] \\
 \mathbf{T}_{\pm 1}^2 &= \mp 1/2 [\mathbf{U}_x \mathbf{V}_z + \mathbf{U}_z \mathbf{V}_x \pm i (\mathbf{U}_y \mathbf{V}_z + \mathbf{U}_z \mathbf{V}_y)] \\
 \mathbf{T}_{\pm 2}^2 &= 1/2 [\mathbf{U}_x \mathbf{V}_x - \mathbf{U}_y \mathbf{V}_y \pm i (\mathbf{U}_x \mathbf{V}_y + \mathbf{U}_y \mathbf{V}_x)].
 \end{aligned} \tag{3.75}$$

Note the phase differences between Eqs. 3.73 and 3.75.

In summary, the *JDE* model spin hamiltonian in spherical tensor notation is,

$$\mathcal{H} = \sum_{k=0}^2 \mathbf{O}_{AB}^{(k)} : \mathbf{T}_{AB}^{(k)} + \mathbf{O}_A^{(k)} : \mathbf{T}_A^{(k)} + \mathbf{O}_B^{(k)} : \mathbf{T}_B^{(k)}, \tag{3.76}$$

where, from Eqs. 3.21, 3.42, 3.36 and 3.39,

$$\begin{array}{lll}
 \mathbf{O}_{AB}^0 = J & \mathbf{O}_A^0 \equiv 0 & \mathbf{O}_B^0 \equiv 0 \\
 \mathbf{O}_{AB}^{(1)} = \mathbf{d}_{AB} & \mathbf{O}_A^{(1)} = \mathbf{d}_A & \mathbf{O}_B^{(1)} = \mathbf{d}_B \\
 \mathbf{O}_{AB}^{(2)} = \mathbf{X} & \mathbf{O}_A^{(2)} = \mathbf{D}_A & \mathbf{O}_B^{(2)} = \mathbf{D}_B,
 \end{array} \tag{3.77}$$

and,

$$\begin{aligned} \mathbf{T}_{AB}^0 &= (\mathbf{S}_A : \mathbf{S}_B)^0 & \mathbf{T}_A^0 &\equiv 0 & \mathbf{T}_B^0 &\equiv 0 \\ \mathbf{T}_{AB}^{(1)} &= (\mathbf{S}_A \otimes \mathbf{S}_B)^{(1)} & \mathbf{T}_A^{(1)} &= \left((\mathbf{s}_1 \otimes \mathbf{s}_2)^{(1)} \otimes \mathbf{1} \right)^{(1)} & \mathbf{T}_B^{(1)} &= \left(\mathbf{1} \otimes (\mathbf{s}_3 \otimes \mathbf{s}_4)^{(1)} \right)^{(1)} \\ \mathbf{T}_{AB}^{(2)} &= (\mathbf{S}_A \otimes \mathbf{S}_B)^{(2)} & \mathbf{T}_A^{(2)} &= \left(\mathbf{S}_A^{(2)} \otimes \mathbf{1} \right)^{(2)} & \mathbf{T}_B^{(2)} &= \left(\mathbf{1} \otimes \mathbf{S}_B^{(2)} \right)^{(2)}, \end{aligned} \quad (3.78)$$

noting that label conventions follow those in Fig. 2.1 and that the rank of spin operators is one unless indicated.

3.3.2 The Rotated JDE Model

The spin operators in Eq. 3.76 are defined with respect to the lab frame (Fig. 3.3c). However, I derived the interaction tensors with respect to the single-chromophore and dimer frames (Fig. 3.3a and 3.3b). To evaluate the *JDE* model in the lab frame, all tensors in Eq. 3.76 must be rotated from the respective frames in which their parameters are defined into the lab frame. A three-dimensional rotation of a coordinate frame or body can be expressed as a sequence of rotations about a chosen set of axes by three Euler angles. A passive rotation rotates the coordinate frame while leaving the body fixed, while an active rotation rotates the body with respect to the body-fixed reference frame. Because the interactions are irreducible in their original frames, Eq. 3.66 says that these rotations will not change the rank of the interaction.

Following convention, the rank-two intra-chromophore interactions are parameterized by D and E (Eq. 3.34), which are defined with respect to a chromophore's principal frame, assumed to coincide with its molecular frame (Fig. 3.3a). In the single-chromophore principal frames, $\mathbf{D}_A = \mathbf{D}_B = \mathbf{D}$ (Eq. 3.33). For non-parallel chromophores,

however, the principal frames do not coincide so to evaluate the hamiltonian the tensors must be written with respect to a mutual frame of reference in which $\mathbf{D}'_A \neq \mathbf{D}'_B$. I choose to first rotate the single-chromophore interactions from their principal frames into the dimer frame by mirrored active (A) rotations about the molecular axes of the chromophore in its original orientation. The coordinate system remains fixed throughout the rotation while the physical system is redefined under rotation (Fig. 3.4a). For example, the interaction tensor \mathbf{O} is reoriented by the active rotation:

1. Rotate the body about its z -axis counterclockwise through the angle $0 \leq \alpha < 2\pi$ to bring O_x to O'_x and O_y to O'_y .
2. Rotate the body about its original y -axis counterclockwise through the angle $0 \leq \beta < \pi$ to bring O'_x to O''_x and O_z to O'_z .
3. Rotate the body about its original z -axis counterclockwise through the angle $0 \leq \gamma < 2\pi$ to yield the rotated interaction tensor with the renormalized elements O'''_x , O'_y , and O''_z .

These rotations take the diagonal matrix \mathbf{D} into a non-diagonal form $\mathbf{D}'_A \neq \mathbf{D}'_B$. Because \mathbf{D}_A and \mathbf{D}_B are irreducible, however, the rotated tensors \mathbf{D}'_A and \mathbf{D}'_B are also rank-two. In the lab frame, they are each described by five independent parameters (Eq. 3.12): D , E , α , β and γ .

In an applied Zeeman field where the induced Zeeman splittings are large relative to the zero-field splitting, it is natural to choose the quantization axis to lie along the lab z -axis. The interaction tensors are then rotated from the dimer frame into the lab frame defined by $\vec{B}_0 = (0, 0, B_0)$ (Figs. 3.2c, 3.3b, and 3.3c). A passive (P) rotation of the interaction tensors re-expresses their magnitude with respect to the lab z -axis, which only

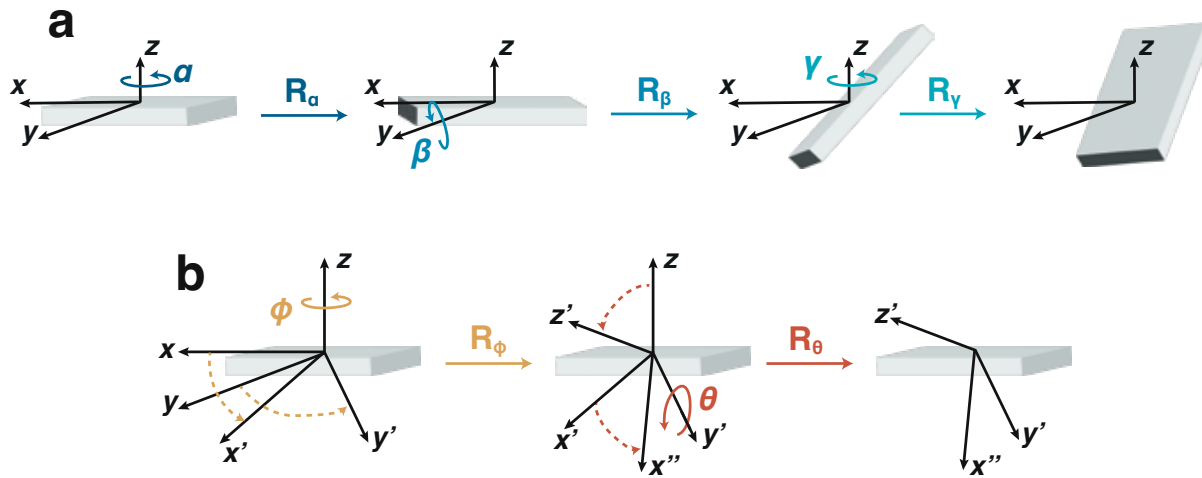


FIGURE 3.4: (a) An active rotation rotates the chromophores into the dimer frame (Fig. 3.3b). (b) A passive rotation of the dimer frame expresses the hamiltonian with respect to the lab frame (Fig. 3.3c).

necessitates two of the three Euler angles (Fig. 3.4b). The rotation leaves the tensors fixed but changes the coordinate system until it is coincident with the final frame:

1. Rotate the coordinate system counterclockwise about the original body-fixed z -axis through the angle $0 \leq \phi < 2\pi$ to give new axes x' and y' .
2. Rotate the coordinate system counterclockwise about the new body-fixed y' -axis through angle $0 \leq \theta < \pi$ to give the new axes (the lab axes) x'' and z' .

In summary, the rotated tensors are,

$$\begin{aligned}
 \mathbf{D}_A &= R_P(\phi, \theta) R_A(\Omega) \mathbf{D} R_A^{-1}(\Omega) R^{-1}(\phi, \theta) \\
 \mathbf{D}_B &= R_P(\phi, \theta) R_A(-\Omega) \mathbf{D} R_A^{-1}(-\Omega) R_P^{-1}(\phi, \theta) \\
 \mathbf{d}_A &= R_P(\phi, \theta) \mathbf{d}_A R_P^{-1}(\phi, \theta) \\
 \mathbf{d}_B &= R_P(\phi, \theta) \mathbf{d}_B R_P^{-1}(\phi, \theta) \\
 \mathbf{d}_{AB} &= R_P(\phi, \theta) \mathbf{d}_{AB} R_P^{-1}(\phi, \theta) \\
 \mathbf{X} &= R_P(\phi, \theta) \mathbf{X} R_P^{-1}(\phi, \theta),
 \end{aligned} \tag{3.79}$$

where $\Omega \equiv \{\alpha, \beta, \gamma\}$ is the rotation from the principal frames into the dimer frame. The final transformation (ϕ, θ) into the lab frame aligns the dimer z-axis to \vec{B}_0 . This allows one to relate features in the spectrum to dimer symmetries and allows us to use intuition based on single-triplet EPR spectra when analyzing the ${}^5\text{TT}$ spectra.

According to Eq. 3.70, the JDE model hamiltonian from Eq. 3.76 is written with respect to the lab frame as,

$$\mathcal{H} = \sum_{k=0}^2 \sum_{q=-k}^{+k} (-1)^q \left[\mathbf{O}_{AB, -q}^k \mathbf{T}_{AB, q}^k + \mathbf{O}_{A, -q}^k \mathbf{T}_{A, q}^k + \mathbf{O}_{B, -q}^k \mathbf{T}_{B, q}^k \right]. \tag{3.80}$$

The interaction tensor components in the lab frame \mathbf{O}_{-q}^k are the transformed tensor components from the dimer frame $\mathbf{O}_{q'}^k$. For example, from Eq. 3.66,

$$\mathbf{O}_{-q}^k = \sum_{q'=-k}^{+k} \mathcal{D}_{-q, q'}^k(\phi, \theta) \mathbf{O}_{q'}^k, \tag{3.81}$$

where (ϕ, θ) describe the rotation from the dimer frame to the lab frame. The hamiltonian in the lab frame with respect to the dimer frame is,

$$\mathcal{H} = \sum_{k=0}^2 \sum_{q=-k}^{+k} (-1)^q \mathcal{D}_{-q,q'}^k(\phi, \theta) \left[\mathbf{O}_{AB,q'}^k \mathbf{T}_{AB,q}^k + \mathbf{O}_{A,q'}^k \mathbf{T}_{A,q}^k + \mathbf{O}_{B,q'}^k \mathbf{T}_{B,q}^k \right]. \quad (3.82)$$

Conventionally, the values D and E are reported for the ZFS interaction, which are defined in the ZFS principal frames. For non-parallel chromophores, these do not coincide with the dimer frame. The interaction tensor components in the dimer frame $\mathbf{O}_{A,q'}^2$ and $\mathbf{O}_{B,q'}^2$ can instead be written as the rotated components from the principal frames, $\mathbf{O}_{A,q''}^2$ and $\mathbf{O}_{B,q''}^2$. For example,

$$\begin{aligned} \mathbf{O}_{A,q'}^2 &= \sum_{q''=-2}^{+2} \mathcal{D}_{q',q''}^2(\Omega) \mathbf{O}_{A,q''}^2 \\ \mathbf{O}_{B,q'}^2 &= \sum_{q''=-2}^{+2} \mathcal{D}_{q',q''}^2(-\Omega) \mathbf{O}_{B,q''}^2, \end{aligned} \quad (3.83)$$

where Ω and $-\Omega$ describe mirrored Euler rotations from the single-chromophore molecular frames into the dimer frame. In their respective single-chromophore frame, the intra-chromophore rank-2 interaction tensor components are equivalent, $\mathbf{O}_{A,q''}^2 = \mathbf{O}_{B,q''}^2$, and $\mathbf{O}_{A,0}^2 = \sqrt{2/3} D$, $\mathbf{O}_{A,\pm 1}^2 = 0$, and $\mathbf{O}_{A,\pm 2}^2 = E$ (Eq. 3.73). Because I am only interested in the selection rules for the relatively weak rank-1 interactions and because they are too weak to resolve from an EPR spectrum, I assume that the values for the interactions in $\mathbf{O}_A^{(1)}$ and $\mathbf{O}_B^{(1)}$ are reported with respect to the dimer frame so that the rank-1 tensors do not need to be further rotated. But, for non-parallel chromophores they are not equivalent, $\mathbf{O}_A^{(1)} \neq \mathbf{O}_B^{(1)}$.

The hamiltonian in the lab frame written with respect to the ZFS interactions in their corresponding single-chromophore molecular frames is,

$$\begin{aligned} \mathcal{H} = & J \mathbf{T}_{AB}^0 + \sum_{q,q'=-1}^{+1} (-1)^q \mathcal{D}_{-q,q'}^1(\phi, \theta) \left[\mathbf{O}_{AB,q'}^1 \mathbf{T}_{AB,q}^1 + \mathbf{O}_{A,q'}^1 \mathbf{T}_{A,q}^1 + \mathbf{O}_{B,q'}^1 \mathbf{T}_{B,q}^1 \right] \\ & + \sum_{q,q',q''=-2}^{+2} (-1)^q \mathcal{D}_{-q,q'}^2(\phi, \theta) \mathbf{O}_{AB,q'}^2 \mathbf{T}_{AB,q}^2 \\ & + \sum_{q,q',q''=-2}^{+2} (-1)^q \mathcal{D}_{-q,q'}^2(\phi, \theta) \left[\mathcal{D}_{q',q''}^2(\Omega) \mathbf{O}_{A,q''}^2 \mathbf{T}_{A,q}^2 + \mathcal{D}_{q',q''}^2(-\Omega) \mathbf{O}_{B,q''}^2 \mathbf{T}_{B,q}^2 \right]. \end{aligned} \quad (3.84)$$

The first term is the isotropic inter-chromophore exchange interaction, the second is the inter- and intra-chromophore rank-one interactions, the third is the inter-chromophore dipole-dipole interaction, and the fourth is the intra-chromophore dipole-dipole interactions.

For parallel chromophores $\Omega = -\Omega = \{0, 0, 0\}$, so $\mathbf{O}_{A,q'}^2 = \mathbf{O}_{B,q'}^2$ in the dimer frame. Likewise, $\mathbf{O}_{A,q'}^1 = \mathbf{O}_{B,q'}^1$. The *JDE* model hamiltonian for parallel chromophores is,

$$\mathcal{H} = \sum_{k,q,q'} (-1)^q \mathcal{D}_{-q,q'}^k(\phi, \theta) \left[\mathbf{O}_{AB,q'}^k \mathbf{T}_{AB,q}^k + \mathbf{O}_{A||B,q'}^k (\mathbf{T}_{A,q}^k + \mathbf{T}_{B,q}^k) \right]. \quad (3.85)$$

For the parallel case, the spin tensor operators $\mathbf{T}_{A,q}^k$ and $\mathbf{T}_{B,q}^k$ factor out of the expression and this has a significant impact on the selection rules (Sections 3.3.7 and 3.3.9).

Like the Wigner rotation matrix elements, $\mathcal{D}_{q,q'}^k$ (Eq. 3.67), the matrix elements of the interaction tensor components \mathbf{O}_q^k are simply scalar coefficients (Eq. 3.77). The Wigner-Eckart theorem is applied to evaluate the matrix elements of the spin tensor operator components \mathbf{T}_q^k . I explicitly derive these for all relevant \mathbf{T}_q^k in the following sections.

3.3.3 Matrix Elements from the Wigner-Eckart Theorem

The Wigner-Eckart theorem says that the matrix elements $\langle S', M' | \mathbf{T}_q^k | S, M \rangle$ are equal to the product of a coupling coefficient and reduced matrix element,⁴⁵

$$\langle S', M' | \mathbf{T}_q^k | S, M \rangle = (-1)^{S'-M'} \begin{pmatrix} S' & k & S \\ -M' & q & M \end{pmatrix} \langle S' || \mathbf{T}^{(k)} || S \rangle, \quad (3.86)$$

where $\{|S, M\rangle\}$ is the eigenbasis of the total spin operator \mathbf{S}^2 and \mathbf{T}_q^k is the q -th component of the rank- k irreducible spherical tensor operator. Here, \mathbf{T}_q^k operators on the total spin space spanned by the $|S, M\rangle$ states. The first term in Eq. 3.86, the 2×3 coupling coefficient, is called a $3j$ -symbol. It derives from Clebsh-Gordan coefficients and represents an integral over angular momentum functions. It guarantees the conservation of angular momentum; it is nonzero for $M' = M + q$ and $|S - k| \leq S' \leq S + k$. While there is it does not depend on the physical nature of \mathbf{T}_q^k , it does depend on the rank k and orientation q of the tensor—specifically, the system’s orientation with respect to the quantization axis, which in the JDE model is the lab z -axis. Solutions to the $3j$ -symbols can be found in look-up tables.⁴⁵

The last term in Eq. 3.86 is called the reduced matrix element because it is independent of the orientation of the system (i.e., M , M' , and q). It describes the evolution of the physical properties of the system that are invariant under rotations. When the reduce matrix element is expressed in the eigenspace of its tensor operator, it is solved in the obvious way. It is often most simple to evaluate the matrix element for $q = 0$. For example, the

solution to $\langle S'_A || \mathbf{S}_A || S_A \rangle$ comes from Eq. 3.86,

$$\langle S' || \mathbf{T}^{(k)} || S \rangle = (-1)^{-S'+M'} \frac{\langle S', M' | \mathbf{T}_q^k | S, M \rangle}{\begin{pmatrix} S' & k & S \\ -M' & q & M \end{pmatrix}}. \quad (3.87)$$

3.3.4 Reduced Matrix Elements from the Wigner-Eckart Theorem

Recoupling of angular momenta takes into account the multiple coupling schemes possible when coupling more than one. Recoupling coefficients are unitary transformations that take states between the different coupling schemes. The coupling order determines the phase of the resulting state $|S, M\rangle$, so it is necessary to consider the different intermediate values that can give a particular final value of S . For example, $S_1 = 0$ and $S_2 = 2$ can couple to $S = 2$ while, also, $S_3 = 1$ and $S_4 = 1$ can couple to $S = 2$. **Because the intermediate states are independent, the intermediate observables, or eigenvalues, must be specified.**

Suppose that $\mathbf{T}_q^k = (\mathbf{U}_{q_A}^{k_A} \otimes \mathbf{V}_{q_B}^{k_B})_q^k$, where A and B indicate subspaces of the total spin space. $\mathbf{U}_{q_A}^{k_A}$ operates on the spin space of chromophore A and $\mathbf{V}_{q_B}^{k_B}$ operates on the spin space of chromophore B so that the $\mathbf{U}_{q_A}^{k_A}$ and $\mathbf{V}_{q_B}^{k_B}$ commute. The matrix elements of tensor products of commuting operators are,

$$\langle S' M' | \mathbf{T}_q^k | S M \rangle = (-1)^{S'-M'} \begin{pmatrix} S' & k & S \\ -M' & q & M \end{pmatrix} \langle S'_A S'_B; S' || (\mathbf{U}_A \otimes \mathbf{V}_B)^{(k)} || S_A S_B; S \rangle. \quad (3.88)$$

For $\mathbf{U}_A = \mathbf{S}_A$ and $\mathbf{V}_B = \mathbf{S}_B$ the reduced matrix elements are,

$$\begin{aligned} \langle S'_A S'_B; S' | (\mathbf{S}_A \otimes \mathbf{S}_B)^{(k)} | S_A S_B; S \rangle &= [(2S+1)(2S'+1)(2k+1)]^{1/2} \\ &\times \left\{ \begin{array}{ccc} S'_A & S_A & 1 \\ S'_B & S_B & 1 \\ S' & S & k \end{array} \right\} \langle S'_A | |\mathbf{S}_A| |S_A\rangle \langle S'_B | |\mathbf{S}_B| |S_B\rangle. \end{aligned} \quad (3.89)$$

The 3×3 array in Eq. 3.89 is a recoupling coefficient, a $9j$ -symbol. By recognizing that the coupled angular momentum from different permutations of uncoupled angular momenta are related through rotations, only one calculation is necessary to consider all $(2S_A + 1)(2S'_A + 1)(2S_B + 1)(2S'_B + 1)$ coupling schemes.

Consider the matrix elements of the scalar product of commuting tensor operators $\mathbf{T}^{(0)} = (\mathbf{S}_A : \mathbf{S}_B)^0$. According to Eqs. 3.88 and 3.89 for $k = q = 0$ and $k_A = k_b = 1$,

$$\begin{aligned} \langle S'_A S'_B; S' M' | (\mathbf{S}_A : \mathbf{S}_B)^0 | S_A S_B; S M \rangle &= (-1)^{S_A + S'_B + S} \left\{ \begin{array}{ccc} S & S'_B & S'_A \\ 1 & S_A & S_B \end{array} \right\} \\ &\times \langle S'_A | |\mathbf{S}_A| |S_A\rangle \langle S'_B | |\mathbf{S}_B| |S_B\rangle \delta_{S', S} \delta_{M', M}. \end{aligned} \quad (3.90)$$

When k_A , k_B , or k is equal to zero, the $9j$ -symbol in Eq. 3.89 simplifies to a 2×3 $6j$ -symbol. Solutions to the reduce matrix elements $\langle S'_A | |\mathbf{S}_A| |S_A\rangle$ and $\langle S'_B | |\mathbf{S}_B| |S_B\rangle$ are given by Eq. 3.87.

The single-chromophore ZFS hamiltonians (Eq. 3.36) are a function of single chromophore tensor operators. For example, the ZFS hamiltonian for chromophore A is a function of the tensor operator components $\mathbf{T}_q^k = (\mathbf{S}_{A,q}^k \otimes \mathbf{1})_q^k$, where $k_A = k$, $q_A = q$,

$k_B = 0$, and $q_B = 0$. In this case, the reduced matrix element in Eq. 3.89 simplifies to,

$$\begin{aligned} \langle S'_A S'_B; S' | | (\mathbf{S}_A^{(k)} \otimes \mathbf{1})^{(k)} | | S_A S_B; S \rangle &= (-1)^{S'_A + S_B + S + k} [(2S+1)(2S'+1)]^{1/2} \\ &\times \left\{ \begin{array}{ccc} S'_A & S' & S_B \\ S & S_A & k \end{array} \right\} \langle S'_A | | \mathbf{S}_A | | S_A \rangle, \end{aligned} \quad (3.91)$$

or,

$$\begin{aligned} \langle S'_A S'_B; S' | | (\mathbf{1} \otimes \mathbf{S}_B^{(k)})^{(k)} | | S_A S_B; S \rangle &= (-1)^{S_A + S_B + S' + k} [(2S+1)(2S'+1)]^{1/2} \\ &\times \left\{ \begin{array}{ccc} S'_B & S' & S_A \\ S & S_B & k \end{array} \right\} \langle S'_B | | \mathbf{S}_B | | S_B \rangle. \end{aligned} \quad (3.92)$$

The reduced matrix elements for single-electron spin operators must be derived recursively. For the triplet pair, we start with either Eq. 3.91 or Eq. 3.92, depending on the relative subspace. Then, the spin states are again expanded to include the single electron spin operators \mathbf{s}_1 and \mathbf{s}_2 , or, \mathbf{s}_3 and \mathbf{s}_4 , respectively. For example, consider $\mathbf{S}_A = \mathbf{s}_1 + \mathbf{s}_2$. The tensor product of two operators that act on the same spin space do not commute. The reduced matrix element for $\mathbf{T}^{(k_A)} = (\mathbf{s}_1 \otimes \mathbf{s}_2)^{(k_A)}$ is,

$$\begin{aligned} \langle s'_1 s'_2; S'_A | | (\mathbf{s}_1 \otimes \mathbf{s}_2)^{(k_A)} | | s_1 s_2; S_A \rangle &= [2k_A + 1]^{1/2} (-1)^{k_A + S_A + S'_A} \\ &\times \sum_{S''_A, s''_1, s''_2} \left\{ \begin{array}{ccc} 1 & 1 & k_A \\ S_A & S'_A & S''_A \end{array} \right\} \\ &\times \langle s'_1 s'_2; S'_A | | \mathbf{s}_1 | | s''_1 s''_2; S''_A \rangle \langle s''_1 s''_2; S''_A | | \mathbf{s}_2 | | s_1 s_2; S_A \rangle. \end{aligned} \quad (3.93)$$

This simplifies for the triplet pair, where $S_A = S'_A = S''_A = 1$, $s_1 = s'_1 = s''_1 = 1/2$, and

$s_2 = s'_2 = s''_2 = 1/2$. The matrix elements for the electrons belonging to subspace B are found by substituting indices: $\{1, 2, A\} \rightarrow \{3, 4, B\}$.

3.3.5 Selection Rules from the Wigner-Eckart Theorem

If a system is originally in a state with a certain symmetry, and if the hamiltonian for this system is symmetrical under the operation of that symmetry, then the state will have the same symmetry for all time. Based on spherical tensor formalism, the Wigner-Eckart theorem gives the selection rules for transitions between the coupled spin states by simply considering rotational symmetries.

The Wigner $3j$ -symbol from Eq. 3.86 is a more symmetric representation of the physical consequence of coupling angular momenta (Eq. 3.45). The rank- k spin interaction represented by \mathbf{T}_q^k acts on spin states $|S, M\rangle$, and for $q \neq 0$ the interaction can transform the state, changing its angular momentum. The new state is $|S', M'\rangle$. The $3j$ -symbol requires that the three angular momenta, of magnitude S , S' and k , couple so that the resulting angular momentum is zero. The reduced product of the angular momenta is thus invariant under rotations. The $3j$ -symbol is zero unless the following conditions are satisfied,

1. $|S - k| \leq S' \leq S + k$
2. $q = M' - M$
3. $M \in \{-S, 1-S, \dots, S-1, S\}$, $M' \in \{-S', 1-S', \dots, S'-1, S'\}$, $q \in \{-k, 1-k, \dots, k-1, k\}$

The first rule is commonly referred to as a “triangle inequality” and is read off the first row of the $3j$ -symbol. In a similar manner, the second row of the $3j$ -symbol requires that

the change in the spin projection M following the operation $\mathbf{T}_q^k |S, M\rangle$ be equivalent to the magnitude of the tensor component, q .

Depending on the sign of the interaction, rank-0 operators favor either parallel or anti-parallel spin configurations by applying a uniform penalty proportional to the spin density. The observed affect on the energy of the system is only a function of the spin's magnitude S , independent of orientation. For $k = 0$, the initial and final states must have the same spin and projection, $\Delta S = 0$ and $\Delta M = 0$ (Table 3.3).

Rank-1 operators tend to rotate spin states into perpendicular configurations. The act of \mathbf{T}_q^1 on $|S, M\rangle$ cant the spin state $|S, M\rangle$ into the spin state $|S', M'\rangle$, where $S' = |S - 1|, S, S + 1$ and $M' = M + q$ (Table 3.3).

Rank-2 operators also align the spins but do so by applying an anisotropic energy penalty to the spin densities. The energy maximum $|\langle S, M | \mathbf{T}_q^2 | S, M \rangle|_{max}$ of the coaligned spins is along a specific axis. The selection rules from a rank-2 spherical tensor are $|S - 2| \leq S' \leq S + 2$ and $\Delta M = 0, \pm 1, \pm 2$ (Table 3.3).

The $q = 0$ total spin operator, S_z , is a constant of motion because it rotates the spin state $|S, M\rangle$ about the z -axis without changing it. The quantity observed upon the action of S_z —its eigenvalue, M —is said to be conserved if and only if the commutator, $[H, S_z] = HS_z - S_z H$, is zero. In fact, for each rank- k case, the $q = 0$ interaction does not change the orientation of the spin state with respect to the quantization axis, $M' = M$. The Cartesian representations of the $q = 0$ total spin spherical tensors are,

$$\begin{aligned}\mathbf{T}_0^1 &= S_z \\ \mathbf{T}_0^2 &= (3S_z^2 - \mathbf{S}^2) / \sqrt{6}.\end{aligned}\tag{3.94}$$

Total spin \mathbf{T}_0^k tensor operators commute with \mathbf{S}^2 —they are spin conserving, $\langle S', M' | \mathbf{T}_0^k | S, M \rangle \neq 0 \Leftrightarrow$

\mathbf{T}^0		\mathbf{T}_q^1		\mathbf{T}_q^2	
S	S'	S	S'	S	S'
0	0	0	1	0	2
1	1	1	0, 1, 2	1	1, 2
2	2	2	1, 2	2	0, 1, 2

\mathbf{T}_{-2}^k		\mathbf{T}_{-1}^k		\mathbf{T}_0^k		\mathbf{T}_{+1}^k		\mathbf{T}_{+2}^k	
M	M'	M	M'	M	M'	M	M'	M	M'
-2		-2		-2	-2	-2	-1	-2	0
-1		-1	-2	-1	-1	-1	0	-1	+1
0	-2	0	-1	0	0	0	+1	0	+2
+1	-1	+1	0	+1	+1	+1	+2	+1	
+2	0	+2	+1	+2	+2	+2		+2	

TABLE 3.3: Rotational symmetry selection rules from irreducible spherical tensor operators depend on the rank k and component q of the operator. This table shows the selection rules that connect the spin states. The matrix elements $\langle S', M' | \mathbf{T}_q^k | SM \rangle$ are non-zero for the specified cases, where S and M refer to the total spin and spin projection of the initial state and S' and M' refer to the final state.

$S' = S$. Though this does not hold for $q = 0$ operators that belong to subspaces of the total spin, like S_{Az} . The $q \neq 0$ operators transform $|S, M\rangle$ into $|S', M'\rangle = |S', M + q\rangle$.

Considering Eq. 3.86, all other selection rules from the Wigner-Eckart theorem come from the reduced matrix elements $\langle S' || \mathbf{T}^{(k)} || S \rangle$. The $6j$ - and $9j$ -symbols recoupling coefficients, are independent of q , M , and M' , but do depend on the intermediate angular momenta $\{S_A, S'_A, S_B, S'_B\}$. Because they consider different ways to couple the spins, they must satisfy additional triangle inequalities. For example, the $6j$ -symbol,

$$\left\{ \begin{array}{ccc} j_1 & j_2 & j_3 \\ j_4 & j_5 & j_6 \end{array} \right\}, \quad (3.95)$$

has four triads: (j_1, j_2, j_3) , (j_1, j_5, j_6) , (j_4, j_2, j_6) , and (j_4, j_5, j_3) . The triangle inequality $|x - y| \leq z \leq x + y$ must be satisfied for each triad (x, y, z) :

1. $|j_1 - j_2| \leq j_3 \leq j_1 + j_2$
2. $|j_1 - j_5| \leq j_6 \leq j_1 + j_5$
3. $|j_4 - j_2| \leq j_6 \leq j_4 + j_2$
4. $|j_4 - j_5| \leq j_3 \leq j_4 + j_5$

3.3.6 Isotropic Inter-chromophore Exchange Matrix Elements

Recall the isotropic inter-chromophore exchange hamiltonian from Eq. 3.21,

$$H_{AB}^{(0)} = \mathbf{O}_{AB}^0 : (\mathbf{S}_A : \mathbf{S}_B)^0 = J (\mathbf{S}_A : \mathbf{S}_B)^0. \quad (3.96)$$

The matrix element of the scalar product of commuting operators was given in Eq. 3.90. After substituting $S_A = S'_A = S_B = S'_B = 1$, for the triplet pair the isotropic exchange matrix elements are,

$$\langle S'_A S'_B; S' M' | (\mathbf{S}_A : \mathbf{S}_B)^0 | S_A S_B; S M \rangle = (-1)^S \left\{ \begin{array}{ccc} S & 1 & 1 \\ 1 & 1 & 1 \end{array} \right\} \langle S'_A || \mathbf{S}_A || S_A \rangle \langle S'_B || \mathbf{S}_B || S_B \rangle \delta_{S', S} \delta_{M', M}. \quad (3.97)$$

The reduced matrix elements are solved according to Eq. 3.87, shown explicitly below.

Section 3.3.5, showed that the $|S, M\rangle$ states are eigenstates of the $q = 0$ components of the total spin operators. Thus, it is natural to choose the simple case $q = 0$ and solve for the reduced matrix element using Eq. 3.87. Recall that for spin operators $k = 1$,

$$\begin{aligned} \langle S'_A M'_A | S_{Az} | S_A M_A \rangle &= M_A \delta_{S_A, S'_A} \delta_{M_A, M'_A} \\ &= \langle S'_A M'_A | \mathbf{S}_{A, 0} | S_A M_A \rangle \\ &= (-1)^{S'_A - M'_A} \left(\begin{array}{ccc} S'_A & 1 & S_A \\ -M'_A & 0 & M_A \end{array} \right) \langle S'_A || \mathbf{S}_A || S_A \rangle. \end{aligned} \quad (3.98)$$

Solutions for the $3j-$ and $6j-$ symbols are found in look up tables, where it may be useful to consider the symmetry properties of the symbols. From Edmonds,⁴⁵

$$\left(\begin{array}{ccc} S_A & 1 & S_A \\ -M_A & 0 & M_A \end{array} \right) = (-1)^{S_A - M_A} M_A [(2S_A + 1)(S_A + 1)S_A]^{-1/2}. \quad (3.99)$$

The reduced matrix element is,

$$\begin{aligned}\langle S'_A || \mathbf{S}_A || S_A \rangle &= [(2S_A + 1)(S_A + 1)S_A]^{1/2} \delta_{S_A, S'_A} \delta_{M_A, M'_A} \\ &= \sqrt{6} \delta_{S_A, S'_A} \delta_{M_A, M'_A},\end{aligned}\tag{3.100}$$

where δ is the Kronecker delta function. Because Eq. 3.87 holds for either subspace, $\langle S'_B || \mathbf{S}_B || S_B \rangle = \langle S'_A || \mathbf{S}_A || S_A \rangle$. Picking up from Eq. 3.97 and noting that,

$$\left\{ \begin{array}{ccc} S & 1 & 1 \\ 1 & 1 & 1 \end{array} \right\} = (-1)^{-S} (S(S+1)-4)/12,\tag{3.101}$$

the matrix elements for the isotropic exchange interaction are,

$$J \langle S'_A S'_B; S' M' | (\mathbf{S}_A : \mathbf{S}_B)^0 | S_A S_B; S M \rangle = \frac{J}{2} (S(S+1)-4) \delta_{S', S} \delta_{M', M}.\tag{3.102}$$

As predicted in Table 3.3, the isotropic exchange interaction connects states of the same spin S and projection M .

The isotropic exchange interaction can instead be written in terms of the total spin by considering the equivalent form,

$$J \mathbf{S}_A^\top \cdot \mathbf{S}_B = \frac{J}{2} \left(\mathbf{S}^2 - \mathbf{S}_A^2 - \mathbf{S}_B^2 \right),\tag{3.103}$$

where $\mathbf{S}^2 = (\mathbf{S}_A + \mathbf{S}_B)^2$. It is clear upon inspection that the isotropic inter-chromophore exchange operators commute with \mathbf{S}^2 , so the matrix elements are diagonal in the total

spin basis $\{|S_A, S_B; S, M\rangle\}$. In this case, it is simple to evaluate the matrix elements directly,

$$\begin{aligned}
 & \frac{J}{2} \langle S'_A, S'_B; S', M' | \mathbf{S}^2 - \mathbf{S}_A^2 - \mathbf{S}_B^2 | S_A, S_B; S, M \rangle \\
 &= \frac{J}{2} S(S+1) \langle S'_A, S'_B; S', M' | S_A, S_B; S, M \rangle \\
 &\quad - \frac{J}{2} (S_A(S_A+1) + S_B(S_B+1)) \langle S'_A, S'_B; S', M' | S_A, S_B; S, M \rangle \\
 &= \frac{J}{2} (S(S+1) - 4) \delta_{S,S'} \delta_{M,M'}.
 \end{aligned} \tag{3.104}$$

This generates the same expression as the one from the Wigner-Eckart theorem (Eq. 3.102).

3.3.7 Anisotropic Intra-chromophore Matrix Elements

Recall that the spin operators in the anisotropic intra-chromophore interaction hamiltonian in spherical tensor notation have the forms $\mathbf{S}_{A,q}^2$ and $\mathbf{S}_{B,q'}^2$, respectively, where the superscript denotes the rank $k = 2$. Because these are with respect to the intermediate spin operators, the matrix elements are evaluated according to the Wigner-Eckart theorem in Eq. 3.88. For example, the matrix element for spin- A is,

$$\begin{aligned}
 \langle S'_A S'_B; S' M' | (\mathbf{S}_{A,q}^2 \otimes \mathbf{1})_q^2 | S_A S_B; S M \rangle &= (-1)^{S'-M'} \left(\begin{array}{ccc} S' & 2 & S \\ -M' & q & M \end{array} \right) \\
 &\times \langle S'_A S'_B; S' | (\mathbf{S}_A^{(2)} \otimes \mathbf{1})^{(2)} | S_A S_B; S \rangle.
 \end{aligned} \tag{3.105}$$

For $S_A = 1$, the reduced matrix element from Eq. 3.91 is,

$$\begin{aligned} \langle S'_A S'_B; S' | \left(\mathbf{S}_A^{(2)} \otimes \mathbf{1} \right)^{(2)} | S_A S_B; S \rangle &= (-1)^S [(2S+1)(2S'+1)]^{1/2} \\ &\times \left\{ \begin{array}{ccc} 1 & S' & 1 \\ S & 1 & 2 \end{array} \right\} \langle S'_A | \mathbf{S}_A^{(2)} | S_A \rangle. \end{aligned} \quad (3.106)$$

The reduced matrix element $\langle S'_A | \mathbf{S}_A^{(2)} | S_A \rangle = \sqrt{5}$ is found by using Eq. 3.86, setting $k = 2$ and $q = 0$, and substituting for the Cartesian equivalent of the $\mathbf{T}_{A,0}^2$ spin operator (Eq. 3.94). The simplified matrix element for spin- A is,

$$\begin{aligned} \langle S'_A S'_B; S' M' | \left(\mathbf{S}_{A,q}^2 \otimes \mathbf{1} \right)_q^2 | S_A S_B; S M \rangle &= (-1)^{S'-M'} \left(\begin{array}{ccc} S' & 2 & S \\ -M' & q & M \end{array} \right) \\ &\times (-1)^S [5(2S+1)(2S'+1)]^{1/2} \left\{ \begin{array}{ccc} 1 & S' & 1 \\ S & 1 & 2 \end{array} \right\}. \end{aligned} \quad (3.107)$$

Similarly, the matrix element for spin- B is,

$$\begin{aligned} \langle S'_A S'_B; S' M' | \left(\mathbf{1} \otimes \mathbf{S}_{B,q}^2 \right)_q^2 | S_A S_B; S M \rangle &= (-1)^{S'-M'} \left(\begin{array}{ccc} S' & 2 & S \\ -M' & q & M \end{array} \right) \\ &\times (-1)^{S'} [5(2S+1)(2S'+1)]^{1/2} \left\{ \begin{array}{ccc} 1 & S' & 1 \\ S & 1 & 2 \end{array} \right\}. \end{aligned} \quad (3.108)$$

The matrix elements for $\mathbf{S}_{A,q}^2$ and $\mathbf{S}_{B,q}^2$ are identical except for their sign,

$$\langle \mathbf{S}_{A,q}^2 \rangle = (-1)^{S'+S} \langle \mathbf{S}_{B,q}^2 \rangle. \quad (3.109)$$

For nonparallel chromophores, the single-chromophore ZFS tensor components $\mathbf{D}_{A,q}^2$ and $\mathbf{D}_{B,q}^2$ are rotated independently so that the values of same- q components are not equivalent. The hamiltonian $H_A + H_B$ for nonparallel chromophores is not factorizable. But for **parallel** chromophores the interaction tensors are rotated together. In this case, the hamiltonian $H_A + H_B$ factorizes as (Eq. 3.85),

$$\begin{aligned} \langle S'_A S'_B; S' M' | \mathbf{S}_{A,q}^2 + \mathbf{S}_{B,q}^2 | S_A S_B; S M \rangle &= (-1)^{-M'} \left(\begin{array}{ccc} S' & 2 & S \\ -M' & q & M \end{array} \right) \\ &\times (-1)^{S'} [5(2S+1)(2S'+1)]^{1/2} \left\{ \begin{array}{ccc} 1 & S' & 1 \\ S & 1 & 2 \end{array} \right\} \quad (3.110) \\ &\times \left((-1)^{S+S'} + 1 \right). \end{aligned}$$

The selection rule,

$$\langle \mathbf{S}_{A,q}^2 + \mathbf{S}_{B,q}^2 \rangle \propto (1 + (-1)^{S'+S}), \quad (3.111)$$

comes from the exchange symmetry of the intra-chromophore hamiltonian, derived in Section 3.2.8 (Table 3.1).

3.3.8 Anisotropic Inter-chromophore Matrix Elements

To evaluate the matrix elements for the anisotropic inter-chromophore interaction, start with Eqs. 3.88 and 3.89. For $k = 2$,

$$\begin{aligned} \langle S'_A S'_B; S' M' | (\mathbf{S}_A \otimes \mathbf{S}_B)_q^2 | S_A S_B; S M \rangle &= (-1)^{S' - M'} \left(\begin{array}{ccc} S' & 2 & S \\ -M' & q & M \end{array} \right) \\ &\quad \times \langle S'_A S'_B; S' | | (\mathbf{S}_A \otimes \mathbf{S}_B)^{(2)} | | S_A S_B; S \rangle, \end{aligned} \quad (3.112)$$

where,

$$\begin{aligned} \langle S'_A S'_B; S' | | (\mathbf{S}_A \otimes \mathbf{S}_B)^{(2)} | | S_A S_B; S \rangle &= \langle S'_A | | \mathbf{S}_A | | S_A \rangle \langle S'_B | | \mathbf{S}_B | | S_B \rangle \\ &\quad [5(2S + 1)(2S' + 1)]^{1/2} \left\{ \begin{array}{ccc} 1 & 1 & 1 \\ 1 & 1 & 1 \\ S' & S & 2 \end{array} \right\}. \end{aligned} \quad (3.113)$$

The $9j$ -symbol does not simplify further. The single-chromophore reduced matrix elements for $k_A = k_B = 1$ were found in Eq. 3.100. The matrix element fully simplifies to,

$$\begin{aligned} \langle S'_A S'_B; S' M' | (\mathbf{S}_A \otimes \mathbf{S}_B)_q^2 | S_A S_B; S M \rangle &= (-1)^{S' - M'} \left(\begin{array}{ccc} S' & 2 & S \\ -M' & q & M \end{array} \right) \\ &\quad \times 6 [5(2S + 1)(2S' + 1)]^{1/2} \left\{ \begin{array}{ccc} 1 & 1 & 1 \\ 1 & 1 & 1 \\ S' & S & 2 \end{array} \right\}. \end{aligned} \quad (3.114)$$

The $9j$ -symbols must be evaluated numerically for given S and S' , however, $9j$ -symbols with identical rows vanish unless the sum over the unique row is even.⁵⁴ This reveals

the parity selection rule from Table 3.2—the anisotropic inter-chromophore hamiltonian is zero unless $S + S'$ is even.

3.3.9 Rank-1 Intra-chromophore Matrix Elements

The rank-1 intra-chromophore interactions cannot be evaluated in the total spin basis using Cartesian methods. The matrix elements from the Wigner-Eckart theorem (Eqs. 3.88 and 3.91) for spin A are,

$$\begin{aligned} \langle S'_A S'_B; S' M' | \left((\mathbf{s}_1 \otimes \mathbf{s}_2)_q^1 \otimes \mathbf{1} \right)_q^1 | S_A S_B; S M \rangle &= (-1)^{S' - M'} \begin{pmatrix} S' & 1 & S \\ -M' & q & M \end{pmatrix} \\ &\times \langle S'_A S'_B; S' | \left((\mathbf{s}_1 \otimes \mathbf{s}_2)^{(1)} \otimes \mathbf{1} \right)^{(1)} | S_A S_B; S \rangle, \end{aligned} \quad (3.115)$$

where,

$$\begin{aligned} \langle S'_A S'_B; S' | \left((\mathbf{s}_1 \otimes \mathbf{s}_2)^{(1)} \otimes \mathbf{1} \right)^{(1)} | S_A S_B; S \rangle &= (-1)^{S+1} [(2S+1)(2S'+1)]^{1/2} \\ &\times \begin{Bmatrix} 1 & S' & 1 \\ S & 1 & 1 \end{Bmatrix} \langle s'_1 s'_2; S'_A | (\mathbf{s}_1 \otimes \mathbf{s}_2)^{(1)} | s_1 s_2; S_A \rangle. \end{aligned} \quad (3.116)$$

The reduced matrix element in the last line are solved using Eqs. 3.93 and 3.100, where $s_1 = s_2 = 1/2$,

$$\begin{aligned} \langle s'_1 s'_2; S'_A | (\mathbf{s}_1 \otimes \mathbf{s}_2)^{(1)} | s_1 s_2; S_A \rangle &= -\frac{1}{2\sqrt{3}} \langle s'_1 | \mathbf{s}_1 | s_1 \rangle \langle s'_2 | \mathbf{s}_2 | s_2 \rangle \\ &= -\frac{1}{2\sqrt{3}} [(2s_1+1)(s_1+1)s_1]^{1/2} [(2s_2+1)(s_2+1)s_2]^{1/2} \\ &= -\frac{\sqrt{3}}{4}. \end{aligned} \quad (3.117)$$

The simplified rank-1, spin operator-*A* matrix elements are then,

$$\begin{aligned} \langle S'_A S'_B; S'M' | \left((\mathbf{s}_1 \otimes \mathbf{s}_2)_q^1 \otimes \mathbf{1} \right)_q^1 | S_A S_B; SM \rangle &= (-1)^{S'+S-M'} \begin{pmatrix} S' & 1 & S \\ -M' & q & M \end{pmatrix} \\ &\times [3(2S+1)(2S'+1)]^{1/2} / 4 \quad (3.118) \\ &\times \left\{ \begin{array}{ccc} 1 & S' & 1 \\ S & 1 & 1 \end{array} \right\}. \end{aligned}$$

Like the matrix elements of the rank-two intra-chromophore hamiltonian, the spin operator-*B* matrix element only differs from the matrix element for spin-*A* by a phase,

$$\begin{aligned} \langle S'_A S'_B; S'M' | \left(\mathbf{1} \otimes (\mathbf{s}_3 \otimes \mathbf{s}_4)_q^1 \right)_q^1 | S_A S_B; SM \rangle &= (-1)^{-M'} \begin{pmatrix} S' & 1 & S \\ -M' & q & M \end{pmatrix} \\ &\times [3(2S+1)(2S'+1)]^{1/2} / 4 \quad (3.119) \\ &\times \left\{ \begin{array}{ccc} 1 & S' & 1 \\ S & 1 & 1 \end{array} \right\}. \end{aligned}$$

The selection rules for the $3j$ -symbol are given in Table 3.3, where $S = 0$ and $S' = 1$ are connected through the rank-1 interaction. But the exchange symmetry requires that only $S + S' = even$ elements are non-zero for parallel chromophores (Table 3.1). This holds for both the rank-1 and rank-2 intra-chromophore hamiltonians because the exchange selection rule is independent of k .

3.3.10 Rank-1 Inter-chromophore Matrix Elements

The rank-1 inter-chromophore interaction matrix elements are,

$$\langle S'_A S'_B; S' M' | (\mathbf{S}_A \otimes \mathbf{S}_B)_q^1 | S_A S_B; S M \rangle = (-1)^{S' - M'} \begin{pmatrix} S' & 1 & S \\ -M' & q & M \end{pmatrix} \times 6 [3(2S + 1)(2S' + 1)]^{1/2} \begin{Bmatrix} 1 & 1 & 1 \\ 1 & 1 & 1 \\ S' & S & 1 \end{Bmatrix}. \quad (3.120)$$

As for the rank-2 inter-chromophore matrix elements, the $9j$ -symbol has two identical rows so that it vanishes unless the sum over the unique row is even.⁵⁴ This selection rule arises from the parity symmetry of the inter-chromophore hamiltonian, which depends on k (Table 3.2). It requires that the matrix elements of the antisymmetric inter-chromophore hamiltonian are zero unless $S + S'$ is odd.

3.4 Nonadiabatic Transition Theory for the JDE Model

At long times, paired excitons in crystalline structures may hop to neighboring sites and become increasingly more distant. In the limit that the distance between excitons becomes large, the exchange interaction goes to zero while the ZFS is unaffected. This is the strong coupling limit $|D| \gg |J|$, where here coupling refers to the coupling

between TT states, in which the full exciton hamiltonian,

$$\begin{aligned}\mathcal{H} &= H_{AB} + H_A + H_B \\ &= J\mathbf{S}_A^\top \cdot \mathbf{S}_B + \mathbf{S}_A^\top \cdot \mathbf{D}_A \cdot \mathbf{S}_A + \mathbf{S}_B^\top \cdot \mathbf{D}_B \cdot \mathbf{S}_B,\end{aligned}\tag{3.121}$$

simplifies to $H_A + H_B$. The equilibrium density matrix is,

$$\rho_{eq} = \frac{e^{-\beta H_A} e^{-\beta H_B}}{Z_A Z_B}.\tag{3.122}$$

In this adiabatic representation the equilibrium density matrix is factorizable $\rho_{eq} = \rho_A \otimes \rho_B$, suggesting that the entanglement of \mathbf{S}_A and \mathbf{S}_B depends on the distance between the excitons. At first this may seem reasonable, however entanglement is independent of distance and the coupling between A and B so ρ_{eq} is not necessarily factorizable. In fact, the isolated uncoupled triplets may not be independently representable.

As an alternative, consider the nonadiabatic weak coupling limit $|J| \gg |D|$ whose basis is the coupled Zeeman basis $\{|S, M\rangle\}$ (Eq. 3.47). Considering the JDE model hamiltonian (Eq. 3.76), the equilibrium density matrix at zero field thermalizes to,

$$\rho_{eq} = \gamma |^1\text{TT}\rangle \langle ^1\text{TT}| + (1 - \gamma) |^5\text{TT}_0\rangle \langle ^5\text{TT}_0| \tag{3.123}$$

where γ is the probability of being in state $|^1\text{TT}\rangle$. The coupled kets $|^1\text{TT}\rangle$ and $|^5\text{TT}_0\rangle$ are nonseparable with respect to \mathbf{S}_A and \mathbf{S}_B (Eq. 3.47) and thus the equilibrium density matrix describes an entangled state.

The conditions for a fast, nonadiabatic transition to a pure state are satisfied for $|J| \gg |D|$ when fluctuations in J are on the order of $\Delta E_{^1\text{TT}-^5\text{TT}_0} \sim 3J$ (Fig. 2.2). For quantum

computing, the relevant states at finite temperature are the $|S, M\rangle$ diabatic states.

3.4.1 Choice of Basis for the JDE model

Rare stochastic fluctuations in the large exchange interaction J rapidly bring different ^{2S+1}TT spin states close in energy so that weak zero-field perturbations, D , X , and E , can promote population transfer between the singlet and quintet state and, subsequently, the quintet and triplet state. I aim to model the prompt EPR spectrum, where the ^1TT population has already evolved into an EPR active state that in turn remains steady over a given period of time. Under these conditions, $|J| \gg |D| \gg |X|$ and $|E|$, we refer to the observed spin as being “well-defined”—meaning that the states that describe the triplet pair do not have mixed-spin “character.” The spectra calculated with the short time approximation are purely from the initially formed quintet state, $^1\text{TT} \rightarrow ^5\text{TT}$.

The $|S, M\rangle$ states form the Zeeman, or diabatic, basis where S and M are the total spin and the total spin projection. The adiabatic states are linear superpositions of the diabatic states: $|S, \alpha\rangle = \sum_M \alpha_M |S, M\rangle$. They are the eigenstates of the quintet block of the hamiltonian (Fig. 3.5b). By restricting diagonalization to a specific spin subspace, S remains well-defined.

The coefficients $\alpha_M = \langle S, M | S, \alpha_M \rangle$ are functions of the adiabatic interactions, D , X , and E , and are therefore different for different orientations (α , β , γ , θ , and ϕ) (see Section 3.3.2 and Fig. 3.2). Although the spectra from the adiabatic states may resemble the data more closely, the diabatic spectrum is still a good fit (Chapter 4). By expressing the hamiltonian in the diabatic basis, spectral features can be assigned to specific transitions between specific states—even in a disordered sample. This is a significant advantage for quantum computing applications.

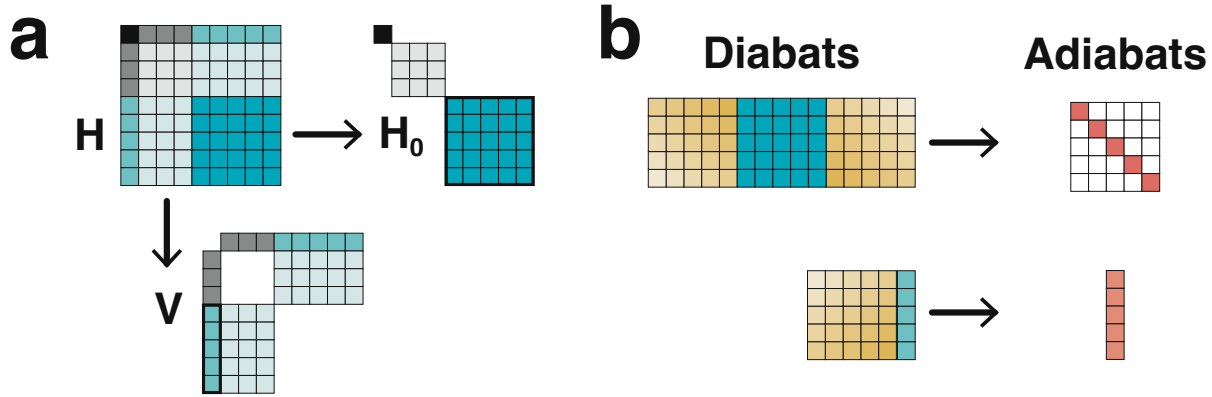


FIGURE 3.5: (a) In the $|S, M\rangle$ basis, the *JDE* model hamiltonian partitions into block diagonal and off-diagonal parts. The diagonal parts contain subspaces with singlet (1×1), triplet (3×3), and quintet (5×5) multiplicities, and the off-diagonal blocks couple states of different multiplicities. $P = \sum_{M,M'} |^{2S+1}\text{TT}_{M'}\rangle \langle ^{2S+1}\text{TT}_M|$ projects out the diagonal blocks, $H_0 = PHP$, and the coupling blocks are what remain, $V = H - H_0$. (b) A unitary transformation (represented by yellow blocks) takes the quintet block of the hamiltonian from its representation in the diabatic basis to a diagonal representation, referred to as the adiabatic representation. The adiabatic states are linear combinations of the same-spin Zeeman states, $|S, \alpha\rangle = \sum_M \alpha_M |S, M\rangle$. The same transformation is applied to the coupling matrix block to transform it into the adiabatic basis. Elements of the 5×1 coupling block, shown, couple the ^1TT state with $^5\text{TT}_M$ (blue) or $^5\text{TT}_\alpha$ (red) sublevels.

3.4.2 Calculating the Quintet State Populations

To calculate $^5\text{TT}_M$ populations, I apply the *JDE* model which is founded in perturbation theory (Chapter 2). The hamiltonian is of the form of Eq. 3.121. It can be simplified by accounting for specific dimer symmetries or setting weak (unresolved) interactions, like X or E , to zero. What follows generalizes to any of these cases in the large J limit.

The hamiltonian in the Zeeman, or diabatic, basis is first partitioned into a sum of block-diagonal, H_0 , and block off-diagonal parts, V (Fig. 3.5a). $P = \sum_{M,M'} |^5\text{TT}_{M'}\rangle \langle ^5\text{TT}_M|$ is a projection operator that projects out the diagonal blocks of H , so that $H_0 = PHP$ (Fig. 3.5a). The off-diagonal blocks are then $V = H - H_0$. The strong interactions, J and

B_0 , only appear in H_0 ; they split the energies of the total spin states. V only contains weak perturbations, D , X , and E , that cause transitions between spin states.

It is somewhat remarkable, and not at all obvious, that the magnetic fields produced by the triplets couple the $|S, M\rangle$ spin states. For quantum computing, we must consider the dimer symmetries that dictate the magnitudes of D , X and E to encourage selective transitions. Compared to the diagonal interactions, B_0 and J , the anisotropic zero-field interactions D , X , and E are relatively weak so that the coupling can be treated perturbatively.

I stress that this result is unique for the chosen representation: (1) The hamiltonian in the chosen frame of reference—the lab frame—where \vec{B}_0 defines the quantization axis, and (2) A total spin S basis, either the diabatic or adiabatic, where only same-spin states can mix. There are then two contrasting cases. If a molecular interaction-based frame of reference is chosen, the Zeeman interaction is not diagonal in the total spin basis. In this case, V becomes a function of the strong applied field, $B_0 \approx 10$ GHz, and perturbation theory becomes an invalid approach. Likewise, if the hamiltonian is expressed with respect to the uncoupled $|S_A, m_A; S_B, m_B\rangle$ states, V is a function of the strong exchange interaction, $|J| \geq 20$ GHz. These distinctions may become insignificant, for example, if the populations are treated as fit parameters, but they are a requirement for nonadiabatic transition theory.

3.4.3 Calculating the EPR Spectrum

Spectral fitting and calculations are performed with in-house programs written in the Julia programming language. The spin hamiltonian is used to calculate the transition

energies and intensities of the quintet EPR spectrum. It is evaluated in one of two bases—the adiabatic basis $\{|S, \alpha\rangle\}$, or diabatic basis $\{|S, M\rangle\}$. For convenience, the procedure for calculating the spectrum will be discussed with respect to the $\{|S, M\rangle\}$ basis, but this is without loss of generality.

For a given orientation, the program solves the strong-field *JDE* model hamiltonian, which is equivalent to the zero-field hamiltonian (Eq. 3.121) plus the Zeeman hamiltonian,

$$H_{\text{Zeeman}} = g\mu_B B_0 S_z, \quad (3.124)$$

over a range of B_0 , where μ_B is the Bohr magneton, $S_z = S_{Az} + S_{Bz}$ is the total spin along the lab z -axis, and g is its g -factor. Then a line spectrum is constructed by minimizing $\Delta E(B_0) = g\mu_B B_1$ for the four $\Delta M = \pm 1$ transitions. Here, B_1 is the magnitude of the applied microwave frequency and $\Delta E(B_0)$ is the energy gap between the $\Delta M = \pm 1$ states. The four lines are broadened by a Gaussian or Lorentzian lineshape, whose linewidth is fixed for all transitions and orientations. This procedure is appropriate for light atom singlet fission molecules with EPR spectra in the X-band field range.

The quintet EPR intensities are proportional to the polarization and transition dipole matrix elements $I(B_0) = (p_M - p_{M+1})\delta(\epsilon_M - \epsilon_{M+1})|\langle^5\text{TT}_M|\boldsymbol{\mu}|^5\text{TT}_{M+1}\rangle|^2$, where S is the total spin, $\boldsymbol{\mu} \propto S_x^2$ is the transition dipole operator, and p_M is the population of level M . The population of a ${}^5\text{TT}_M$ level is expected to be proportional to the probability of observing the system in that level after ${}^1\text{TT}$ is populated by singlet fission. It is given by the coupling matrix element squared, $p_M \sim |\langle {}^1\text{TT}|V|^5\text{TT}_M\rangle|^2$.

For a disordered system, spectra are calculated for a uniform distribution of orientations that are distributed over a hemisphere where $\theta \in [0, 90]$ degree and $\phi \in [0, 360]$ degree. Each spectrum is weighted by a geometrical factor w before summing to give the

powder spectrum. Note that the spectra are not normalized at each orientation so that, for example, for parallel chromophores (Fig. 2.3), the two peaks in the $B_0 \parallel z$ spectrum are about two times more intense than the four peaks in the $B_0 \parallel x$ spectrum, because there is intensity borrowing to the additional transitions.

Algorithm 1: Compute diabatic spectrum

Input: $g, B_1, J, D, E, X, \Omega, \{\phi, \theta, w\}, B_0$

Output: RES, INT

```

1 Compute all interaction tensors  $\mathbf{O}_q^k$                                 // Eq. 3.77
2 Compute all spin tensor operators  $\mathbf{T}_q^k$                             // Eq. 3.78
3 Compute rotated intra-chromophore interaction tensors                  // Eq. 3.83
4 Compute rank-0 hamiltonian                                         // Eq. 3.76
5 Calculate the dipole moment matrix
6 Project out quintet elements of dipole moment matrix and store in  $\mu_Q$ 
7 for  $i$  in  $\{\phi, \theta, w\}$  do
8   Compute all rotated interaction tensors for the  $i$ -th set of  $\{\phi, \theta\}$  // Eq. 3.81
9   Compute rank-2 hamiltonians                                         // Eq. 3.76
10  for  $j$  in  $B_0$  do
11    Compute Zeeman hamiltonian for  $j$ -th value of  $B_0$                       // Eq. 3.124
12    Store the sum of all hamiltonians in  $\mathbf{H}$ 
13    Project out quintet block of  $\mathbf{H}$  and store in  $\mathbf{H}_Q$                    // Fig. 3.5
14    for  $m = 1-4$  do
15      Store absolute difference between  $m$ -th and  $m + 1$ -th diagonal elements of  $\mathbf{H}_Q$  in row
16       $m$  and column  $j$  of  $\Delta EN$ 
17      Store difference between the squared  $m$ -th and squared  $m + 1$ -th elements of the first
18      row of  $\mathbf{H}_Q$  in row  $m$  and column  $j$  of  $\Delta P$ 
19  for  $m=1-4$  do
20    Set the element of column  $i$  and row  $m$  of  $RES$  to the minimum of the absolute difference
21    between the  $m$ -th row of  $\Delta EN$  and  $g\mu_B B_1$ 
22    Save the index of the minimum to  $IDX$ 
23    Set the element of column  $i$  and row  $m$  of  $INT$  to the value from the  $IDX$ -th column and
24     $m$ -th row of  $\Delta P$ 
25  Multiply  $i$ -th column of  $INT$  by  $i$ -th element of  $w$ 
26  for  $m=1-4$  do
27    Multiply  $m$ -th row of  $INT$  by the squared matrix element from the  $m$ -th row and  $m + 1$ -th
28    column of  $\mu_Q$ 

```

3.4.4 Best-fit Parameters by Simulated Annealing

Best-fit parameters provide an approximation to the global minimum of the least squares residual, $\chi^2 = 1/N \sum_i^N (S_{i,\text{Exp}} - S_{i,\text{Theory}}/\sigma_i)^2$, where S_{Theory} is the spectrum calculated at the same N field points as the experimental data, S_{Exp} . The error in the intensity at each field point, σ_i , can be estimated by jackknifing the average of consecutively acquired data sets. A minimal set of parameters are fit, and the resampling methods, such as jackknifing, are used to consider parameter correlation.

The SAMIN algorithm from the Optim.jl Julia package⁵⁵ was implemented to minimize the objective function, χ^2 . First, the algorithm stores the initial value of the objective function from a user-given set of initial parameters. The initial values are chosen at random from a bounded parameter space that is system-dependent and chosen to be experimentally relevant but non-restrictive. The initial value for the “temperature” parameter is chosen so that the entire parameter space is accessible.

Once the initial temperature is determined, the algorithm takes N_S (20) steps through the n floated parameters.⁵⁶ On each iteration i , a trial value for parameter p is chosen at random, $p_i = p_0 + rv$, where r is a uniformly distributed random number from $[-1, 1]$, p_0 is the current best value of the parameter and v is the step length for the parameter. If the trial parameter lowers the value of χ^2 , it is accepted. If χ^2 increases, however, the trial parameter may still be accepted if the probability $\exp(-(\chi_{\text{trial}}^2 - \chi_{\text{current best}}^2)/T)$ is greater than a uniformly distributed random number in $[0, 1]$. After $N_S \cdot n$ total steps, the step length v for each parameter is adjusted. If more than 50% of all moves are accepted for a parameter, v is increased so that, for the given temperature, more moves are rejected in following iterations. After N_T (10) bound adjustments, the system is cooled via

$T' = r_T \cdot T$, where r_T (0.85) is the user defined cooling rate. Lowering the temperature decreases the probability of accepting trial parameters that increase the objective function. The temperature continues to cool as the system “anneals” to the correct answer, defined by the objective function tolerance (10^{-3}) and the parameter tolerance (10^{-2}). The implemented values for all optimization parameters (in parenthesis) were tuned until the minima for 50 randomly initialized runs of the SAMIN algorithm converged.

Chapter 4

Entangled, Spin-polarized Excitons from Singlet Fission in a Rigid Dimer*

4.1 Abstract

Singlet fission, a process that splits a singlet exciton into a biexciton, has promise in quantum information (Chapter 1). We report time-resolved electron paramagnetic resonance measurements on a molecule, TIPS-BP1', designed to exhibit strongly state-selective relaxation to specific magnetic spin sublevels. The resulting optically pumped “spin polarization” is a nearly pure initial state from the ensemble. The long-lived spin coherences modulate the signal intrinsically, allowing a new measurement scheme that substantially removes noise and uncertainty in the magnetic resonance spectra. A nonadiabatic transition theory with a minimal number of spectroscopic parameters allows the quantitative assignment and interpretation of the spectra (Chapter 2). The rigid, covalently bound dimer, TIPS-BP1', supports persistent spin coherences at temperatures far higher than those used in conventional quantum hardware.

*Adapted with permission from: Smyser, K. E., Dill, R. D., Rugg, B. K., Damrauer, N. H. & Eaves, J. D. Entangled, Spin-polarized Excitons from Singlet Fission in a Rigid Dimer, (In Review, 2022). R.D.D. and B.K.R. performed the measurements and K.E.S. implemented the theory of K.E.S and J.D.E. Authors N.H.D and J.D.E. advised on all efforts.

4.2 Entangled, Spin-polarized Excitons from Singlet Fission in a Rigid Dimer

Quantum information promises advances in science and computing not seen since the revolutions in classical computing that have unfolded over the last 80 years.¹ But unlike classical computing, where the solid-state transistor has become ubiquitous, we remain in the discovery phase for quantum materials. Quantum logic uses fragile non-equilibrium quantum states built upon qubits that irreversibly decay to Boltzmann equilibrium. In strong-field experiments, microwave or radio frequencies manipulate the qubits to perform operations.⁵ Because the resonant frequencies are much smaller than the thermal energy at room temperature, without extreme cooling or other means of control, a significant population in the excited state generates thermal uncertainty in the initial state of the wavefunction.² This “tyranny of temperature” makes quantum circuits classical for temperatures above a few kelvin (Section 1.1).

Removing the uncertainty in the initial condition of the wavefunction solves the so-called “state-initialization problem,” a requirement for quantum computation that DiVincenzo articulated more than twenty years ago.¹ For example, in color centers, like nitrogen-vacancy centers in diamond, a weak-field optical excitation initializes the system into a non-equilibrium state—a magnetic sublevel—where strong-field magnetic resonance pulses perform gate operations.⁵⁷ But controlling the placement of defects in crystals is challenging, which makes scaling the number of qubits in these materials a formidable hurdle. Recent molecular analogs to the color centers suggest that a bottom-up approach from synthetic chemistry might ultimately lead to more scalable architectures.⁵⁸ Like many other quantum materials, however, the molecules only exhibit

quantum function near liquid helium temperatures.

Chapter 2 predicted that at long times, paired excitons in crystals may hop to neighboring sites and become increasingly more distant. In the limit that the distance between excitons becomes large, the inter-chromophore exchange interaction that splits spin states, J , goes to zero while the single-chromophore interaction that couples the states, D , is unaffected. Models derived from Merrifield's theory for triplet-triplet annihilation^{15,17,19,59,60} and from Redfield theories⁶¹ are a good choice for modeling the pair states when J is small ($|J| \ll |D|$). They can describe the triplet pair EPR spectrum from densely packed dimers or dimers of weakly coupled chromophores, for example, from crystals or floppy molecular dimers with large linkers. For dimers with weak J , the full EPR spectrum is typically from both paired and uncoupled triplets.^{15,17,60}

In Chapter 2, I developed the *JDE* model, a model Hamiltonian and nonadiabatic transition theory for dimers with strong J ($|J| \gg |D|$). It predicted that the conditions for a fast, nonadiabatic transition to a pure state are satisfied when J is the largest energy in the hamiltonian and when fluctuations in J are on the order of the pair state energy splittings. Chapter 2 suggests that highly ordered and dilute systems can produce a strongly spin-polarized quintet pair state 5TT , which is observed when the singlet state 1TT transfers into specific quintet sublevels 5TT_M with high fidelity. Chapter 4 now reports on the EPR spectrum from a dilute glass of molecular dimers, TIPS-BP1'. Importantly for quantum computing applications, all $S = 1$ photoproducts are undetectable in its EPR spectrum—it is entirely from the quintet state—and electron spin coherence remains for microseconds. Because the chromophores are covalently bound and because diffusion is inhibited, we expect that J is large. By replicating the observed spectrum with the *JDE* model, using only three adjustable parameters we confirm this assumption. Moreover, because the

spectrum from the glassy sample contains information on all single-dimer spectra—for all orientations—we break it down into components from single orientations and show how state-selectivity is achievable for an oriented sample of TIPS-BP1'. To generate intense spin polarization, our results show that it is sufficient for chromophores to share a single molecular axis as long as their relative orientation is fixed—they need not be entirely parallel, as predicted in Chapter 2.

The several possible biexciton species $^{2S+1}\text{TT}_M$ that differ in their overall spin S and degree of entanglement are not directly distinguished by transient absorption spectroscopy,³⁵ so we turn to trEPR to resolve them. The experiment starts the SF process with an optical pulse and then uses EPR to monitor the time-evolution of the products. TrEPR signatures of TIPS-BP1' in mTHF glass (75 K, 640 nm pump wavelength) emerge over a few hundred nanoseconds following photoexcitation (Fig. 4.1a). This timescale is consistent with the decay of ^1TT and is impulsive on the timescale of the trEPR measurement (10 μs).³⁵ Four sharp features, from 338–359 mT, dominate the trEPR spectra for all observable times. They form concomitantly and exhibit underdamped Rabi oscillations that beat at the nutation frequency (Fig. 4.1a, inset). These oscillations have not been reported in trEPR data for any system undergoing SF but have been observed for triplets where relaxation processes are slow.⁶²

General trEPR trends in the SF literature include broad and congested spectra, with substantial interconversion between EPR-active states.^{14–17,20,22,63} By contrast, our spectra—aside from the oscillations—do not show substantial time evolution. They are also highly structured and symmetrical. The EPR spectra in Fig. 4.1a are narrow, with intensity spanning 20 mT. The intersystem crossing triplet spectrum for the monomer TIPS-Pc, in comparison, spans 84 mT (Fig. 4.2). The relatively narrow width of the

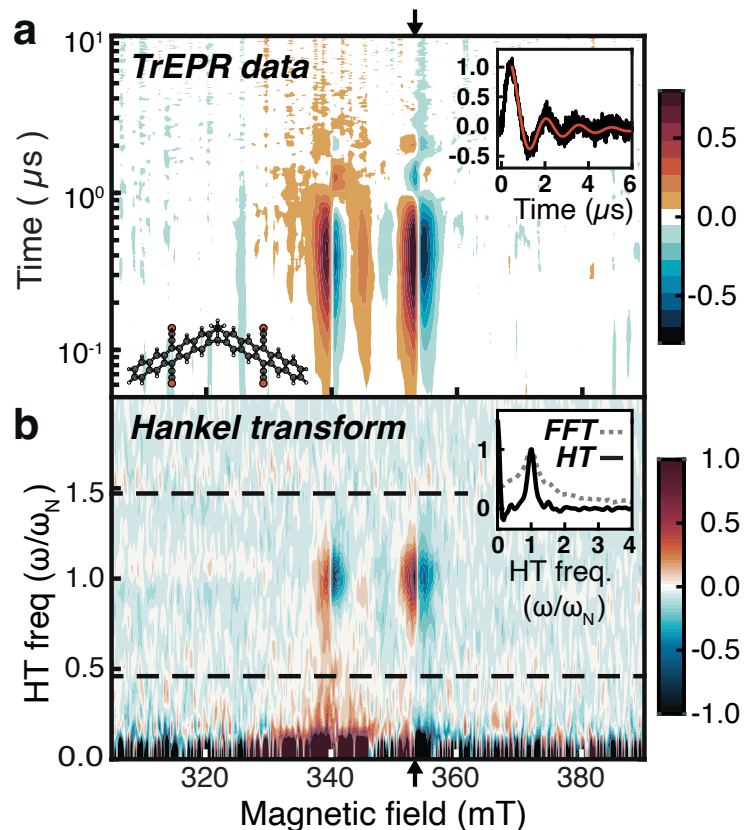


FIGURE 4.1: TrEPR data for TIPS-BP1' demonstrates long spin-coherence times and strong spin polarization. **(a)**, Contour plot of X-band trEPR data for TIPS-BP1' (75 K and 640 nm excitation). Inset: Underdamped Rabi oscillations for a representative magnetic field value (353.4 mT, arrows). The signal decay (black line) fits well to a damped Bessel function (red line), which is expected for an orientationally distributed sample. The fit gives an estimate for the coherence time, $T_2 \approx 1.4 \mu\text{s}$. **(b)**, The Hankel Transform (HT) then provides the nutation spectrum at each field point. Inset: HT of the transient shown in the inset of (a) peaks much more sharply than the comparable amplitude spectrum from the Fast Fourier Transform (FFT). This resolution enhancement facilitates extraction of the “Hankel spectrum” in Fig. 4.3b, which corresponds to ${}^5\text{TT}_0 \leftrightarrow {}^5\text{TT}_{\pm 1}$ transitions.

TIPS-BP1' spectra suggests that the signal originates from ${}^5\text{TT}$.⁴⁶

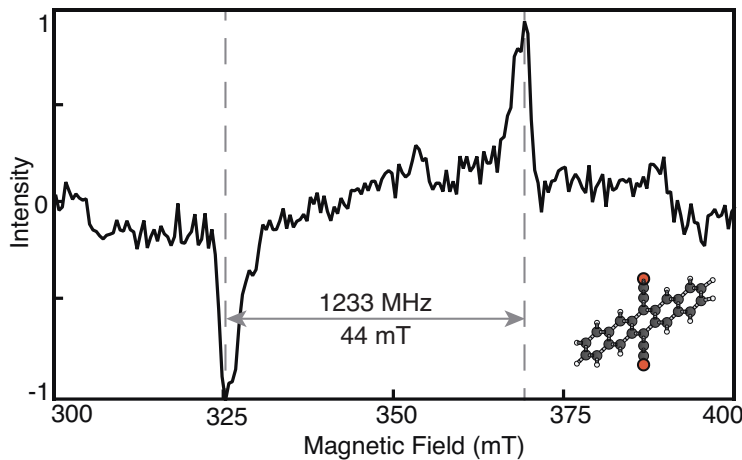


FIGURE 4.2: The intersystem crossing triplet EPR spectrum of TIPS-Pc monomers in a heavy atom solvent (4:1 toluene:1-iodobutane, 640 nm excitation, 100 K, $f_{\text{microwave}} = 9.74729$ GHz). Because this is a triplet, the splitting between the peaks (dotted grey lines) gives the value of D directly. The measured value of D (1233 MHz), assuming $E = 0$, is similar to the extracted value of D for the TIPS-BP1' dimer (1322 MHz). The data is an average of scans in the time domain over 101–301 ns, where the signal remained relatively constant. The spectrum appears to be contaminated near 350 mT. We attribute this contamination to the presence of ${}^5\text{TT}$ in aggregated monomers,⁶⁴ because a similar sample with higher TIPS-Pc concentration (not shown) indicated much stronger features in this field range.

Nutation frequencies depend on S and M , so they can, in principle, inform on the spin species and sublevels produced after SF.⁶⁵ In the SF literature, they are commonly determined with pulsed EPR at only a few values of the static magnetic field, B_0 .^{14–17,20,22} Compared to pulsed nutation experiments, trEPR has a dramatic multiplex advantage—an entire time trace is collected simultaneously (Fig. 4.1). However, pulsed techniques with high microwave powers are necessary for most SF systems since rapid dephasing and population transfer overdamp the low-frequency nutation oscillations in trEPR.⁶⁶ In TIPS-BP1', by contrast, the presence of Rabi oscillations at a dominant frequency in

the trEPR data implies that there is a state-selective population formed rapidly on the timescale of the oscillation period.

Although Rabi oscillations within a two-level quantum system decay as a damped harmonic oscillator, the measured trEPR nutation signal for an inhomogeneously broadened system does not—it decays as a Bessel function. In such systems, including disordered samples like ours, the measured signal contains contributions from many spins with a distribution of resonant frequencies. Integrating over the distribution of resonant frequencies leads to the approximate result $s(t) \propto J_0(\omega_N t)e^{-t/2T_2}$, valid for strongly underdamped Rabi oscillations that begin suddenly.^{62,67,68} $s(t)$ is the time-domain signal for a fixed value of B_0 , J_0 is a zeroth order Bessel function, ω_N is the observed nutation frequency, and T_2 is the transverse relaxation time (strictly true for a two-level system), or coherence time.

Because the nutation signal is described by a Bessel function, the Hankel transform, which projects the time-domain signal onto the Bessel functions, substantially enhances frequency resolution relative to the Fourier transform (Fig. 4.1b, inset). Our method shares many similarities with lock-in detection, but rather than externally modulating the signal, the method “locks in” at the sharply peaked dominant nutation frequency ω_N to separate low-frequency components from the oscillating signal (Fig. 4.1b). The “Hankel spectrum” is the integrated intensity along the frequency axis within a prescribed bandwidth (Fig. 4.1b). It isolates the signal that nutates at ω_N —the majority component of the EPR data (Fig. 4.3, black lines).

Recognizing the Bessel function shape of the trEPR data at fixed B_0 , we also use the oscillatory decay to estimate the decoherence time, $T_2 \approx 1.4 \mu\text{s}$ (Fig. 4.1a, inset). Notably,

there are two recent works in the literature that use singlet fission in the pursuit of quantum information applications, but with chromophores in crystals that are oriented in the field, not dimers (Chapter 5).⁶⁰ The value of T_2 for TIPS-BP1' dimers reported here at 75 K is similar to that reported in Ref. [60] for a single-crystal tetracene-derivative at 10 K. Even in a glassy phase, T_2 for TIPS-BP1' is at least five times longer than it is in the crystalline samples of Ref. [60] at similar temperatures.

A signal oscillating at a dominant nutation frequency might result from a state-selective relaxation process, from ^1TT into a few specific $^5\text{TT}_M$ sublevels, and such precise state-selectivity can solve the state-initialization problem in quantum information. But to determine the extent of state-selectivity in a molecule, an accurate interpretation of the EPR spectrum is essential. Some have adapted Merrifield's theory⁵⁹ for triplet-triplet annihilation, to compute the TT populations that the EPR experiment probes (see Appendix B).^{15,17,19,60} Therein, when the inter-chromophore exchange interaction J is zero the resulting spectrum only comes from $M = 0 \rightarrow M = \pm 1$ transitions, so we refer to it as the " Q_0 " model. But the Q_0 model is inappropriate for strongly coupled dimers that directly populate ^5TT , from ^1TT , so it does not reproduce the spectrum of TIPS-BP1' (Fig. 4.3a). Without a theory to determine the populations, they become fitting parameters.¹⁶ In the dense and broad spectra typical of EPR data for SF, these additional parameters lead to uncertainty and overfitting that complicates the interpretation of the spectra.

To overcome this problem, we compute the populations of the initial ^5TT sublevels with our nonadiabatic transition theory by extending the theory reported in Chapter 2 to model non-parallel chromophores and to compute spectra for dimers in the glass phase. Like in Chapter 2, we assume that J , the Dirac-Heisenberg coupling between triplets on

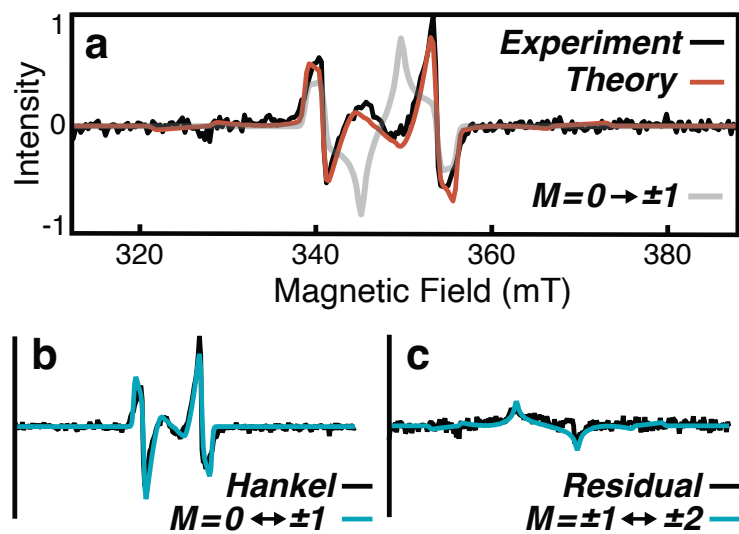


FIGURE 4.3: Data and calculated EPR spectrum for TIPS-BP1'. **(a)**, The prompt trEPR spectrum for TIPS-BP1' (black) is an average over 200–400 ns (Fig. 4.1a). The red line comes from the *JDE* model with best-fit parameters $D = 1322 \pm 3$ MHz, $X = 59 \pm 1$ MHz, and $\beta = 111.1 \pm 0.2^\circ$ (see Chapter 3). Using the Q_0 model to predict initial populations (gray) does not reproduce the spectrum. **(b)**, The Hankel spectrum (black) is the dominant signal and is replicated well by a calculated ${}^5\text{TT}_0 \leftrightarrow {}^5\text{TT}_{\pm 1}$ spectrum (blue, *JDE* model). **(c)**, The residual spectrum (black) is the difference between the full spectrum in (a) and the Hankel component in (b). It is reproduced (blue, *JDE* model) with a calculated ${}^5\text{TT}_{\pm 1} \leftrightarrow {}^5\text{TT}_{\pm 2}$ spectrum. Any signal from triplets is undetectable. Relative amplitudes of the calculated spectra (blue) come from the *JDE* model.

adjacent chromophores A and B of the same molecule, is the largest energy scale of the matter hamiltonian and choose the quantization axis to lie along the Zeeman field in the lab frame. This choice diagonalizes the Zeeman hamiltonian and the rotationally invariant, or isotropic, part of the JDE hamiltonian for all orientations of the molecule, $g\mu_B B_0 S_z + J\vec{S}_A \cdot \vec{S}_B$, in the basis of total spin Zeeman states $|S, M\rangle$. The remaining “zero-field hamiltonian” is anisotropic—it depends on a molecule’s orientation relative to the quantization axis. After employing rotation operators, the Wigner-Eckhart theorem, and other simplifications, the zero-field hamiltonian becomes a function of three parameters: the axial intra-chromophore interaction, D , the anisotropic inter-chromophore interaction, X , and the angle between the chromophores, β (Fig. 4.5b, Chapter 3). A projection operator, P , partitions the hamiltonian into the reference hamiltonian, $H_0 \equiv PHP$, that is block-diagonal in total spin S , and the perturbation that involves only the anisotropic zero-field hamiltonian $V = H - H_0$.

After this partitioning, the Zeeman term lies on the diagonal of H_0 and splits states of different M . The exchange interaction J produces diagonal terms that split states with variations in total spin S . We assume that nuclear motions modulate the distance between chromophores to make the value of J time dependent, $J = \langle J \rangle + \delta J(t)$. Fluctuations in J modulate the energy gaps between diagonal states of different S , bringing them into transient resonances that allow transitions between them. After including the fluctuations on the diagonal by introducing a linear response system-bath hamiltonian and applying perturbation theory in V for the transition rates between states $|\mu\rangle$ and $|\nu\rangle$ of H_0 , the expression for the rate is analogous to the nonadiabatic Marcus theory, $k_{\mu \rightarrow \nu} \propto |\langle \mu | V | \nu \rangle|^2 F_{\mu, \nu}$, where $F_{\mu, \nu}$ is a temperature-dependent nuclear factor that depends on the statistics of the fluctuations. But, because the energy levels of H_0 are split by energies much smaller

than $k_B T$, the state populations are approximately independent of the statistics for the fluctuations in J and thereby independent of $F_{\mu,\nu}$. In this theory and under the stated assumptions, the tunneling matrix element $|\langle {}^1\text{TT}|V|\nu\rangle|^2$ gives the sublevel population of the initial state in the trEPR experiment $|\nu\rangle$ from $|{}^1\text{TT}\rangle$.

In the chosen representation, H_0 is block-diagonal in S , but there is weak mixing between states of different M within an S block. One can either ignore the mixing or diagonalize the block, redefining both the states and the transition matrix elements. These two choices correspond to a diabatic basis or an adiabatic one for $|\nu\rangle$, respectively. Unlike the adiabatic states, the diabatic (Zeeman) states are well-defined in the lab frame and independent of orientation (see Section 3.4.1). The diabatic states facilitate assignment of the trEPR spectrum (Figs. 4.3b, 4.3c) but the adiabatic states (Fig. 4.3a) give a more accurate reproduction of it. Because the applied Zeeman field is much larger than the zero-field interactions, the mixing between the ${}^5\text{TT}_M$ sublevels is weak, and there are only small, quantitative differences between the spectra calculated with the diabatic and adiabatic bases (Fig. 4.4).

To fit spectra, we compute the ensemble-averaged trEPR spectrum directly in the adiabatic basis, use discretization to calculate and sample over molecular orientations, and use simulated annealing to determine best fit parameters. For each orientation in the fitting protocol, the initial states of the trEPR spectra come from the nonadiabatic transition theory. These simplifications are substantial. The computed trEPR spectra only depend on the parameters D , X and β . Including X is essential but the orthorhombicity parameter E is not included because it does not significantly improve fit results for either the dimer or the monomer. Section 3.4 contain the details of the theory and the fitting procedure.

Figure 4.3a shows the prompt EPR spectrum—the spectrum immediately following

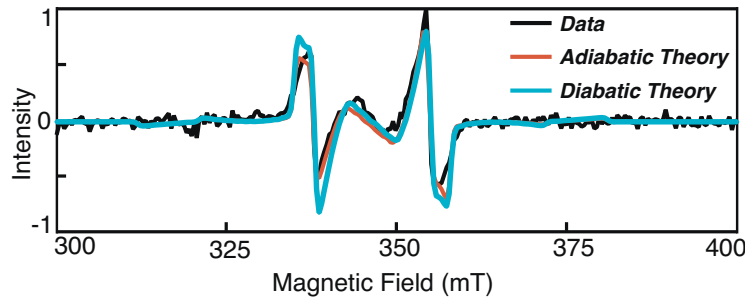


FIGURE 4.4: The ${}^5\text{TT}$ spectrum calculated with the *JDE* model in the diabatic $|S, M\rangle$ basis (blue) is a good fit to the early time trEPR data (black). The calculated spectra and data in Figs. 2b and 2c sum to give the blue and black lines here, respectively. The diabatic spectrum is symmetric with respect to center field.

SF—for TIPS-BP1' (200–400 ns, Fig. 4.1a) along with a calculation of it. The best-fit values $D = 1322 \pm 3$ MHz and $X = 59 \pm 1$ MHz are consistent with those for pentacene derivatives and dimers, respectively.¹⁴ The fit value of $\beta = 111.1 \pm 0.2^\circ$ is within 0.2% of the calculated value from DFT simulations for the quintet in a model of TIPS-BP1' (110.9° , unrestricted- ω -B97XD/6-31G(d)).

With the optimal set of spectroscopic parameters determined, the calculated EPR spectrum breaks down into two components from the diabatic ${}^5\text{TT}_M \leftrightarrow {}^5\text{TT}_{M\pm 1}$ transitions. Figures 4.3b and 4.3c show the results. Our theory demonstrates that the Hankel transform isolates the signal from the ${}^5\text{TT}_0 \leftrightarrow {}^5\text{TT}_{\pm 1}$ transitions (Fig. 4.3b), and supports the assignment of the nutation frequency to this component. The residual spectrum (Fig. 4.3c), the difference between the Hankel spectrum (Fig. 4.3b) and the total spectrum (Fig. 4.3a), agrees with the computed ${}^5\text{TT}_{\pm 1} \leftrightarrow {}^5\text{TT}_{\pm 2}$ spectral component quantitatively, in both amplitude and functional form.

It is only by accounting for the orientational dependence of the sublevel populations that we recover the spectrum from TIPS-BP1'. Figure 4.5a shows that the most intense features in the powder spectra are from transitions where the Zeeman field aligns with the dimer axes (Fig. 4.5b and 4.5c). Figure 4.5a also shows that while the $^5\text{TT}_0$ sublevel population is large for $\vec{B}_0 \parallel z$ and $\vec{B}_0 \parallel y$, it is *zero* for $\vec{B}_0 \parallel x$. In the Q_0 model, by contrast, the $^5\text{TT}_0$ sublevel is the only TT sublevel populated for any orientation—including $\vec{B}_0 \parallel x$ —leading to an over-representation of the $^5\text{TT}_0 \rightarrow ^5\text{TT}_{\pm 1}$ transitions in the spectrum, and a poor resulting fit (Fig. 4.3a, gray). Indeed, if the $^5\text{TT}_0$ level were the only sublevel populated, the residual spectrum would be zero.

To engineer a piece of quantum hardware based on our system and observations, one would have to immobilize and align the molecules so that they all have a definite orientation with respect to the Zeeman field. Figures 4.5d and 4.5e show the predicted spin polarization for a system of aligned TIPS-BP1' dimers. Borrowing an idea from Shannon's classical information theory,⁶⁹ we introduce the order parameter \mathcal{I} to quantify the spin polarization achievable into *any* $^5\text{TT}_M$ sublevel from ^1TT as a function of molecular orientation relative to the field (Fig. 4.5c), where $\mathcal{I} = 1 + \frac{1}{\log_2(5)} \sum_{M=-2}^{+2} p_M \log_2 p_M$ (Fig. 4.5d). Like Shannon's information measure, \mathcal{I} is zero when all $^5\text{TT}_M$ are equally populated and unity when only one level is occupied. Our work in Chapter 2 recommends that the chromophores share a common set of axes. While the x and z -axes of the chromophores are not parallel for TIPS-BP1', the y -axes *are*. As a result, the most intense spin polarization occurs when the Zeeman field aligns with the shared y -axis.⁷⁰ The corresponding north and south poles of Fig. 4.5d exhibit the largest spin polarization, and Fig. 4.5e shows that the $^5\text{TT}_0$ sublevel is the one that gets polarized.

In molecular systems like those pioneered in nuclear spin resonance computing,

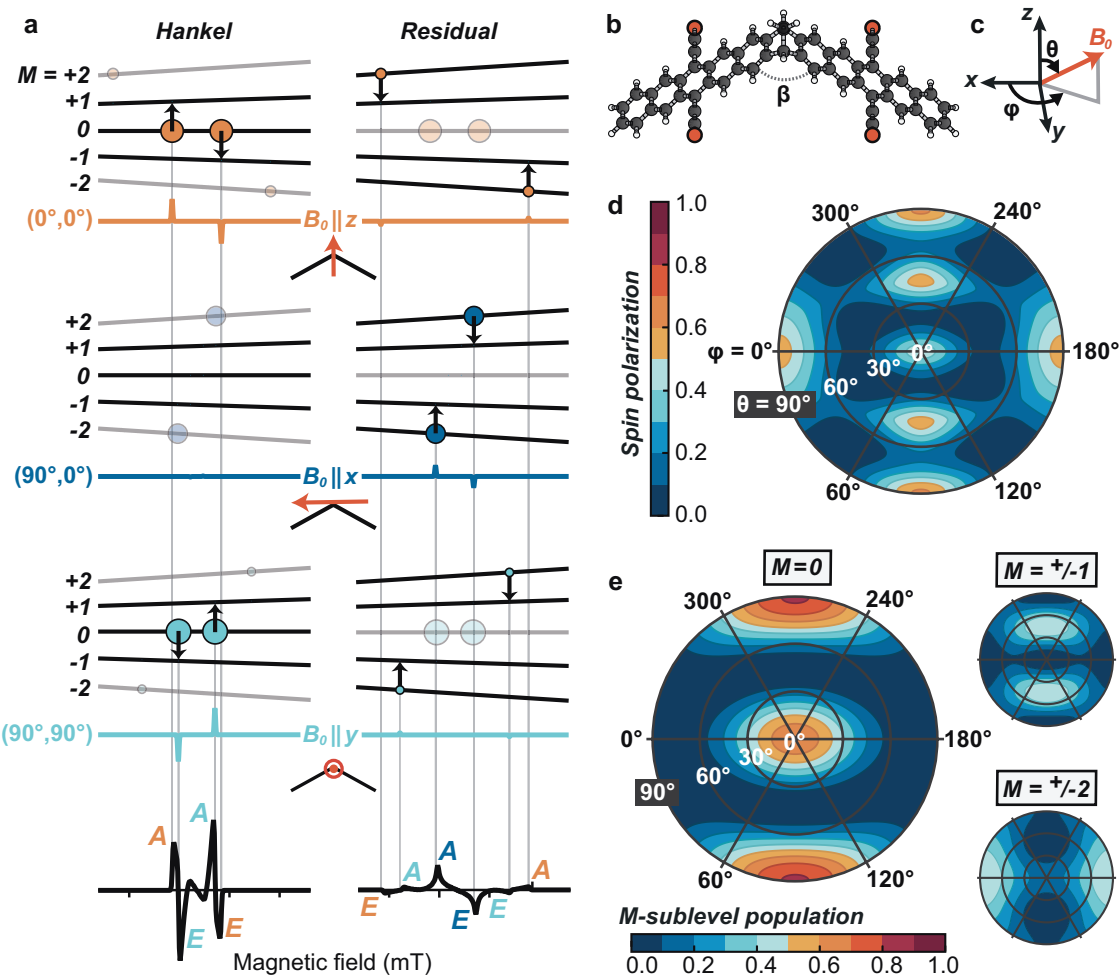


FIGURE 4.5: Theory predicts strong spin polarization for the rigid TIPS-BP1' dimer. (a), Fixed-orientation EPR spectra (colored lines) for \vec{B}_0 (red arrows) applied along cardinal dimer directions. Predictions for the Hankel spectrum (${}^5\text{TT}_0 \leftrightarrow {}^5\text{TT}_{\pm 1}$) on left and residual spectrum (${}^5\text{TT}_{\pm 1} \leftrightarrow {}^5\text{TT}_{\pm 2}$) on right. Area of colored circles indicates ${}^5\text{TT}_M$ -sublevel populations, and arrows show the direction of transitions (A absorption or E emission). Vertical lines correlate population assignments with features in the simulated powder spectra (black, below). (b), The two chromophores in the TIPS-BP1' dimer are rigidly linked so that a single bridging angle β defines the chromophore-chromophore orientation. (c), The polar and azimuthal angles θ and ϕ for the Zeeman field relative to the dimer cardinal axes. (d), Spin polarization $\mathcal{I} = 1 + \frac{1}{\log_2(5)} \sum_{M=-2}^{+2} p_M \log_2 p_M$ for an ordered sample as a function of the dimer-field orientation. This range of (θ, ϕ) considers all orientations with unique spectra. (e), ${}^5\text{TT}_M$ populations as a function of the dimer-field orientation. The $\pm M$ -sublevels are predicted to be equally populated. The maximum population of ${}^5\text{TT}_0$ occurs at $\vec{B}_0 \parallel y$, $(\theta, \phi) = (90^\circ, 90^\circ)$.

scaling the number of coherent qubits is relatively straightforward.⁵ But the state-initialization problem has bedeviled that field.² TIPS-BP1' is an example of a novel class of compounds that create entanglements between *electron* spin states that remain coherent on timescales that are orders of magnitude longer ($\approx 1 \mu\text{s}$) than the switching time for a gate operation ($\approx 1 \text{ ns}$), even in a powder spectrum. The quintet state, born under the selection rules of singlet fission, is a two-triplet spin-coherent excitation. The coherence entangles the triplets and increases the number of computational states from three to five—an elementary demonstration of scaling. Our results motivate efforts to orient TIPS-BP1', and molecules like it, through crystallization or other means. SF in rigid molecular dimers solves the state initialization problem at temperatures far higher than the operating temperatures in contemporary quantum hardware.

Chapter 5

Triplet-Pair Spin Signatures from Macroscopically Aligned Heteroacenes in an Oriented Single Crystal*

5.1 Abstract

In Chapter 2, the *JDE* model determined that the ${}^5\text{TT}_0$ sublevel can be selectively populated if certain conditions are met. Among the most challenging, the molecules within the dimer undergoing singlet fission must have their principal magnetic axes parallel to one another and to an applied Zeeman field. Chapter 5 presents time-resolved paramagnetic resonance spectroscopy of a single crystal sample of a novel tetracenethiophene compound featuring arrays of dimers aligned in this manner, mounted so that the orientation of the field relative to the molecular axes could be controlled. The observed spin sublevel populations for the paired TT and unpaired T + T triplets are consistent with predictions from the *JDE* model, including preferential ${}^5\text{TT}_0$ formation at $z \parallel B_0$, with

*Adapted with permission from: Rugg, B. K., Smyser, K. E., Fluegel, B., Chang, C. H., Thorley, K. J., Parkin, S., Anthony, J. E., Eaves, J. D. & Johnson, J. C. Triplet-Pair Spin Signatures from Macroscopically Aligned Heteroacenes in an Oriented Single Crystal. *PNAS* **29**, 119, (2022). B.K.R prepared samples and performed trEPR measurements and analysis, under advisement of J.C.J. B.F. performed magnetoluminescence experiments. K.J.T. synthesized TES TIPS-TT, under advisement of J.E.A. S.P. characterized and indexed single crystals. K.E.S. and J.D.E developed theoretical methods and performed trEPR simulations.

one caveat—the two ${}^5\text{TT}_{+M}$ spin sublevels have little to no population.

5.2 Introduction

In Chapter 2 I derived the *JDE* model based on nonadiabatic transition theory (NTT) for dimers whose molecules share principal axis directions. In the model, the effective J is large enough to separate the ${}^{2S+1}\text{TT}$ states, but, immediately following singlet fission, large fluctuations in J induce crossings between the various ${}^{2S+1}\text{TT}_M$ sublevels to facilitate relaxation events. The subsequent sublevel population is dictated by the orientation of the molecular z -axis relative to an applied magnetic field (\vec{B}_0 , Fig. 5.1a). Importantly, for quantum information applications, the ${}^5\text{TT}_0$ sublevel is dominant for $z \parallel \vec{B}_0$ and there is evidence that it is addressable with microwave pulses and has the potential for optical readout.^{58,71,72} This Chapter expands the model to include exciton unbinding dynamics that can occur in crystals with mobile excitons and find that the separated triplets T + T maintain the spin polarization of the initially formed sublevels.

Motivated by the predictions of the parallel *JDE* model, we have conducted a time-resolved EPR study of a single crystal of 2-triethylsilyl-5,11-bis(triisopropylsilyl ethynyl) tetraceno[2,3-b]thiophene (TES TIPS-TT), a novel heteroacene with a crystal structure in which all molecules share a common z -axis (Fig. 5.1b). Because all TES TIPS-TT molecules are aligned parallel to one another in the crystal, the angle θ of the molecular z -axis relative to \vec{B}_0 (Fig. 5.1) can be systematically controlled.

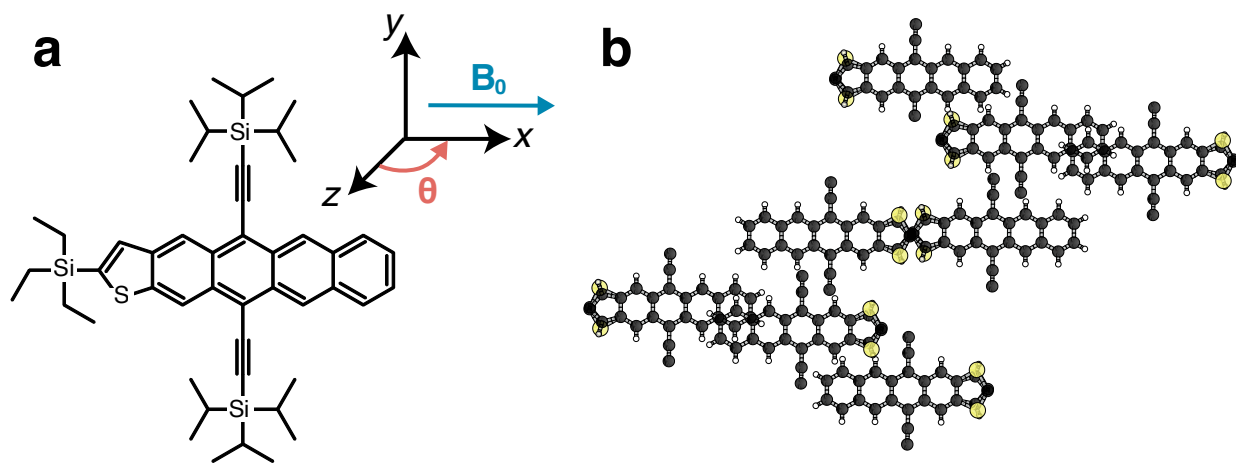


FIGURE 5.1: (a) The primary axis, the z -axis, is perpendicular to the molecular π -system and its orientation relative to an applied magnetic field, \vec{B}_0 , is defined by θ . The illustration shows $\theta = 90^\circ$, or $x \parallel \vec{B}_0$. (b) The crystal structure of TES TIPS-TT. Although all chromophores are parallel in the crystal, there are various pair sites that have different chromophore-chromophore distances and orientations (Fig. 3.2). There is only one sulfur atom per chromophore, however this may be in one of the two positions indicated.

5.3 Theory and Calculations for the EPR Spectra

To model the exciton unbinding process, $TT \rightarrow T + T$, let the J -coupling be binary—it is J when two molecules in the crystal are nearest neighbors and zero otherwise. The hamiltonian takes the form,

$$\mathcal{H} = H_{AB}^{Zeeman} + H_A^{ZFS} + H_B^{ZFS} + f(J\mathbf{S}_A^T \cdot \mathbf{S}_B), \quad (5.1)$$

for chromophores A and B where f is a binary switching function that is either zero or one. While the ${}^1\text{TT}$ state forms on adjacent chromophores,⁷³ the excitons in a crystal are mobile. Once one of the excitons hops to another chromophore, the ${}^{2S+1}\text{TT}$ state can decohere and evolve to separated triplet pairs, $T + T$.

Part of the spectrum comes from the ${}^5\text{TT}_M$ sublevels, whose calculations appear in the

analysis of the parallel *JDE* model in Chapter 2. But in a crystal, some of the triplets in the ensemble will have hopped and unpaired, even at early times. The jump dynamics are assumed to be slow relative to the timescale for quintet formation on neighboring molecules but fast enough to completely dephase the triplet pair states. This is modelled by allowing the quintet state to form for all molecules in the *JDE* hamiltonian, $f = 1$. Some fraction of those molecules in the ensemble will experience a jump between time zero and time t . That sub-ensemble will quench into the unpaired triplet hamiltonian, $f = 0$. I quench those molecules, using the density matrix from the initial quintet states of the *JDE* model, into the states of the unpaired triplet by applying the projection operator $P = \sum_{M_A, M_B} |M_A, M_B\rangle\langle M_A, M_B|$, where the sum over M_A and M_B goes over the sublevels of unpaired states—the eigenstates of the hamiltonian with $f = 0$. The projection operator separates out the diagonal elements of the density matrix in the unpaired basis. The density matrix of the entire system is $\rho = w\rho_0 + (1 - w)P\rho_0P$, where w is an empirical parameter equivalent to the fraction of exciton pairs that have not undergone a jump before the time of measurement, and ρ_0 is the density matrix of the *JDE* model at early times (Chapter 2). Here, it is assumed that the populations decouple from the coherences and that the time evolution of the coherences is fast compared to the populations. Both approximations appear in the Redfield theory of quantum relaxation.⁷⁴ The calculation of the trEPR spectrum follows from the density matrix (Section 3.4).

The single crystal spectra of TES TIPS-TT at select orientations were calculated with the parallel *JDE* model, where both transitions and intensities are calculated from the spin hamiltonian (Eq. 5.1). The computed trEPR spectra at each orientation are sums of two components: one from the ${}^5\text{TT}_M$ sublevels and another from the spin-polarized, unpaired triplets $\text{T} + \text{T}$. First, the calculated spectrum was compared to the data for $z \parallel \vec{B}_0$

to optimize a value of D in the least-squares sense with the simulated annealing technique (Section 3.4.4). At this orientation, E has little to no effect on the spectrum. Fixing D to the resulting best-fit value (1260 MHz), the $x \parallel \vec{B}_0$ spectrum was optimized for E (16 MHz). When optimizing parameters, the hamiltonian is evaluated in the eigenbasis of the quintet subspace, called the adiabatic basis, $|S = 2, \alpha\rangle = \sum_M \alpha_M |S = 2, M\rangle$ (Section 3.4.1). These states are very close to the Zeeman $|S = 2, M\rangle$ states *away from crossings*.⁷⁰ Although the energies of the Zeeman states change upon sample rotation, the states remain well defined. The ${}^5\text{TT}$ and T + T populations were calculated using the parallel *JDE* model, but to replicate the data, populations of the two high energy quintet states ($M = +1, +2$) were set to zero. The four ${}^5\text{TT}$ and two T + T lines ($\Delta M = \pm 1$) at each orientation are broadened by Lorentzian lineshapes. Line intensities are proportional to the difference in population between the $\Delta M = \pm 1$ sublevels and the corresponding dipole matrix element squared. The relative amplitudes of the ${}^5\text{TT}$ and T + T spectra are orientation-dependent and are estimated from the data. Diagrams of the spin sublevel energies and populations (Figs. 5.5-5.8) were likewise calculated, but in the diabatic Zeeman basis where states of S and M are long-lived.

5.4 Magnetophotoluminescence Spectroscopy

Single crystals of TES TIPS-TT exhibit several bands of steady-state fluorescence in the range of 600-800 nm when excited at 520 nm. The yield of the fluorescence within the range of 700-775 nm shows a clear dependence on the strength of an applied magnetic field at low temperatures (Fig. 5.2). Dips in the fluorescence intensity are observed where the non-magnetic ${}^1\text{TT}$ state crosses with the dark ${}^5\text{TT}_M$ sublevels that tune through the

magnetic Zeeman interaction (Fig. 5.3).⁴⁴ The magnitude, though not sign, of J can be determined from the distribution of the dips in the spectrum. The experimental field range (0 - 14 T) allows for detection of J between ≈ 5 and 131 GHz. I assumed that $J > 0$ to generate Fig. 5.2a, but it is equally probable that $J < 0$.

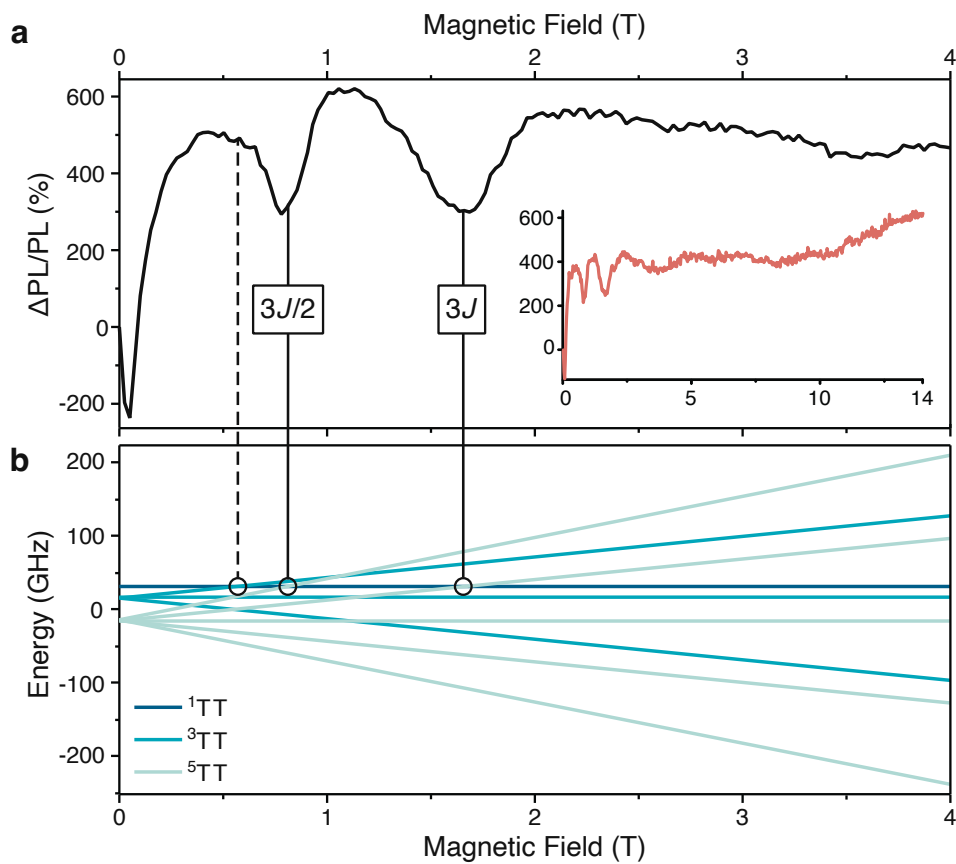


FIGURE 5.2: (a) Changes in relative PL vs. applied magnetic field at 2 K. The full data set is shown as an inset where the units are the same as the main figure. (b) Energy level diagram of an exciton pair with $J = -15.4$ GHz in a magnetic field. Black circles highlight level crossings between ^1TT and $^5\text{TT}_{+1,+2}$ (observed) and with $^3\text{TT}_{+1}$ (not observed).

Two prominent dips in the field sweep appear at 0.83 and 1.65 T. Based on the 1:2 ratio of these values, and assuming $J > 0$, the first and second peaks can be assigned to ^1TT mixing with $^5\text{TT}_{+2}$ and $^5\text{TT}_{+1}$, respectively (Fig. 5.2b). Dips from these crossings occur at

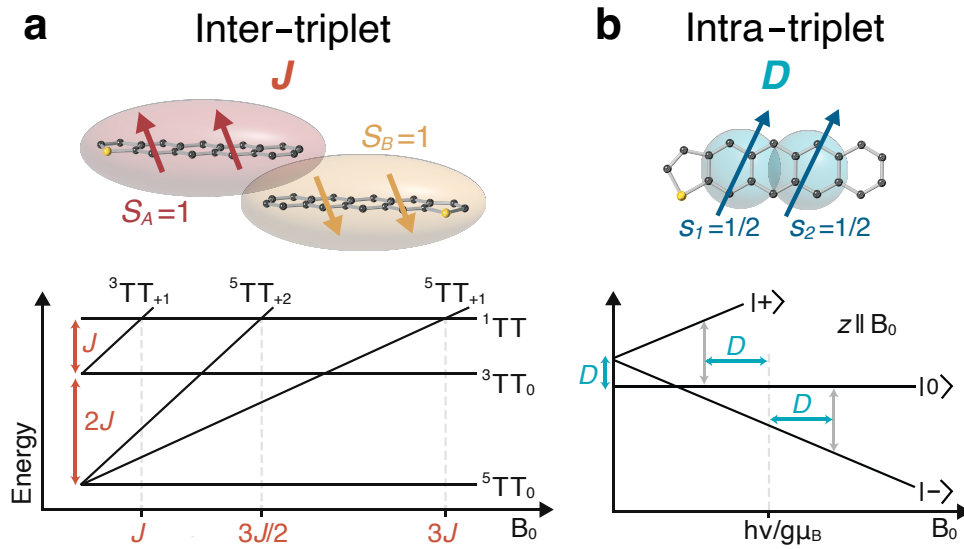


FIGURE 5.3: Schematic and associated energy level diagrams for (a) the inter-triplet interaction J , which dictates energetic splitting between the ^1TT , ^3TT , and ^5TT spin manifolds (depicted for negative J in the diagram) and is dependent on the degree of electronic coupling between triplet excitons. The magnitude of J can be obtained directly by measuring field strengths at which photoluminescence is decreased due to mixing of the emissive ^1TT state with dark ^5TT sublevels. (b) The intra-triplet interaction D , which primarily dictates energetic splitting between magnetic sublevels within $\text{T} + \text{T}$, ^3TT , and ^5TT . Splitting of trEPR transitions due to D is dependent on molecular orientation relative to an applied magnetic field (B_0); the energy level diagram depicts the splitting between the states of an isolated T when the primary molecular axis (z) is parallel to B_0 , for which associated transitions are split by $2D$. Values of D and its associated parameter E (not depicted) are typically obtained from fitting the trEPR powder spectrum of triplets localized on non-interacting monomers.

field strengths of about $1.5J$ and $3J$ (1:2), respectively, so that $|J| = 15.4 \pm 0.3$ GHz for at least one dimer within the TES TIPS-TT crystal structure.

Our results are similar to the MPL from TIPS tetracene,⁷¹ however, three peaks rather than two are observed for TIPS tetracene because there is also a peak at $|J|$. This yields a characteristic 1:3/2:3 splitting pattern. For TES TIPS-TT, no dip is detected at the ^1TT - $^3\text{TT}_{+1}$ curve-crossing field position at J (dashed line, Fig. 5.2a).

In Sections 3.2.8 and 3.3.5, I derived the selection rules that allow ^1TT - ^3TT mixing. To observe the $S = 0$ to $S = 1$ transition, there must be a non-zero rank-1 interaction. Although the rank-1 interactions are small for light-atom singlet fission systems, they can become significant at crossings where the energy splitting goes to zero. The intra-chromophore interactions, in general, are orders of magnitude smaller than the inter-chromophore interactions and, therefore, most likely direct the observed behavior. But the intra-chromophore rank-1 interactions are zero, according to the particle exchange symmetry, when the chromophores are parallel. The observation of only two dips in emission intensity vs. magnetic field provides further evidence of favorable molecular alignment, unlike the lower symmetry TIPS tetracene samples.^{71,72}

The additional prominent feature that occurs at $\vec{B}_0 < 0.1$ T in both TES TIPS-TT and TIPS tetracene is ubiquitous in early magnetic-field dependent experiments⁴⁴ on crystalline acenes. For weakly coupled chromophores ($|J| \ll |D|$), crossings occur at field strengths similar to the zero-field splitting interaction. Its presence here alongside features associated with $|J|=15.4$ GHz affirms that both paired ($f = 1$, Eq. 5.1) and unpaired ($f = 0$) triplets exist in the crystal. The potential for fast TT dissociation rationalizes the detection of both species in time-integrated experiments.

Note that the multitude of possible molecular pairs will lead to other values of J ;

however, these may not be observable in the magneto-photoluminescence experiment for various reasons: triplet-triplet interactions on these pairs may not lead to detectable fluorescence that reflects the ${}^1\text{TT}$ population, or they may be too weak or too strong to be detectable in the magnetic field range of the experiment.

5.5 Electron Paramagnetic Resonance Spectroscopy.

TrEPR spectra obtained from a crystalline powder of TES TIPS-TT at room temperature after $\lambda_{ex} = 610$ nm are shown in Fig. 5.4. The central *EA* feature in the early time 25 – 75 ns spectrum (Fig. 5.4c) spans about center field by about $|D|/3$ and identifies the presence of ${}^5\text{TT}_0$. The outer features in the data persist to later times (400 – 450 ns, Fig. 5.4b), after the most characteristic ${}^5\text{TT}_0$ signatures have disappeared, and are associated with T + T. Although there is an *EA*-like feature in the early time spectrum, the intensity of the data remains greater than zero over the full field range. This is likely from dynamic behavior that is not entirely modelled by the nonadiabatic transition theory (Chapter 2) for systems with large J ($|J| > 20$ GHz). The *JDE* model does not reproduce the powder data. Single-orientation data show that, although the energies are predicted by the *JDE* model, the intensities for some transitions are not.

A single crystal of TES TIPS-TT was mounted to make the orientation $z \parallel \vec{B}_0$ attainable within the EPR spectrometer (Fig. 5.1a). Starting with $z \parallel \vec{B}_0$ (labeled 0° , Fig. 5.4), the sample was rotated to collect trEPR spectra for different orientations about the y -axis in 10° increments between 0° and 180° . Figure 5.4 shows colored lines that correspond to ${}^5\text{TT}$ and T + T transitions between the coupled $|{}^5\text{TT}_M\rangle$ and uncoupled $|M_A, M_B\rangle$ Zeeman states, respectively (Section 3.2.7). As with the crystalline powder spectra, the features

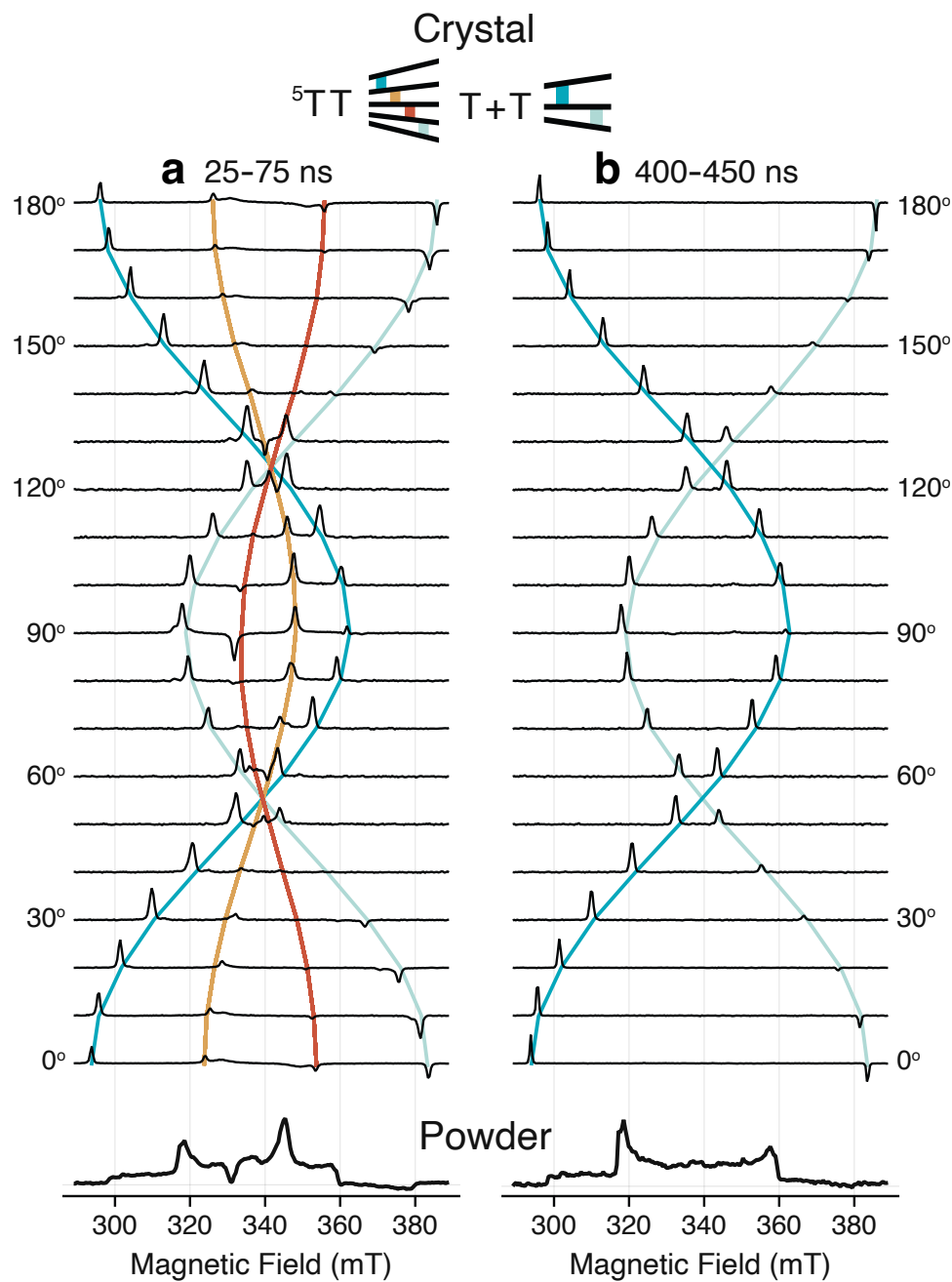


FIGURE 5.4: TrEPR spectra of a single crystal of TES TIPS-TT mounted to enable rotation of the molecular x - and z -axes in the plane of \vec{B}_0 at (a) early (25-75 ns) and (b) late (400-450 ns) times. The starting orientation of 0° represents the orientation in which $z \parallel \vec{B}_0$. Transitions within ^5TT and $\text{T} + \text{T}$ are color-coded. Below, crystalline powder of TES TIPS-TT at room temperature at early and late times (25-75 and 400-425 ns, respectively).

associated with ${}^5\text{TT}$ can be distinguished from those of $\text{T} + \text{T}$, if they are detected at early times (Fig. 5.4a) but not at late times (Fig. 5.4b). The $\text{T} + \text{T}$ spectrum is present at both early and late times and cannot be distinguished from the ${}^5\text{TT}_{\pm 2} \leftrightarrow {}^5\text{TT}_{\pm 1}$ spectrum at orientations other than $z \parallel \vec{B}_0$, where only the ${}^5\text{TT}_0$ state is populated.

The 25–75 ns spectra and the initial populations of the ${}^5\text{TT}$ and $\text{T} + \text{T}$ sublevels were calculated at all orientations with the parallel *JDE* model as described in Section 5.3. This procedure simulates the spectra at $z \parallel \vec{B}_0$ (ignoring broad inner peaks) and $x \parallel \vec{B}_0$ with an exceptional degree of accuracy (Fig. 5.5). At intermediate orientations, for example, at 50° and 120° (Figs. 5.6–5.8), there is a large degree of overlap between transitions. The ${}^5\text{TT}$ spectrum becomes more prominent as the sample is rotated from 0° to 90° . The populations of $+M$ and $-M$ Zeeman states are predicted to be equally populated in the large J limit, but, to replicate the data, the $+M$ populations were turned off. The result is a less symmetric spectrum, as in, for example, the $\theta = 40^\circ$ spectrum.

Simulations of the spectra at intermediate orientations were also successful (Figs. 5.6–5.8), especially regarding the predicted population of $\text{T} + \text{T}$ from the ${}^5\text{TT}$ populations. As with the crystalline powder spectra, many spectra exhibit a trend towards preferential population of the lower energy M sublevels. Minor discrepancies between the simulation and data are evident both in peak position and amplitude and are likely related to the simplicity of the model—the spectra were simulated with only two adjustable parameters.

The highly successful fits of sharp trEPR features at all TES TIPS-TT crystal orientations underscore the successful convergence of parallel intermolecular orientation, macroscopic crystal alignment, and rigorous theory. A critical result of the NTT presented here and in Chapter 2 is that the populations of the M -spin sublevels depend on

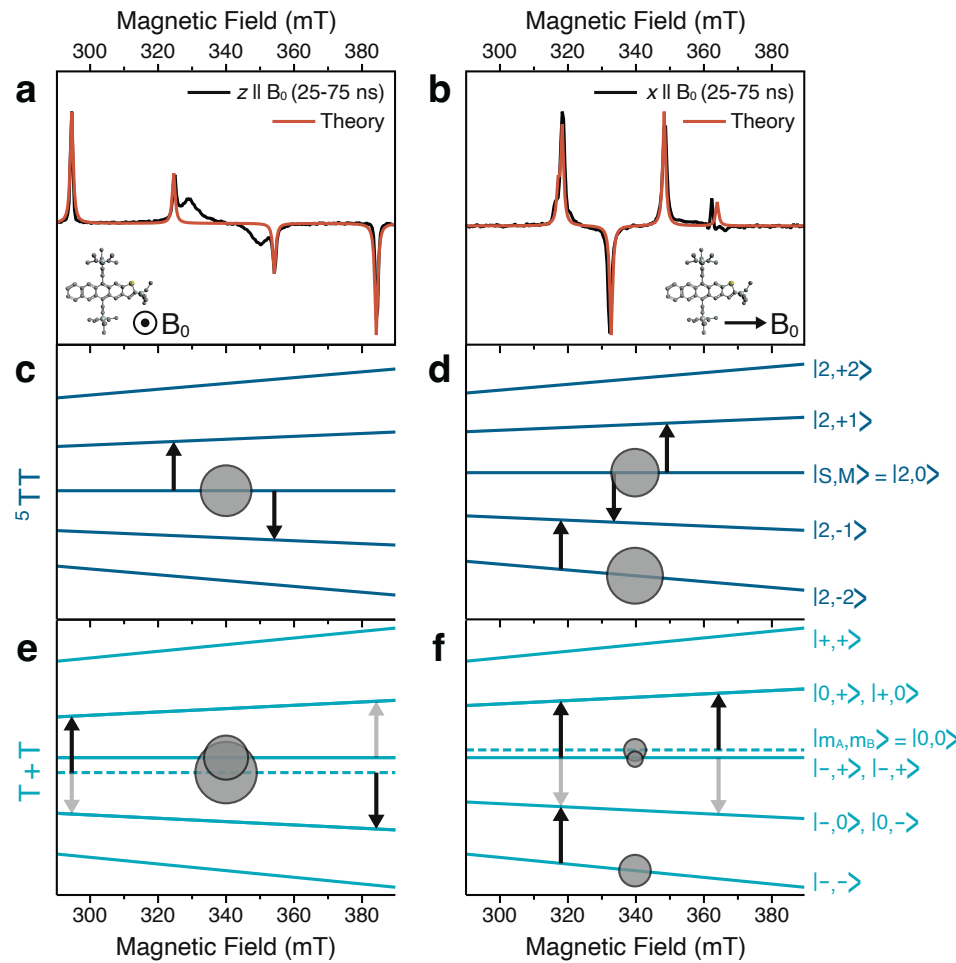


FIGURE 5.5: Early time (25-75 ns) spectra and calculations of single crystal sample at (a) $z \parallel \vec{B}_0$ and (b) $x \parallel \vec{B}_0$ with associated energy level plots for (c), (d) ⁵TT and (e), (f) dissociated triplets T + T. Based on the theory, the arrows indicate field position of relevant transitions, with the associated circle areas indicating relative populations of the relevant sublevel.

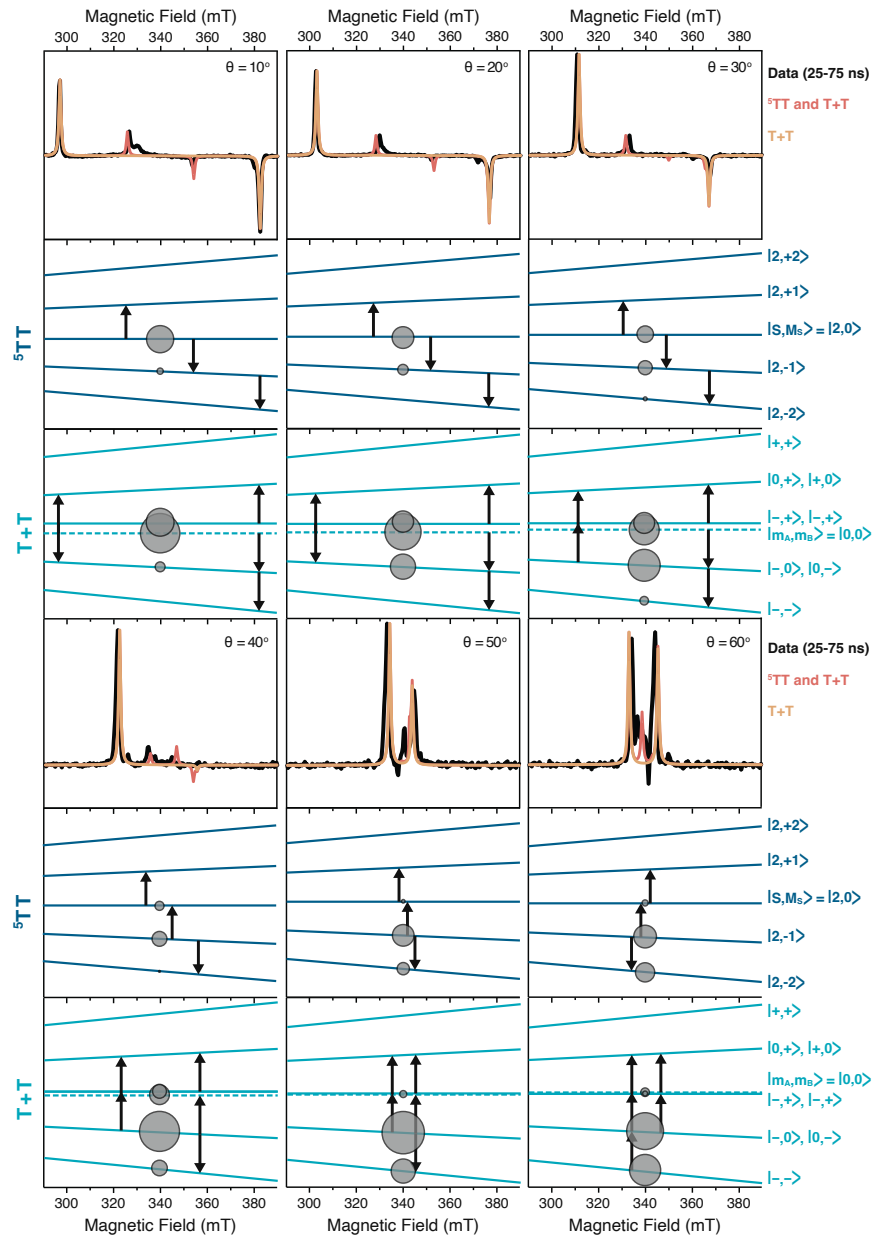


FIGURE 5.6: Calculated spectra, populations and energy level plots for single crystal trEPR data at specified orientations between 10° and 60° . The relative populations of specific sublevels are indicated by the area of the associated circles, which are positioned next to arrows that indicate allowed microwave transitions.

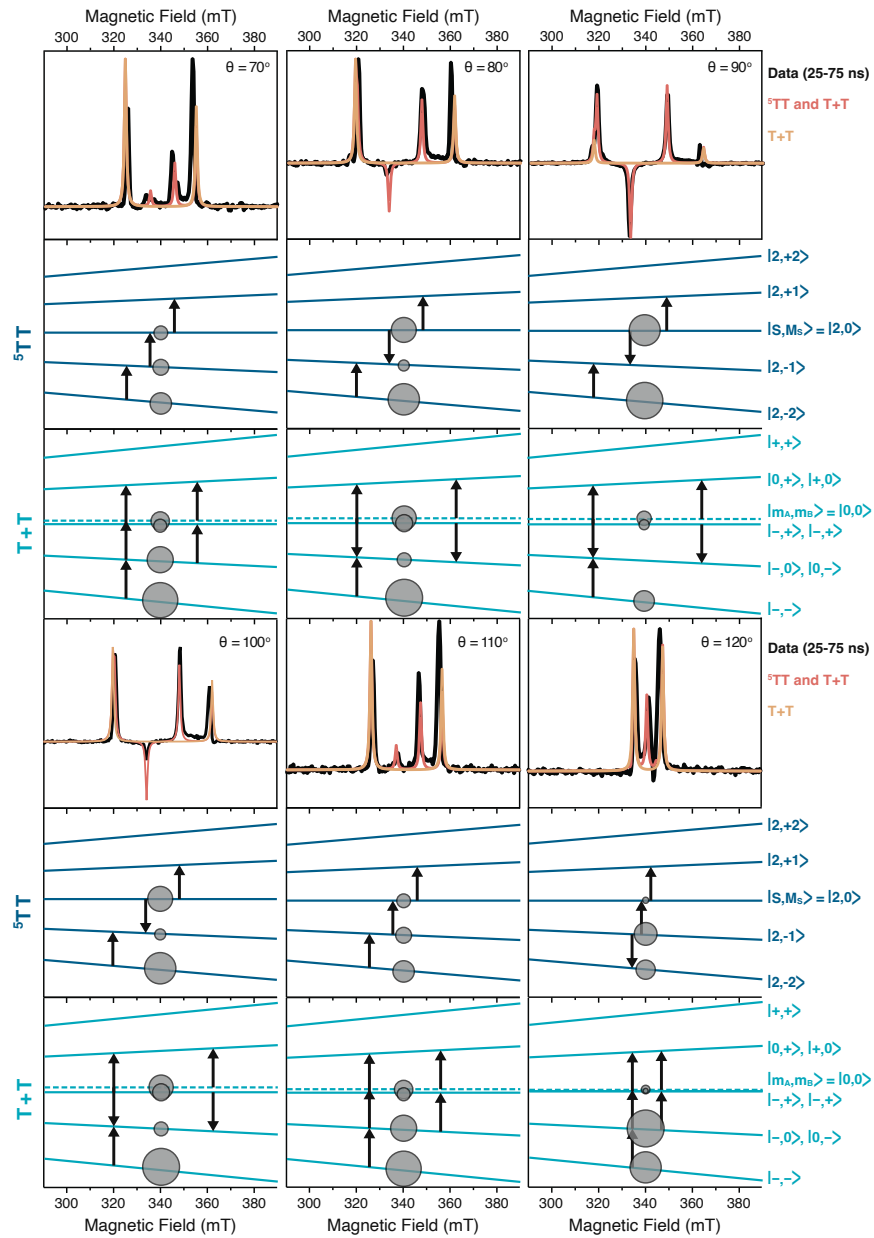


FIGURE 5.7: Calculated spectra, populations and energy level plots for single crystal trEPR data at specified orientations between 70° and 120° . The relative populations of specific sublevels are indicated by the area of the associated circles, which are positioned next to arrows that indicate allowed microwave transitions.

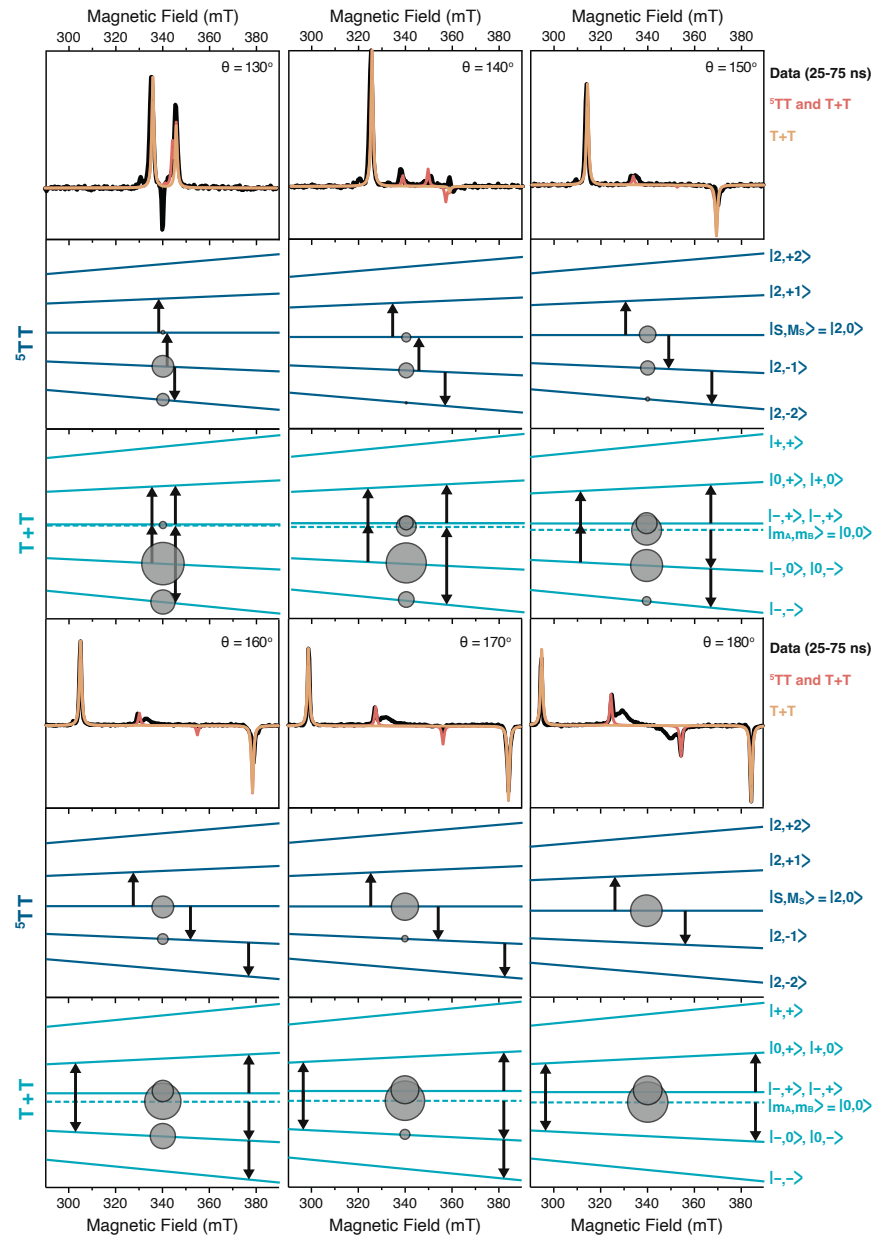


FIGURE 5.8: Calculated spectra, populations and energy level plots for single crystal trEPR data at specified orientations between 130° and 180° . The relative populations of specific sublevels are indicated by the area of the associated circles, which are positioned next to arrows that indicate allowed microwave transitions.

the orientation of the chromophore pair relative to the magnetic field. The orientational dependence for sublevel populations is a prediction that is distinct from other treatments in the literature.⁶⁰ Figs. 5.5a-5.5d shows that the populations in the ${}^5\text{TT}_M$ sublevels do indeed depend on orientation. But it also shows that the populations of the T + T levels also depend on orientation—the quantum coherence imprinted on the singlet ${}^1\text{TT}$ state from singlet fission leads to distinct, and measurable, polarizations in both the TT and the unpaired T + T trEPR spectra. Because the unpaired singlet state ${}^1\text{TT} \rightarrow \text{T} + \text{T}$ does not have an EPR spectrum, the assignments in Fig. 5.5 show that the T + T spectrum is from an unpaired quintet: ${}^1\text{TT} \rightarrow {}^5\text{TT} \rightarrow \text{T} + \text{T}$.

Concerned with potential of specific spin sublevels of TT for QI purposes, it is imperative to distinguish pure from mixed states, and this distinction renders Merrifield's theory of triplet (pair) populations,⁴⁴ based on triplet-triplet annihilation, difficult to translate to SF (see Appendix B). First, the putative unpaired T + T "state" in the Merrifield theory is not a pure quantum state but rather a mixed state with a density matrix, but not a wavefunction. The literature concerning the formation of this state is somewhat murky, sometimes invoking states like "T...T" that may or may not be pure quantum states. For fitting trEPR data, the nature of the intermediate states—pure or mixed—may not be of much interest, but in quantum applications it is crucial. Secondly, the "singlet character" approximation in the original theory and oft-resurrected in recent literature^{17,19} resembles a Franck-Condon approximation, but it is unclear why such an approximation should be valid for the triplet pair EPR spectra from singlet fission. Lastly, and perhaps most obviously, the Merrifield theory does not consider the potentially dominant J interaction between chromophores that eliminates essential curve-crossings in many systems.

The simple view of the dynamics, which evolves the ${}^5\text{TT}$ populations instantaneously,

cannot be expected to be valid on all timescales. But the results shown here indicate that it is sufficient to capture many important features in the observed trEPR spectra and it provides microscopic insight into the unpairing process with a minimal number of empirical parameters.

Bibliography

- (1) DiVincenzo, D. P. The Physical Implementation of Quantum Computation. *Fortschr. Phys.* **2000**, *48*, 771–783.
- (2) Warren, W. S. The Usefulness of NMR Quantum Computing. *Science* **1997**, *277*, 1688–1690.
- (3) Shor, P. W. Polynomial-Time Algorithms for Prime Factorization and Discrete Logarithms on a Quantum Computer. *SIAM Rev.* **1999**, *41*, 303–332.
- (4) DiVincenzo, D. P.; Loss, D. Quantum computers and quantum coherence. *J. Magn. Magn. Mater.* **1999**, *200*, 202–218.
- (5) Vandersypen, L. M.; Steffen, M.; Breyta, G.; Yannoni, C. S.; Sherwood, M. H.; Chuang, I. L. Experimental realization of Shor's quantum factoring algorithm using nuclear magnetic resonance. *Nature* **2001**, *414*, 883–7.
- (6) Fataftah, M. S.; Freedman, D. E. Progress towards creating optically addressable molecular qubits. *Chem. Commun.* **2018**, *54*, 13773–13781.
- (7) Gaita-Ariño, A.; Luis, F.; Hill, S.; Coronado, E. Molecular spins for quantum computation. *Nat. Chem.* **2019**, *11*, 301–309.
- (8) Smith, M. B.; Michl, J. Singlet Fission. *Chem. Rev.* **2010**, *110*, 6891–6936.

- (9) Smith, M. B.; Michl, J. Recent Advances in Singlet Fission. *Annu. Rev. Phys. Chem.* **2013**, *64*, 361–386.
- (10) Pope, M.; Geacintov, N. E.; Vogel, F. Singlet Exciton Fission and Triplet-Triplet Exciton Fusion in Crystalline Tetracene. *Mol. Cryst. J. Am. Chem. Soc.* **1969**, *6*, 83–104.
- (11) Burdett, J. J.; Bardeen, C. J. Quantum Beats in Crystalline Tetracene Delayed Fluorescence Due to Triplet Pair Coherences Produced by Direct Singlet Fission. *J. Am. Chem. Soc.* **2012**, *134*, 8597–8607.
- (12) Scholes, G. D. Correlated Pair States Formed by Singlet Fission and Exciton-Exciton Annihilation. *J. Phys. Chem. A* **2015**, *119*, 12699–12705.
- (13) Bardeen, C. J. Time dependent correlations of entangled states with nondegenerate branches and possible experimental realization using singlet fission. *J. Chem. Phys.* **2019**, *151*, 124503.
- (14) Lubert-Perquel, D.; Salvadori, E.; Dyson, M.; Stavrinou, P. N.; Montis, R.; Nagashima, H.; Kobori, Y.; Heutz, S.; Kay, C. W. Identifying triplet pathways in dilute pentacene films. *Nat. Commun.* **2018**, *9*, 4222.
- (15) Weiss, L. R.; Bayliss, S. L.; Kraffert, F.; Thorley, K. J.; Anthony, J. E.; Bittl, R.; Friend, R. H.; Rao, A.; Greenham, N. C.; Behrends, J. Strongly exchange-coupled triplet pairs in an organic semiconductor. *Nat. Phys.* **2017**, *13*, 176–181.
- (16) Nagashima, H.; Kawaoka, S.; Akimoto, S.; Tachikawa, T.; Matsui, Y.; Ikeda, H.; Kobori, Y. Singlet-Fission-Born Quintet State: Sublevel Selections and Trapping by Multiexciton Thermodynamics. *J. Phys. Chem. Lett.* **2018**, *9*, 5855–5861.

- (17) Tayebjee, M. J.; Sanders, S. N.; Kumarasamy, E.; Campos, L. M.; Sfeir, M. Y.; McCamey, D. R. Quintet multiexciton dynamics in singlet fission. *Nat. Phys.* **2017**, *13*, 182–188.
- (18) Matsui, Y.; Kawaoka, S.; Nagashima, H.; Nakagawa, T.; Okamura, N.; Ogaki, T.; Ohta, E.; Akimoto, S.; Sato-Tomita, A.; Yagi, S., et al. Exergonic Intramolecular Singlet Fission of an Adamantane-Linked Tetracene Dyad via Twin Quintet Multiexcitons. *J. Phys. Chem. C* **2019**, *123*, 18813–18823.
- (19) Chen, M.; Krzyaniak, M. D.; Nelson, J. N.; Bae, Y. J.; Harvey, S. M.; Schaller, R. D.; Young, R. M.; Wasielewski, M. R. Quintet-triplet mixing determines the fate of the multiexciton state produced by singlet fission in a terrylenediimide dimer at room temperature. *Proc. Natl. Acad. Sci. U. S. A.* **2019**, *116*, 8178–8183.
- (20) Basel, B. S.; Zirzlmeier, J.; Hetzer, C.; Reddy, S. R.; Phelan, B. T.; Krzyaniak, M. D.; Volland, M. K.; Coto, P. B.; Young, R. M.; Clark, T., et al. Evidence for charge-transfer mediation in the primary events of singlet fission in a weakly coupled pentacene dimer. *Chem* **2018**, *4*, 1092–1111.
- (21) Basel, B. S.; Zirzlmeier, J.; Hetzer, C.; Phelan, B. T.; Krzyaniak, M. D.; Reddy, S. R.; Coto, P. B.; Horwitz, N. E.; Young, R. M.; White, F. J., et al. Unified model for singlet fission within a non-conjugated covalent pentacene dimer. *Nat. Commun.* **2017**, *8*, 15171.
- (22) Sakai, H.; Inaya, R.; Nagashima, H.; Nakamura, S.; Kobori, Y.; Tkachenko, N. V.; Hasobe, T. Multiexciton Dynamics Depending on Intramolecular Orientations in Pentacene Dimers: Recombination and Dissociation of Correlated Triplet Pairs. *J. Phys. Chem. Lett.* **2018**, *9*, 3354–3360.

- (23) Swenberg, C. E.; Geacintov, N. E. Exciton interactions in organic solids. *Org. Mol. Photophys.* **1973**, *1*, 489–564.
- (24) Johnson, R. C.; Merrifield, R. E.; Avakian, P.; Flippen, R. B. Effects of Magnetic Fields on the Mutual Annihilation of Triplet Excitons in Molecular Crystals. *Phys. Rev. Lett.* **1967**, *19*, 285–287.
- (25) Williams, R. Delayed Fluorescence of Complex Molecules in the Vapor Phase. *J. Chem. Phys.* **1958**, *28*, 577–581.
- (26) Parker, C. A.; Hatchard, C. G. Delayed fluorescence from solutions of anthracene and phenanthrene. *Proc. R. Soc. Lond. A. Math. Phys. Sci.* **1962**, *269*, 574–584.
- (27) Avakian, P.; Abramson, E.; Kepler, R. G.; Caris, J. C. Indirect Observation of Singlet—Triplet Absorption in Anthracene Crystals. *J. Chem. Phys.* **1963**, *39*, 1127–1128.
- (28) Singh, S.; Jones, W. J.; Siebrand, W.; Stoicheff, B. P.; Schneider, W. G. Laser Generation of Excitons and Fluorescence in Anthracene Crystals. *J. Chem. Phys.* **1965**, *42*, 330–342.
- (29) Hanna, M. C.; Nozik, A. J. Solar conversion efficiency of photovoltaic and photoelectrolysis cells with carrier multiplication absorbers. *J. Appl. Phys.* **2006**, *100*, 074510.
- (30) Paci, I.; Johnson, J. C.; Chen, X.; Rana, G.; Popović, D.; David, D. E.; Nozik, A. J.; Ratner, M. A.; Michl, J. Singlet Fission for Dye-Sensitized Solar Cells: Can a Suitable Sensitizer Be Found? *J. Am. Chem. Soc.* **2006**, *128*, 16546–16553.
- (31) Weber, S. In *eMagRes*; John Wiley & Sons, Ltd: 2017, pp 255–270.
- (32) Biskup, T. Structure-Function Relationship of Organic Semiconductors: Detailed Insights From Time-Resolved EPR Spectroscopy. *Front. Chem.* **2019**, *7*, 1–22.

- (33) Weil, J. A.; Bolton, J. R., *Electron Paramagnetic Resonance: Elementary Theory and Practical Applications*, 2nd; John Wiley & Sons: Hoboken, N.J., 2007.
- (34) Hutchison, C. A.; Mangum, B. W. Paramagnetic Resonance Absorption in Naphthalene in Its Phosphorescent State. *J. Chem. Phys.* **1961**, *34*, 908–922.
- (35) Gilligan, A. T.; Miller, E. G.; Sammakia, T.; Damrauer, N. H. Using Structurally Well-Defined Norbornyl-Bridged Acene Dimers to Map a Mechanistic Landscape for Correlated Triplet Formation in Singlet Fission. *J. Am. Chem. Soc.* **2019**, *141*, 5961–5971.
- (36) Pedash, Y. F.; Prezhdo, O. V.; Kotelevskiy, S. I.; Prezhdo, V. V. Spin-orbit coupling and luminescence characteristics of conjugated organic molecules. I. Polyacenes. *J. Mol. Struct.: THEOCHEM* **2002**, *585*, 49–59.
- (37) Collins, M. I.; McCamey, D. R.; Tayebjee, M. J. Y. Fluctuating exchange interactions enable quintet multiexciton formation in singlet fission. *J. Chem. Phys.* **2019**, *151*, 164104.
- (38) Bencini, A.; Gatteschi, D., *Electron Paramagnetic Resonance of Exchange Coupled Systems*; Springer-Verlag Berlin Heidelberg: Berlin, Heidelberg, 1990, pp X–287.
- (39) Van Strien, A. J.; Schmidt, J. An EPR study of the triplet state of pentacene by electron spin-echo techniques and laser flash excitation. *Chem. Phys. Lett.* **1980**, *70*, 513–517.
- (40) Miyata, K.; Conrad-Burton, F. S.; Geyer, F. L.; Zhu, X.-Y. Triplet Pair States in Singlet Fission. *Chem. Rev.* **2019**, *119*, 4261–4292.

- (41) Wakasa, M.; Kaise, M.; Yago, T.; Katoh, R.; Wakikawa, Y.; Ikoma, T. What Can Be Learned from Magnetic Field Effects on Singlet Fission: Role of Exchange Interaction in Excited Triplet Pairs. *J. Phys. Chem. C* **2015**, *119*, 25840–25844.
- (42) Yarmus, L.; Rosenthal, J.; Chopp, M. EPR of triplet excitons in tetracene crystals: spin polarization and the role of singlet exciton fission. *Chem. Phys. Lett.* **1972**, *16*, 477–481.
- (43) Sternlicht, H.; McConnell, H. M. Paramagnetic Excitons in Molecular Crystals. *J. Chem. Phys.* **1961**, *35*, 1793–1800.
- (44) Merrifield, R. E. Magnetic effects on triplet exciton interactions. *Pure and App. Chem.* **1971**, *27*, 481–498.
- (45) Edmonds, A. R., *Angular momentum in quantum mechanics*; Princeton university press: 1996, pp 1–146.
- (46) Benk, H.; Sixl, H. Theory of two coupled triplet states. *Mol. Phys.* **1981**, *42*, 779–801.
- (47) Johnson, R. C.; Merrifield, R. E. Effects of Magnetic Fields on the Mutual Annihilation of Triplet Excitons in Anthracene Crystals. *Phys. Rev. B* **1970**, *1*, 896–902.
- (48) Matsuda, S.; Oyama, S.; Kobori, Y. Electron spin polarization generated by transport of singlet and quintet multiexcitons to spin-correlated triplet pairs during singlet fissions. *Chem. Sci.* **2020**.
- (49) Hore, P. J. In *Advanced EPR*, Hoff, A. J., Ed.; Elsevier: Amsterdam, 1989, pp 405–440.
- (50) Brennen, G. K.; O'Leary, D. P.; Bullock, S. S. Criteria for exact qudit universality. *Phys. Rev. A* **2005**, *71*, 052318.

- (51) Sakurai, J. J.; Tuan, S. F., *Modern Quantum Mechanics*; Addison-Wesley Pub. Co.: Reading, Mass., 1994.
- (52) Kollmar, C.; Sixl, H.; Benk, H.; Denner, V.; Mahler, G. Theory of two coupled triplet states - electrostatic energy splittings. *Chem. Phys. Lett.* **1982**, *87*, 266–270.
- (53) Mueller, L. J. Tensors and rotations in NMR. *Concepts Magn. Reson. A* **2011**, *38A*, 221–235.
- (54) Varshalovich, D. A.; Moskalev, A. N.; Khersonskii, V. K. In 1988, pp 333–411.
- (55) Mogensen, P. K.; Riseth, A. N. Optim: A mathematical optimization package for Julia. *J. Open Source Softw.* **2018**, *3*, 615.
- (56) Goffe, W. L.; Ferrier, G. D.; Rogers, J. Global optimization of statistical functions with simulated annealing. *J. Econom.* **1994**, *60*, 65–99.
- (57) Dutt, M. V. G. et al. Quantum register based on individual electronic and nuclear spin qubits in diamond. *Science* **2007**, *316*, 1312–1316.
- (58) Bayliss, S. L. et al. Optically addressable molecular spins for quantum information processing. *Science* **2020**, *370*, 1309–1312.
- (59) Johnson, R. C.; Merrifield, R. E. Effects of Magnetic Fields on the Mutual Annihilation of Triplet Excitons in Anthracene Crystals. *Phys. Rev. B* **1970**, *1*, 896–902.
- (60) Jacobberger, R. M.; Qiu, Y.; Williams, M. L.; Krzyaniak, M. D.; Wasielewski, M. R. Using Molecular Design to Enhance the Coherence Time of Quintet Multiexcitons Generated by Singlet Fission in Single Crystals. *J. Am. Chem. Soc.* **2021**.

- (61) Nakamura, S. et al. Synergetic Role of Conformational Flexibility and Electronic Coupling for Quantitative Intramolecular Singlet Fission. *J. Phys. Chem. C* **2021**, *125*, 18287–18296.
- (62) Schröder, M.; Rauber, D.; Matt, C.; Kay, C. W. M. Pentacene in 1,3,5-Tri(1-naphthyl)benzene: A Novel Standard for Transient EPR Spectroscopy at Room Temperature. *Appl. Magn. Reson.* **2021**.
- (63) Papadopoulos, I. et al. Varying the Interpentacene Electronic Coupling to Tune Singlet Fission. *J. Am. Chem. Soc.* **2019**, *141*, 6191–6203.
- (64) Chernick, E. T. et al. Pentacene Appended to a TEMPO Stable Free Radical: The Effect of Magnetic Exchange Coupling on Photoexcited Pentacene. *J. Am. Chem. Soc.* **2015**, *137*, 857–863.
- (65) Astashkin, A.; Schweiger, A. Electron-spin transient nutation: a new approach to simplify the interpretation of ESR spectra. *Chem. Phys. Lett.* **1990**, *174*, 595–602.
- (66) Stoll, S.; Jeschke, G.; Willer, M.; Schweiger, A. Nutation-Frequency Correlated EPR Spectroscopy: The PEANUT Experiment. *J. Magn. Reson.* **1998**, *130*, 86–96.
- (67) Furrer, R. et al. Transient ESR nutation signals in excited aromatic triplet states. *Chem. Phys. Lett.* **1980**, *75*, 332–339.
- (68) Torrey, H. C. Transient Nutations in Nuclear Magnetic Resonance. *Phys. Rev.* **1949**, *76*, 1059–1068.
- (69) Kardar, M., *Statistical Physics of Particles*; Cambridge University Press: Cambridge, 2007.
- (70) Lewis, S. G.; Smyser, K. E.; Eaves, J. D. Clock transitions guard against spin decoherence in singlet fission. *J. Chem. Phys.* **2021**, *155*, 194109.

- (71) Bayliss, S. L. et al. Site-selective measurement of coupled spin pairs in an organic semiconductor. *Proc. Natl. Acad. Sci. U. S. A.* **2018**, *115*, 201718868.
- (72) Bayliss, S. L.; Weiss, L. R.; Rao, A.; Friend, R. H.; Chepelianskii, A. D.; Greenham, N. C. Spin signatures of exchange-coupled triplet pairs formed by singlet fission. *Phys. Rev. B* **2016**, *94*, 045204.
- (73) Teichen, P. E.; Eaves, J. D. Collective aspects of singlet fission in molecular crystals. *J. Chem. Phys.* **2015**, *143*, 044118.
- (74) Blum, K. Density Matrix Theory and Applications. *Springer Series on Atomic, Optical, and Plasma Physics* **2012**.
- (75) Nielsen, M. A.; Chuang, I. L., *Quantum computation and quantum information*, 10th anniversary; Cambridge University Press: Cambridge;New York; 2010.
- (76) Merrifield, R. E. Theory of Magnetic Field Effects on the Mutual Annihilation of Triplet Excitons. *J. Chem. Phys.* **1968**, *48*, 4318–4319.
- (77) Bae, Y. J.; Zhao, X.; Kryzaniak, M. D.; Nagashima, H.; Strzalka, J.; Zhang, Q.; Wasielewski, M. R. Spin Dynamics of Quintet and Triplet States Resulting from Singlet Fission in Oriented Terrylenediimide and Quaterrylenediimide Films. *J. Phys. Chem. C* **2020**, *124*, 9822–9833.
- (78) Snaathorst, D.; Keijzers, C. P. Triplet-triplet interactions between dimers of a copper maleonitriledithiolate complex. *Mol. Phys.* **1984**, *51*, 509–524.

Appendix A

Quantifying Entanglement

In singlet fission, a photon prepares an optically excited state that rapidly decays into two spin-entangled triplet excitations. The initially formed state is the maximally entangled singlet pair state ${}^1\text{TT}$. To say that the ${}^1\text{TT}$ state is maximally entangled, there must be a measurement of entanglement. Below, I consider two measures of entanglement: the Schmidt rank and the entropy of entanglement.

The Schmidt rank for any bipartite pure state with Schmidt decomposition,

$$|\psi\rangle_{AB} = \sum_{i=1}^N \lambda_i |a_i\rangle_A |b_i\rangle_B, \quad (\text{A.1})$$

is defined as the number of non-zero coefficients λ_i . This is equal to the rank of the reduced density matrices $\rho_A = \sum_i \lambda_i^2 |a_i\rangle_A \langle a_i|_A$ and $\rho_B = \sum_i \lambda_i^2 |b_i\rangle_B \langle b_i|_B$, whose eigenvalues λ_i^2 are identical. λ_i are the *Schmidt coefficients* satisfying $\sum_i \lambda_i^2 = 1$.⁷⁵

As an example, consider the Schmidt rank of the $|{}^5\text{TT}_0\rangle$ state by expressing it as a Schmidt decomposition. First, the reduced density matrix, $\rho_A = \sum_i \lambda_i^2 |a_i\rangle_A \langle a_i|_A$ is diagonalized to find the λ_i . For $|{}^5\text{TT}_0\rangle = \sqrt{\frac{1}{6}} (2|00\rangle + |+-\rangle + |-+\rangle)$, the bipartite density

matrix is,

$$\begin{aligned}\rho_{AB} &= |^5\text{TT}_0\rangle\langle ^5\text{TT}_0| \\ &= \frac{1}{6} (4|00\rangle\langle 00| + 2|00\rangle\langle +-| + 2|00\rangle\langle -+| \\ &\quad + 2|+-\rangle\langle 00| + |+-\rangle\langle +-| + |+-\rangle\langle -+| \\ &\quad + 2|-+\rangle\langle 00| + |-+\rangle\langle +-| + |-+\rangle\langle -+|).\end{aligned}\tag{A.2}$$

The reduced density matrix $\rho_A = \text{tr}_B(\rho_{AB})$ is,

$$\begin{aligned}\rho_A &= \langle +|_B \rho_{AB} |+\rangle_B + \langle 0|_B \rho_{AB} |0\rangle_B + \langle -|_B \rho_{AB} |-\rangle_B \\ &= \frac{1}{6} (|-\rangle_A \langle -|_A + 4|0\rangle_A \langle 0|_A + |+\rangle_A \langle +|_A).\end{aligned}\tag{A.3}$$

The density matrix is already in diagonal form, $\rho_A = \lambda_0|0\rangle\langle 0| + \lambda_1|+\rangle\langle +| + \lambda_2|-\rangle\langle -|$.

We can read off the eigenvalues $\lambda_0 = \frac{1}{6}$, $\lambda_1 = \frac{2}{3}$, and $\lambda_2 = \frac{1}{6}$, for the eigenbasis $\{| \lambda_i \rangle\} = \{|-\rangle_A, |0\rangle_A, |+\rangle_A\}$.

Likewise, the reduced density matrix for B is, $\rho_B = \frac{1}{6} (|-\rangle_B \langle -|_B + 4|0\rangle_B \langle 0|_B + |+\rangle_B \langle +|_B)$. For $i = 0 - 2$, we construct the Schmidt decomposition, $|\psi\rangle_{AB} = \sqrt{\frac{1}{6}}|-\rangle + \sqrt{\frac{2}{3}}|00\rangle + \sqrt{\frac{1}{6}}|+-\rangle$, and find that the Schmidt rank of $|^5\text{TT}_0\rangle$ is 3. By this measure, the ${}^5\text{TT}_0$ and ${}^1\text{TT}$ states are both maximally entangled.

In fact, the $|S, M\rangle$ states, as written in Eq. 3.47, are all already written as Schmidt decompositions. An example of a state that is not already written in this form is $|\psi\rangle = (|00\rangle + |0+\rangle + |++\rangle)/\sqrt{3}$. Continuing this procedure for the remaining quintet states, it is easy to see that the $M = \pm 1$ states are rank 2 and that the $M = \pm 2$ states are rank 1. A state is entangled if and only if its Schmidt rank is greater than one, so clearly the $|\pm\pm\rangle$ states are not entangled.

The entropy of entanglement expresses the distribution of a state's Schmidt coefficients λ_i , $S = -\sum_i |\lambda_i|^2 \log_2(|\lambda_i|^2)$. A maximally entangled state—a state in which all singular values are equal—has a maximum value of the entanglement entropy, defined as,

$$S = -\sum_{i=1}^N \frac{1}{N} \log_2\left(\frac{1}{N}\right). \quad (\text{A.4})$$

For qubits, the maximum entropy is $S = -\log_2\left(\frac{1}{2}\right) = 1$. The qubit state $|\psi\rangle = \sqrt{\frac{1}{2}}|00\rangle + \sqrt{\frac{1}{2}}|11\rangle$ is said to be maximally entangled because the entanglement entropy is maximal among all two-qubit states. Entanglement entropy diminishes as $\epsilon \rightarrow 0$ for $|\phi\rangle = \sqrt{\epsilon}|00\rangle + \sqrt{1-\epsilon}|11\rangle$.

Likewise $|{}^1\text{TT}\rangle = \sqrt{\frac{1}{3}}(|00\rangle - |+-\rangle - |-+\rangle)$ is a maximally entangled qutrit state. For the coupled triplet pair, the maximum entropy is $S = -\log_2\left(\frac{1}{3}\right) \approx 1.6$. The entanglement entropy of the $|{}^5\text{TT}_0\rangle$ sublevel is $S = -\left(\frac{1}{6}\log_2\left(\frac{1}{6}\right) + \frac{2}{3}\log_2\left(\frac{2}{3}\right) + \frac{1}{6}\log_2\left(\frac{1}{6}\right)\right) \approx 1.3$. Although both $|{}^1\text{TT}\rangle$ and $|{}^5\text{TT}_0\rangle$ have maximal rank, the entropy of entanglement for the $|{}^1\text{TT}\rangle$ state is greater than that of the $|{}^5\text{TT}_0\rangle$ sublevel.

Appendix B

The Q_0 Model

In 1967, the discovery of magnetic field effects on the photoluminescence (PL) intensity from anthracene crystals proved the existence of singlet fission.²⁴ In their seminal study, Johnson and Merrifield reported two magnetic field regimes in which the intensity of PL from S_0S_1 (Fig. 1.2) either increased or decreased in anthracene crystals. The fluorescence intensity decreased at high fields (35-300 mT) and, remarkably, this effect was a function of the direction of the magnetic field relative to the crystal axes (Fig. B.1). The dips appear in the spectrum when states are tuned into resonance by reorienting the sample to change the effective field. They systematically assigned this observation to the result of a varying triplet-triplet annihilation rate constant, which decreases when states that are allowed to annihilate mix with dark states.

This breakthrough was the first step in understanding triplet exciton interactions in singlet fission crystals and motivated a model for the rate of triplet-triplet annihilation through the singlet channel in singlet fission chromophores.⁷⁶ When the Zeeman energy dominates the hamiltonian, the Zeeman pair states are perturbed by zero-field energies that become orientation dependent in the field (Section 1.3, Fig. 1.7). Rotation of the system modulates the local fields and induces level-crossings, where dominant features in the spectrum appear (Fig. B.1). They explain that only pairs with spin states that contain

a singlet component can annihilate. Therefore, the selection rule mediated annihilation rate must depend on the form of the spin wavefunction.

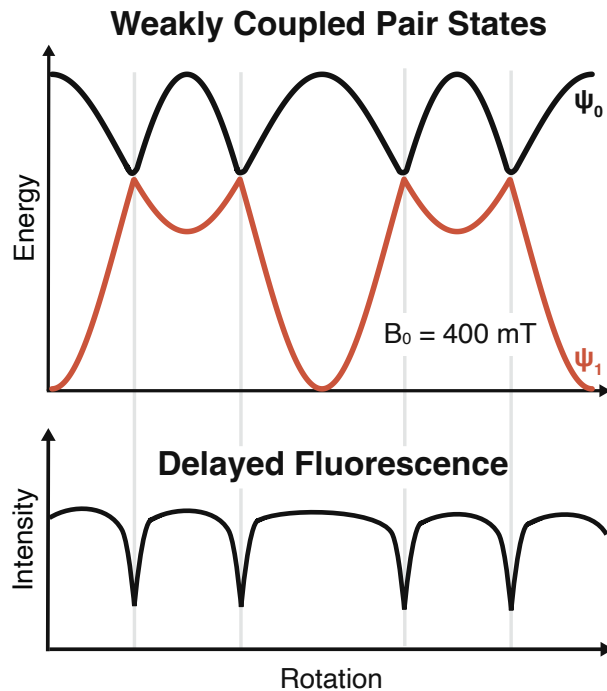


FIGURE B.1: Reproduction of the strong-field PL spectrum from Johnson and Merrifield⁵⁹ and calculated pair state energies. In a strong field ($B_0 = 400$ mT), weakly coupled triplets have two pair states with singlet components (ψ_0 and ψ_1 , Eq. B.5). They are split by the intra-chromophore magnetic dipole interactions (Section 3.2.4). Because the applied field modulates the local field from these magnetic interactions, the splitting is a function of the orientation of the chromophores with respect to the field. Johnson and Merrifield showed that dips in the fluorescence spectrum appear at sublevel degeneracies.

Merrifield's model is fundamentally based on the selection rules for the annihilation process—triplet-triplet annihilation is spin-allowed—so that fusion through the singlet channel is only accessible by a state with non-zero singlet amplitude. The rate ($\gamma_{0 \rightarrow 0}$) of singlet channel fusion,



was said to be proportional to the “singlet character” of the states,

$$\gamma_{0 \rightarrow 0} \propto \sum_i |\langle {}^1\text{TT} | \psi_i \rangle|^2. \quad (\text{B.2})$$

The amount of singlet character is quantified by the probability amplitude $|\langle {}^1\text{TT} | \psi_i \rangle|^2$, where $|{}^1\text{TT}\rangle$ is the eigenstate of the total spin operator squared \mathbf{S}^2 with eigenvalue zero, i.e., the **pure singlet state**. $|\psi_i\rangle$ is the i -th eigenstate of the experimentally relevant TT hamiltonian, $\mathcal{H}|\psi_i\rangle = E_i|\psi_i\rangle$, which according to Merrifield’s model is,

$$\mathcal{H} = g\mu_B \mathbf{B}_0(\mathbf{S}_A + \mathbf{S}_B) + D(S_{Az}^2 + S_{Bz}^2) + E(S_{Ax}^2 + S_{Bx}^2 - S_{Ay}^2 - S_{By}^2). \quad (\text{B.3})$$

Here, all inter-triplet interactions, like J and X , are neglected and magnetic parameters, D and E , are averages for inequivalent pairs. Merrifield’s zero-field splitting (ZFS) hamiltonian in Eq. B.3 is equivalent to the parallel JDE model ZFS hamiltonian in Eq. 2.2, because it considers the orientation of the averaged ZFS interaction in the field. Note the lack of subscripts on D and E that would refer to spatially unique pair sites.

The ZFS hamiltonian does not commute with \mathbf{S}^2 . So at degeneracies, it couples states by energies that are large compared to their splitting, which is effectively zero. For this reason, Merrifield refers to the eigenstates of the full hamiltonian as having mixed spin “character”—they are mixed singlet-triplet-quintet states. At high fields, Merrifield expressed the $|\psi_i\rangle$ as linear combinations of the T + T, free triplet spin states $|M_A M_B\rangle$ (Eq. 3.44), which were assumed to be equally populated. The pure singlet state, for example, in terms of the $|M_A M_B\rangle$ states is $|{}^1\text{TT}\rangle = (|00\rangle - |-\+\rangle - |+-\rangle)/\sqrt{3}$. The singlet character simply comes from the coefficient C_i that re-expresses the i -th eigenstate of the

hamiltonian in terms of the $|^1\text{TT}\rangle$ state,

$$\begin{aligned} |\psi_i\rangle &= C_i |^1\text{TT}\rangle + \dots \\ &= \langle ^1\text{TT}|\psi_i\rangle |^1\text{TT}\rangle + \dots \end{aligned} \tag{B.4}$$

By treating the ZFS perturbatively in the strong field limit, Merrifield approximated the eigenstates of Eq. B.3 by the Zeeman $|M_A M_B\rangle$ states. In this limit, and for $J = 0$, two states have singlet character,

$$\begin{aligned} |\psi_0\rangle &= |00\rangle \\ |\psi_1\rangle &= (|-\rangle + |+\rangle)/\sqrt{2}. \end{aligned} \tag{B.5}$$

Here, $|\psi_1\rangle$ is the exchange symmetric linear combination of the degenerate $|-\rangle$ and $|+\rangle$ states.

As discussed in Chapter 2, the nonadiabatic transition theory from the *JDE* model calculates the initial populations of the quintet magnetic sublevels following singlet fission from the *JDE* model hamiltonian. They are said to be approximately equal to the rate of transition ($\gamma_{0 \rightarrow 2}$),



It says that the transition rates $\gamma_{0 \rightarrow 2}$ for interconversion between the initially formed $|^1\text{TT}\rangle$ state and quintet sublevels $|{}^5\text{TT}_M\rangle$, immediately following singlet fission, may be approximated by the golden rule,

$$\gamma_{0 \rightarrow 2} = \left(\frac{2\pi}{\hbar} \right) |\langle {}^1\text{TT} | V | {}^5\text{TT}_M \rangle|^2 \delta(E_{{}^5\text{TT}_M} - E_{{}^1\text{TT}}), \tag{B.7}$$

to first-order in perturbation theory.⁵¹ In words, the rate of transition between the initially formed $|^1\text{TT}\rangle$ state and the final $|^5\text{TT}_M\rangle$ sublevel is proportional to the transition probability $|\langle ^1\text{TT}|V|^5\text{TT}\rangle|^2$, which comes from propagating the initial state in time. Here $\delta(E_{^5\text{TT}_M} - E_{^1\text{TT}})$ ensures energy conservation of the transition, which is afforded by the fluctuating exchange interaction. The *JDE* model assumes that the initially formed triplet pair is strongly coupled so a single hamiltonian is used to calculate both the populations and energies of the ${}^5\text{TT}_M$ levels. Because the ZFS interactions in V depend on the system's orientation with respect to the field, the populations from the *JDE* model are a function of orientation. The populations from the *JDE* model for strongly coupled dimers predict (Chapter 2) and assign the EPR spectrum from both molecular dimers (Chapter 4) and dimers in crystals (Chapter 5), very well.

Often, there are claims that singlet fission selectively populates the $M = 0$ sublevel of the quintet state, independent of orientation.^{15,17,19,20,22,48,60,77} These claims are based on an adaption of Merrifield's model⁴⁷ for the rate of triplet-triplet annihilation.^{15,17,19,48} In Chapter 4, I refer to this as the "Q₀ model" and show that it does not describe the EPR spectrum from the strongly coupled TIPS-BP1' dimer. This approximation is very common in the literature because without a theory for the populations, they become additional parameters when fitting the EPR spectrum.¹⁶ Though why there is preference for the Q₀ model is unclear. **It requires that the rates of entirely different processes—the rate of the spin conversion process in Eq. B.6 and the rate of singlet channel fusion, Eq. B.1—are equivalent.** Recall, further assumptions of Merrifield's model include: (1) The chromophores are orientationally and molecularly indistinguishable (Eq. B.3, $D = (D_A + D_B) / 2$); (2) The triplets are independent or weakly coupled (Eq. B.3, $J = 0$); (3) The process is spin conserving; (4) The independent triplet states $|M_A, M_B\rangle$ are equally

populated; and (5) The initial and final states are degenerate.

To arrive at the Q_0 model, it is often assumed that the population of a TT pair sub-level is equal to its singlet character. But in the adapted models, it is most common to redefine the “singlet character” as the probability amplitude of $|\psi_0\rangle$ and $|\psi_1\rangle$ (Eq. B.5), the result of Merrifield’s model, instead of using Merrifield’s definition in Eq. B.4.^{15,17,19} The population p_n of state $|n\rangle$ is set equal to the sum,

$$p_n = |\langle\psi_0|n\rangle|^2 + |\langle\psi_1|n\rangle|^2. \quad (\text{B.8})$$

Some say $|n\rangle$ are the coupled Zeeman states $|^{2S+1}\text{TT}_M\rangle$.¹⁵ The resulting populations are simple to calculate. First, $|\psi_0\rangle$ and $|\psi_1\rangle$ can be re-expressed in terms of the $|^{2S+1}\text{TT}_M\rangle$ states,

$$\begin{aligned} |\psi_0\rangle &= \sqrt{\frac{1}{3}}|^1\text{TT}\rangle + \sqrt{\frac{2}{3}}|^5\text{TT}_0\rangle \\ |\psi_1\rangle &= -\sqrt{\frac{2}{3}}|^1\text{TT}\rangle + \sqrt{\frac{1}{3}}|^5\text{TT}_0\rangle. \end{aligned} \quad (\text{B.9})$$

According to Eq. B.5, the Q_0 model actually assumes that the population of state $|n\rangle$ is proportional to its $|^1\text{TT}$ and $|^5\text{TT}_0$, or Q_0 , character,

$$p_n = \left| \sqrt{\frac{1}{3}}\langle ^1\text{TT}|n\rangle + \sqrt{\frac{2}{3}}\langle ^5\text{TT}_0|n\rangle \right|^2 + \left| -\sqrt{\frac{2}{3}}\langle ^1\text{TT}|n\rangle + \sqrt{\frac{1}{3}}\langle ^5\text{TT}_0|n\rangle \right|^2. \quad (\text{B.10})$$

For $|n\rangle = |^{2S+1}\text{TT}_M\rangle$, p_n is zero unless $|n\rangle = |^1\text{TT}\rangle$ or $|^5\text{TT}_0\rangle$. So it is assumed that they are the only states populated, regardless of the system’s orientation or hamiltonian. The result is that the EPR spectrum is assigned entirely to transitions from $|^5\text{TT}_0$.

Merrifield’s model described the annihilation rate at field-induced degeneracies. Models based on this static model, which calculate the ^5TT EPR spectrum as a function of

a varying field, therefore require that $|^1\text{TT}\rangle$ and $|^5\text{TT}_0\rangle$ are degenerate always, i.e. $J = 0$. But it is common to claim, instead, that the spectrum is from dimers with large J . In this case, one hamiltonian where J is large is used to calculate the energies of the spectrum and another, while the model used to calculate populations is based on a different hamiltonian (Eq. B.3), where J is zero. To find a general form for the populations from this argument, let $|n\rangle = |\phi_i\rangle$, where $|\phi_i\rangle$ are the eigenstates of a hamiltonian that includes a large exchange interaction, $\mathcal{H}'|\phi_i\rangle = E_i|\phi_i\rangle$.^{17,19} Using perturbation theory, I will approximate the population of state $|\phi_i\rangle$ according to Eq. B.8. As an example, consider \mathcal{H}' equal to the *JDE* model hamiltonian. In perturbation theory, the hamiltonian is partitioned into strongly interacting parts,

$$H_0 = g\mu_B B_0 S_z + J \mathbf{S}_A \cdot \mathbf{S}_B \quad (\text{B.11})$$

and weak perturbations,

$$V = \mathbf{S}_A^\top \cdot \mathbf{D}_A \cdot \mathbf{S}_A + \mathbf{S}_B^\top \cdot \mathbf{D}_B \cdot \mathbf{S}_B + \mathbf{S}_A^\top \cdot \mathbf{X} \cdot \mathbf{S}_B. \quad (\text{B.12})$$

To first approximation, or zeroth order, the eigenstates of $\mathcal{H}' = H_0 + V$ are approximated by the coupled Zeeman states, $H_0|\phi_i\rangle_0 = E_{0,i}|\phi_i\rangle_0$ where $|\phi_i\rangle_0 = |^{2S+1}\text{TT}_M\rangle$. This is similar to the approximation that Merrifield made in the original theory but J was zero so the result was the uncoupled Zeeman states, $|M_A, M_B\rangle$. For $|n\rangle = |^{2S+1}\text{TT}_M\rangle$, and for the alternate definition of singlet character in Eq. B.10, only the $M = 0$ quintet sublevel is populated.

The first order approximation to the i -th eigenket of the full hamiltonian is,

$$|\phi_i\rangle_1 = |\phi_i\rangle_0 + \sum_{k \neq i} |\phi_k\rangle_0 \frac{0\langle\phi_k|V|\phi_i\rangle_0}{E_{0,i} - E_{0,k}}, \quad (\text{B.13})$$

where $|\phi_i\rangle_0$ is, again, the i -th energy eigenstate of the unperturbed hamiltonian H_0 (Eq. B.11). According to Eq. B.10, the only $|\phi_i\rangle_1$ states with non-zero population are states with non-zero $|^1\text{TT}\rangle$ and $|^5\text{TT}_0\rangle$ amplitude. These are:

$$\begin{aligned} |^1\text{TT}\rangle_1 &= |^1\text{TT}\rangle - |^5\text{TT}_0\rangle \frac{\langle ^5\text{TT}_0|V|^1\text{TT}\rangle}{3J} + \dots \\ |^3\text{TT}_M\rangle_1 &= |^1\text{TT}\rangle \frac{\langle ^1\text{TT}|V|^3\text{TT}_M\rangle}{J + g\mu_B B_0 M} + |^5\text{TT}_0\rangle \frac{\langle ^5\text{TT}_0|V|^3\text{TT}_M\rangle}{2J + g\mu_B B_0 M} + \dots \\ |^5\text{TT}_M\rangle_1 &= |^5\text{TT}_M\rangle + |^1\text{TT}\rangle \frac{\langle ^1\text{TT}|V|^5\text{TT}_M\rangle}{3J + g\mu_B B_0 M} + \dots, \end{aligned} \quad (\text{B.14})$$

where the denominators are the difference between the corresponding diagonal elements of H_0 (Eq. B.11), assuming $J > 0$. Considering only the populations of the quintet states, $|n\rangle = |^5\text{TT}_M\rangle_1$, the singlet and $M = 0$ quintet amplitudes (Eq. B.10) are,

$$\begin{aligned} \langle ^1\text{TT}|^5\text{TT}_M\rangle_1 &= \langle ^1\text{TT}|^5\text{TT}_M\rangle + \langle ^1\text{TT}|^1\text{TT}\rangle \frac{\langle ^1\text{TT}|V|^5\text{TT}_M\rangle}{3J + g\mu_B B_0 M} + \dots \\ &= \frac{\langle ^1\text{TT}|V|^5\text{TT}_M\rangle}{3J + g\mu_B B_0 M}, \end{aligned} \quad (\text{B.15})$$

and

$$\begin{aligned} \langle ^5\text{TT}_0|^5\text{TT}_M\rangle_1 &= \langle ^5\text{TT}_0|^5\text{TT}_M\rangle + \langle ^5\text{TT}_0|^1\text{TT}\rangle \frac{\langle ^5\text{TT}_0|V|^5\text{TT}_M\rangle}{3J + g\mu_B B_0 M} + \dots \\ &= \delta_{M,0}, \end{aligned} \quad (\text{B.16})$$

where $\delta_{M,0}$ is unity when $M = 0$ and zero otherwise. By placing this result into Eq. B.10,

$$\begin{aligned} p_{M \neq 0} &= \left| \frac{\langle {}^1\text{TT}|V|^{}{}^5\text{TT}_M \rangle}{3J + g\mu_B B_0 M} \right|^2 \\ p_{M=0} &= 1 + \left| \frac{\langle {}^1\text{TT}|V|^{}{}^5\text{TT}_M \rangle}{3J + g\mu_B B_0 M} \right|^2 \end{aligned} \quad (\text{B.17})$$

In the large J limit, the perturbation in Eq. B.17 goes to zero and, again, only the $M = 0$ quintet state is predicted to be observable. Based on similar arguments, population of the $|{}^3\text{TT}\rangle$ state is not observed. By using the **result** of Merrifield's model only the $|{}^1\text{TT}\rangle$ and $|{}^5\text{TT}_0\rangle$ levels are populated in any case. I refer to all of these as the Q_0 model.

In contrast, if one uses the **argument** of Merrifield's model, the original definition of singlet character, then the resulting populations are,

$$p_n = |\langle {}^1\text{TT}|n \rangle|^2. \quad (\text{B.18})$$

The probability that $|n\rangle = |{}^5\text{TT}_M\rangle_1$ has singlet amplitude is (Eq. B.16),

$$|\langle {}^1\text{TT}|{}^5\text{TT}_M \rangle_1|^2 = \left| \frac{\langle {}^1\text{TT}|V|^{}{}^5\text{TT}_M \rangle}{3J + g\mu_B B_0 M} \right|^2. \quad (\text{B.19})$$

The numerator in Eq. B.19 is the transition matrix element from the golden rule in Eq. B.7. When the exchange interaction goes to zero, B_0 dominates this expression so that the small perturbations in $|V|^2$ are reduced by a factor proportional to $1/B_0 M$. Because $B_0 \gg |D|$, the population of the ${}^5\text{TT}_0$ level dominates so that the result converges to the Q_0 model as J goes to zero. In the large J limit ($|J| \gg B_0$), the populations in Eq. B.19 become independent of M and they **numerically** converge to the populations from the

JDE model. But the numerical convergence of the adapted Merrifield model (Eq. B.18) and the *JDE* model in the large exchange limit is merely a coincidence. By considering the underlying processes, selection rules, hamiltonians, and theories, it is clear that these are foundationally independent models.

Ref. [15] proposed a Q_0 model for tightly packed TIPS-Tc thin films, where fast fluctuations in the triplet-triplet exchange coupling J afforded by, for example, hopping, leads to irreversible coherence decay, $\text{TT} \rightarrow \text{T} + \text{T}$. They used it to model their trEPR spectrum, where the $\text{T} + \text{T}$ and TT signals grow in concurrently. After unpairing, they claim that separated triplets then recombine so that the accompanying rapid increase in exchange coupling collapses the unpaired triplet states onto the pair spin states, $\text{T} + \text{T} \rightarrow \text{TT}$. The hamiltonian that is used to calculate the energies for the trEPR spectrum is a function of a large exchange energy that splits the total spin states so that there are no crossings in the field range ($|J| > 20$ GHz). If dissociation is much faster than spin conversion, $^1\text{TT} \rightarrow \text{T} + \text{T} \rightarrow ^{2S+1}\text{TT}_M$, the pair spectrum could be found by first quenching the ^1TT density matrix and then quenching the resulting $\text{T} + \text{T}$ density matrix back into the $^{2S+1}\text{TT}_M$ basis. The result is that only the $^{2S+1}\text{TT}_0$ levels are populated. An argument must be made for not observing the spectrum from $^3\text{TT}_0$ and it is unclear why Ref. [15] assumes that the exchange symmetry must hold upon repairing. Recall that in the original Merrifield model, it is assumed that all $|M_A, M_B\rangle$ levels are equally populated.

The data from single crystals of parallel TES TIPS-TT dimers in Chapter 5 cannot be replicated by Ref. [15]'s Q_0 model. Based on a similar argument, in Chapter 5, I perform a quantum quench to calculate the unpaired $\text{T} + \text{T}$ populations from the TT density matrix that is calculated from the *JDE* model. The TT spectrum is from TES TIPS-TT dimers that are in a moderate coupling regime, $|J| \approx 15$ GHz, and unpairing instead follows spin

conversion, $^1\text{TT} \rightarrow ^5\text{TT} \rightarrow \text{T} + \text{T}$. The unpaired ^1TT state, on its own, is not predicted to have an EPR spectrum (Chapter 5).

Ref. [17] reports trEPR spectra from glassy solutions of bridged TIPS-bipentacene molecular dimers. Their chromophores are joined by long linkers that are not rigid; they can rotate about the linkers so that their relative orientation is not fixed. In their trEPR spectra, a $\text{T} + \text{T}$ signal grows in as the TT spectrum begins to decay. They assign the early time spectra to the quintet and fit it using a Q_0 model. The hamiltonian used to calculate the energies for their spectra is a function of an isotropic exchange energy that is approximately equal to the Zeeman field energy, $|J| \approx 10 \text{ GHz}$.[‡] In Chapter 4, I report the trEPR spectrum from a glass of strongly coupled ($|J| > 20 \text{ GHz}$) and rigid TIPS-BP1' molecular dimers. But any signal from an $S = 1$ spin was absent from its spectrum (Fig. 4.3), and the spectrum is not reproduced by a Q_0 model.

[‡]Note that the values of J that Ref. [17] uses to calculate their spectra and energies, for example, in Figs. 3a and S7, are half of the J values reported in their Table S2. The exchange hamiltonian that Ref. [17] reports, like the JDE model hamiltonian, splits the singlet and triplet states by J (Fig. 5.3), which in their Fig. S7 are split by about 10 GHz, i.e., $J \approx 10 \text{ GHz}$. Ref. [17], however, also references Ref. [78] when discussing the splittings and their hamiltonian splits the states by $2J$.

ProQuest Number: 29320344

INFORMATION TO ALL USERS

The quality and completeness of this reproduction is dependent on the quality
and completeness of the copy made available to ProQuest.



Distributed by ProQuest LLC (2022).

Copyright of the Dissertation is held by the Author unless otherwise noted.

This work may be used in accordance with the terms of the Creative Commons license
or other rights statement, as indicated in the copyright statement or in the metadata
associated with this work. Unless otherwise specified in the copyright statement
or the metadata, all rights are reserved by the copyright holder.

This work is protected against unauthorized copying under Title 17,
United States Code and other applicable copyright laws.

Microform Edition where available © ProQuest LLC. No reproduction or digitization
of the Microform Edition is authorized without permission of ProQuest LLC.

ProQuest LLC
789 East Eisenhower Parkway
P.O. Box 1346
Ann Arbor, MI 48106 - 1346 USA